Electrokinetics of Nonpolar Dispersions for Electrophoretic Displays and Liquid Toner Printing

Elektrokinetiek van apolaire dispersies voor elektroforetische beeldschermen en printers met vloeibare toner

Manoj Prasad

Promotoren: prof. dr. ir. F. Beunis, dr. ir. F. Strubbe
Proefschrift ingediend tot het behalen van de graad van
Doctor in de ingenieurswetenschappen: toegepaste natuurkunde

UNIVERSITEIT
GENT

Vakgroep Elektronica en Informatiesystemen
Voorzitter: prof. dr. ir. R. Van de Walle
Faculteit Ingenieurswetenschappen en Architectuur
Academiejaar 2016 - 2017

ISBN 978-90-8578-963-5
NUR 950, 910
Wettelijk depot: D/2016/10.500/95

Promoters:

Prof. Dr. Ir. Filip Beunis

Dr. Ir. Filip Strubbe

Department of Electronics and Information Systems
Faculty of Engineering and Architecture
Ghent University

Members of the Examination Committee:

Prof. Dr. Ir. Luc Taerwe (Chairman)	Ghent University, DSE
Prof. Dr. Ir. Herbert De Smet	Ghent University, ELIS
Prof. Dr. Ir. Alex Henzen	South China Normal University
Prof. Dr. Christophe Leys	Ghent University, DAP
Prof. Dr. Ir. Kristiaan Neyts	Ghent University, ELIS
Dr. Ir. Herman Van de Straete	Xeikon
Prof. Dr. Paul Van Der Meeren	Ghent University, DAAPC
Prof. Dr. Ir. Filip Beunis	Ghent University, ELIS
Dr. Ir. Filip Strubbe	Ghent University, ELIS

Ghent University
Faculty of Engineering and Architecture
Department of Electronics and Information Systems
Sint-Pietersnieuwstraat 41
B-9000 Ghent
Belgium

Acknowledgements

This piece of work is the result of consistent support, motivation and guidance which I got for past four years from many people and all of them in some ways contributed in this work. No matter how much I say, words would be always insufficient to truly express what I was offered. But I must take this as an opportunity to thanks and express my deep sense of gratitude to all of them.

First and foremost, I would like to thank my advisors Prof. Filip Beunis and Dr. Filip Strubbe for giving me an opportunity to work under their supervision and helping me to evolve. This book is the culmination of their immense efforts and time which they put on me over these years. I got full benefits of their mature guidance in this expedition. I must also thank them for their patience and tolerance which was also very essential.

I thank to Prof. Kristiaan Neyts for coming to my desk time to time, going through the results and suggesting valuable ideas. Your friendly nature, curiosity and out of box thinking helped enormously in the evolution process of this dissertation. I would also like to thanks prof. Patric De Vischera, Prof. Alex De Vos, Prof. Mark Burgelman, Prof Jeroen Beeckman and Prof. Johan Lauwaert. Your presence around was always a source of inspiration and sometimes your words were torchbearer.

I would also like to thank Xeikon Company for supporting this research under IWT project o & o 2011. Many scientific problems and ideas which emerged during this collaboration helped greatly to shape this dissertation. The discussions during the meetings were always useful to extend my

understanding about the topic. I would specifically like to thank, Lode, Paul, William, Joachim Kurt, and Roel for their contribution in this fruition.

I would also like to express my sincere gratitude to the members of the examination committee for evaluating and carefully reading the dissertation. Their valuable suggestions indeed helped to improve and to make it errors free.

I would like to thanks the liquid crystals and photonics group for providing an excellent work environment and helping me various ways to reach at this point. The memories of all these years, the time we spent together and all of you will always be in my heart. Each of you inspired me in some ways and I am really indebted for that. I thank, Toon (for helps related to Labview, microscope) Masoumeh , Oksana, Casper (for fruitful discussions), Stijn (for helps related Matlab and Labview codes), John (your experience was always beneficial and thanks for helping me in formatting), Oliver (for helps related to Matlab), Samira (for helping me in LCR measurements), Lieven, Wouter, Aimi, Yi, Thomas, Mohammad, Glenn, Michiel, Karel, Inge, Serena, Frédérique, Varsenik, Xiaoning, Tigran, Pavlo and Chun-Ta, for being part of this Journey. I also wish good luck to newly joined PhD students Bavo, Sheng and Boxun.

I thank my parents for their immense support and unconditional love. I also thank my elder brother and sister-in law for always being there for me, supporting me and keeping me away from all distractions. It is a matter of great joy to see you growing up: Vineet and Jiya.

Last but not least I would also like to thank Prachi for being with me, holding me, and listening me. Your presence in my life makes me the blessed one.

Thanks, Ghent University; Thanks, Ghent; Thanks, Belgium.

Manoj Prasad

9 December 2016

List of Publications

Journal Publications

1. Manoj Prasad, Filip Strubbe, Filip Beunis and Kristiaan Neyts, Space charge Limited Release of Charged Inverse Micelles in Non-polar liquids, *Phys. Chem. Chem. Phys.*, 2016, 18, 19289-19298.

2. Manoj Prasad, Filip Strubbe, Filip Beunis and Kristiaan Neyts, Different Types of Charged Inverse Micelles in Non-Polar Media, *Langmuir*, 2016, 32(23), 5096-5801.

3. Manoj Prasad, Filip Beunis, Kristiaan Neyts and Filip Strubbe, Switching of Charged Inverse Micelles in Non-polar Liquids, *J. Colloid Interface Sci.*, 2015, 458, 39–44.

4. Filip Strubbe, Manoj Prasad and Filip Beunis, Characterizing Generated Charged Inverse Micelles with Transient Current Measurements, *J. Phys. Chem.* B, 2015, 119 (5), 1957–1965.

Conference Publications

1. Kristiaan Neyts, Manoj Prasad, Masoumeh Karvar, Filip Beunis and Filip Strubbe, Charge transport by Inverse Micelles in Non-Polar Media, Interactions and Transport of Charged Species in Bulk and at Interfaces, July 4-7, 2016, CECAM, Austria.

2. Manoj Prasad, Filip Strubbe, Filip Beunis and Kristiaan Neyts,

Different Types of Charged Inverse Micelles in Non-Polar Liquids, 90th ACS Colloid and Surface Science Symposium, June 5-8, 2016, Harvard University, Cambridge MA, USA.

3. Manoj Prasad, Filip Strubbe, Kristiaan Neyts and Filip Beunis, Switching of Charged Inverse Micelles, 28th Conference of The European Colloid and Interface Society, September 7-12, 2014, Limassol, Cyprus.

4. Manoj Prasad, Filip Strubbe, Kristiaan Neyts and Filip Beunis, Transport of Charge Inverse Micelles in Non-Polar Liquids, 11th International Symposium on Electrokinetic Phenomenona, May 20-23, 2014, Ghent University, Ghent, Belgium.

Table of Contents

Acknowledgements ..... **i**

List of Publications ..... **iv**

Table of Contents ..... **vii**

Summary ..... **xiii**

Samenvatting ..... **xix**

List of Figures ..... **xxv**

List of Symbols ..... **xli**

List of Abbreviations ..... **xlv**

Chapter 1: Introduction **1**

1.1 Formation of Charge in Liquids 2
1.2 Applications of Non-Polar Colloids 3
1.2.1 Electrophoretic Displays (EPDs) 4
1.2.2 Liquid Toner 7
1.3 Surfactants 8

1.4 Charge Formation in Non-Polar Liquid With Surfactant 10
1.4.1 Dissociation Mechanism 11
1.4.2 Disproportionation Mechanism 11
1.5 Charging of Colloidal Particles Promoted by Surfactants 14
1.5.1 Acid Base Interaction 14
1.5.2 Preferential Adsorption 15
1.5.3 Surface Dissociation 16
1.6 Stabilization of Colloidal Particles 16
1.6.1 Electrostatic Stabilization (DLVO Theory) 17
1.6.1.1 Van der Waals Attraction 17
1.6.1.2 Double-Layer Repulsion 17
1.6.2 Steric Stabilization 19
1.7 Scope and Overview of This Work 20
1.7.1 Scope 20
1.7.2 Overview 22

Chapter 2: Transient Current Measurements 25

2.1 Introduction 25
2.2 Materials 26
2.2.1 Non-Polar Liquids 27
2.2.2 Surfactants 27
2.3 Device Structure 29
2.4 Transient Current Measurement Setup 30
2.4.1 The Current Measurement Procedure 33
2.4.2 Interpretation of the Measured Currents 33
2.5 Drift, Diffusion, Generation and Recombination of Charged Inverse Micelles 34
2.5.1 Estimation of the Mobility and the Concentration of the CIMs 38
2.5.2 Electrodynamical Regimes 39
2.6 Conclusions 41

Chapter 3: Transport of Charged Inverse Micelles for the Reversal Voltages 43

3.1 Introduction 43
3.2 Experimental Methods 45
3.2.1 Transient Currents Measurements 45
3.2.2 Transient Particle Trajectories 46

3.3 Results and Discussion 47
3.3.1 Low Charge Content: Geometry and Diffusion Limited Currents 48
3.3.2 High Charge Content: Space Charge and Diffuse Double Layer Limited Currents 49
3.3.2.1 Small Polarizing Voltage (V_0 < 1 V) 49
3.3.2.2 Large Polarizing Voltage (V_0 > 1 V) 50
3.3.2.3 Electrohydrodynamic Flow 55
3.3.3 Verification of EHD Flow: Transient Trajectories of the Tracer Particles 57
3.4 Conclusions 57

Chapter 4: Investigation on Newly Generated Charged Inverse Micelles 59

4.1 Introduction 59
4.2 Analytical Approximations 60
4.2.1 Generation Limited Currents 63
4.2.2 Transient Generation Current for Voltage Step $V_0 \rightarrow V_1$ 64
4.2.2.1 The Double Layer Rearrangement Current 65
4.2.2.2 Transient Generation Current 65
4.3 Materials and Methods 68
4.4 Results and Discussion 68
4.4.1 Comparison Between the Measurements and the Simulations 68
4.4.2 The Concentration and the Mobility of the Newly Generated CIMs 74
4.5 Conclusions 75

Chapter 5: Adsorption and Release of Newly Generated Charged Inverse Micelles 77

5.1 Introduction 77
5.2 Materials and Methods 79
5.3 Results 81
5.3.1 Origin of the Second Peak 81
5.3.2 Comparison Between the Results of Type C and D Experiments 85
5.3.3 Release of SCIMs 86
5.3.4 The Polarity of the Released SCIMs 89

5.3.5 Different Types of CIMs 90
5.3.6 Effect of the Short Circuit Duration on the Concentration of..... SCIMs 95
5.4 Further Discussion 96
5.4.1 Why does the Integral of the Second Peak Saturate? 96
5.4.2 Reduced Decay Constant of SCIMs in the Absence of Regular CIMs and Neutral IMs 97
5.5 Conclusions 98

Chapter 6: Release of the Adsorbed Generated Charged Inverse Micelles 99

6.1 Introduction 99
6.2 Theoretical Model 100
6.2.1 Simulation Model 100
6.2.1.1 Initial Conditions 102
6.2.1.2 Boundary Conditions 102
6.2.2 Analytical Equations 105
6.3 Experiments 106
6.4 Measurement and Simulation Results 107
6.4.1 When the Bulk is Replaced With Pure Dodecane 107
6.4.2 With the Presence of Regular CIMs 110
6.5 Conclusions 114

Chapter 7: Electrokinetics of Colloidal Particles and Charged Inverse Micelles 117

7.1 Introduction 117
7.2 Material and Methods 119
7.2.1 Materials 119
7.2.2 Methods 119
7.2.2.1 Electrical Current Measurements 119
7.2.2.2 Optical Setup and Measurements 121
7.3 Theoretical Model 123
7.3.1 Electrical Currents 123
7.3.2 The Size and Charge of Particles 125
7.4 Results and Discussion 126
7.4.1 Comparison Between Measured and Simulated Currents 126

7.4.2 Currents Measurements For Non-Polar Dispersions With a Low Concentration of Liquid Toner Particles in Lytol 131
7.4.3 Single Particle Tracking: Mobility and Size Measurements of Toner Particles..... 135
7.4.4 Current Measurements for Diluted Liquid Toner..... 137
7.4.4.1 Simulation: A Peak Due to Highly Charged Particles..... 140
7.4.5 Current Measurements for Non-Polar Dispersions With High Concentrations of Particles..... 143
7.4.6 Charging of Toner Particles at the Electrode Surfaces in a DC Field..... 144
7.4.7 Conclusions 147

Chapter 8: Conclusions and Future Scope..... 149

8.1 Summary of the Main Findings..... 149
8.2 Applicability..... 150
8.3 Future Scope..... 152

Bibliography 155

Summary

Displaying information electronically is part of our daily life, but the technologies which are in use today are not very energy efficient. We are living in an age in which energy resources are depleting, therefore it is desired to have an energetically more efficient display. The display technology known as electrophoretic displays (EPDs) consumes almost no energy and is based on the scattering of incident light without needing back illumination. This technology offers many advantages over LCD/LED displays such as nearly zero power consumption, bi-stability, a large viewing angle and high contrast under direct sunlight. Despite of these advantages, EPD based applications are at present limited to only a few devices such as e-book readers. The main reasons for this are a low refresh rate (such that video is impossible) and poor color saturation. If these problems can be solved EPDs could become a very interesting candidate for future displays. In order to solve the problems associated with EPDs, it is indispensable to have a better understanding about the underlying physical principles on which EPD technology is based.

Basically, each pixel of a grayscale EPD consists of many microcapsules, each containing a dispersion of black and white pigment particles in a non-polar liquid with surfactant, see Fig. S.1. In the dispersion, the surfactant is added for two purposes: stabilizing and electrically charging the particles. The surfactant is chosen in such a way that the black and white particles become oppositely charged. The black particles absorb light while the white particles scatter light. A layer of capsules containing the dispersion of charged pigment particles is sandwiched between two electrodes, one of

which is transparent. When a voltage is applied, the particles move towards the electrode with opposite polarity. For instance, if the potential on the transparent electrode is higher than the potential of the counter electrode and the black particles are negatively charged, these particles will move towards the transparent electrode and adsorb the light, resulting in a black pixel. The surfactant is needed to charge the particles, but has undesired side-effects. Not all added surfactant adsorbs at the particles or at other interfaces and the excess remains free in the dispersion in the form of charged or neutral inverse micelles. The presence of free charged inverse micelles (CIMs) results in an increase in the conductivity of the dispersion, which in turn affects the electric field in the device. Through the electric field, the surfactant affects the switching characteristics of the pigment particles, resulting in a larger response time of the device. In addition to this, the presence of free CIMs also results in an increase in power consumption and pattern formation next to the electrodes, which reduces the life span of device.

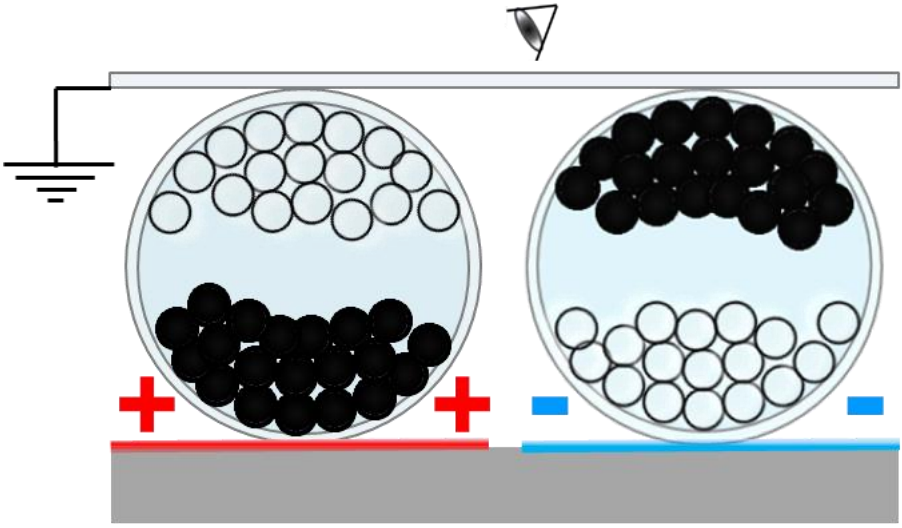

Figure S.1: Pixels of an EPD, each consisting of a microcapsule filled with positively (white particles) and negatively charged (black particles) particles. The particles move between the electrodes in response to an applied electric field. The presence of the particles next to the opposite polarity electrode (in the direction of viewing angle) results in black and white pixels to a viewer.

Printing on a paper is another and relatively old way of presenting information. In general, there are two types of printing technologies, namely

dry toner and liquid toner printing. Liquid toners consist of a dispersion of pigment particles with a charging agent (surfactant) in a non-polar liquid. The liquid toner based printing has many advantages over dry toner based printing, such as high-resolution printing, uniform gloss, sharp image edges, thin image layer, high printing speed and the printing process can also be environment friendly when using organic nonpolar solvents. Despite of these advantages, liquid toner based printing is still in its infancy. There are many reasons for this, such as the unclear mechanism of surfactant mediated charging and particle stabilization, and unclear interfacial behavior and electrodynamics of the particles.

Motivated by these problems associated with an EPD and liquid toners based printing, in this dissertation, firstly the electrodynamics and interfacial properties of CIMs are studied when no particles are present, and then the same types of studies are performed in dispersions with particles. After an introduction covering the background and state of the art in chapter 1. Chapter 2, describes the materials and experimental techniques that are used in this dissertation. The most important method used in this work to study the electrodynamics and the interfacial properties of CIMs is transient current measurement. In these experiments, a voltage step is applied across a layer of liquid between two planar electrodes and the resulting current is measured. From the shape of the current the electrodynamical behavior of the CIMs can be understood. The electrodynamical behavior of CIMs in response to a polarizing voltage is understood well, and four limiting regimes have been identified.

In chapter 3, transient current measurements for the case when the polarity of the voltage is reversed just after a polarizing voltage step are described. In addition to providing information about the switching characteristics of the CIMs such a study also provides details about the interfacial behavior of the CIMs. By varying the charge content and the applied polarizing and reversal voltages, all the important switching regimes are explored. To understand the electrodynamics of the CIMs, the measured currents are compared with a simulation model based on the Poisson-Nernst-Planck (PNP) equations. It is found that the dynamics of the CIMs can be understood well on the basis of the PNP model. However in the space charge regime, when the magnitude of the applied reverse voltage is above 11 V, the measurements show a peak in the current that occurs earlier than predicted by the PNP model. This

mismatch is attributed to electrohydrodynamic (EHD) flow in the system. The occurrence of EHD flow is confirmed by following the trajectories of charged tracer particles for large reversal voltages. Also in the space charge limited regime, for a longer duration of the polarizing voltage step a second peak is observed which cannot be explained by the PNP model. Further investigation reveals that this peak is related to newly generated CIMs.

In chapter 4, the physical properties of the newly generated CIMs are investigated by increasing the voltage after the system has reached steady state. By comparing the measured currents with the simulation model based on the PNP equations and with analytical results, it is found that the newly generated CIMs have the same size and mobility as that of the regular CIMs. In addition to this, it is also confirmed that bulk disproportionation is the generation mechanism of the newly generated CIMs. The findings of this chapter raise the question why the generated CIMs do not release at the same moment as the regular CIMs.

In chapter 5, a detailed study on the origin of the observed second peak in the reversal current, the properties of the CIMs responsible for the peak and their interfacial properties is presented. The origin of the peak is investigated by varying the magnitude of both the polarizing and the reversal voltage, the duration of the polarizing voltage step, the device thickness and the concentration of surfactant in the device. It is found that the integral of the peak increases with increasing duration of the polarizing voltage step, for higher device thicknesses and higher concentrations of surfactant, before reaching a saturation level. These findings lead to the conclusion that indeed the peak is related to newly generated CIMs due to a bulk disproportionation mechanism in which the collision of two neutral inverse micelles (IMs) results in two oppositely charged inverse micelles or vice versa, (see Fig. S.2). However, it is also found that the integral of the peak is just 5 % of the total generated charge during the polarizing voltage step.

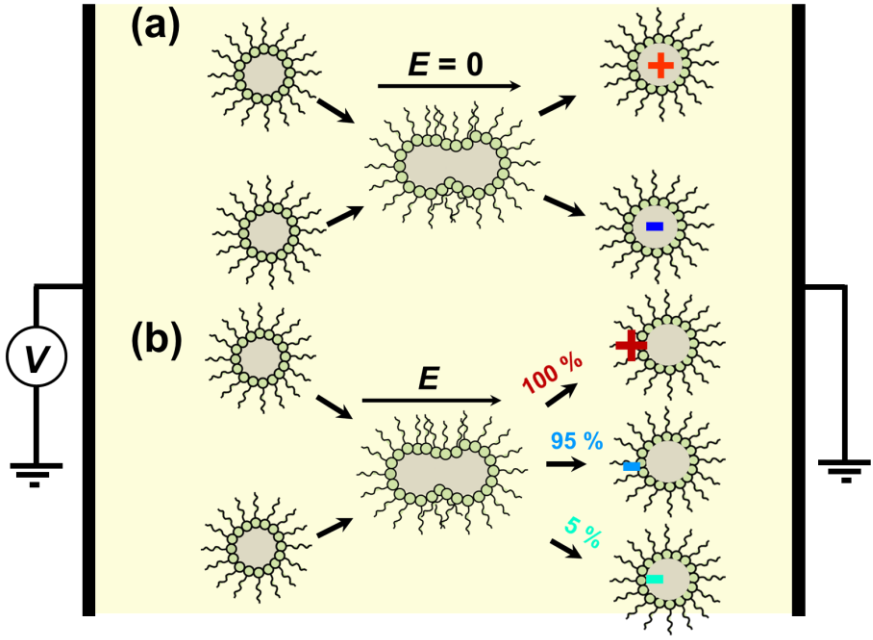

Figure S.2: A depiction of the disproportionation mechanism in which the Brownian collision of two neutral inverse micelles (IMs) results in two oppositely charged inverse micelles (CIMs) or the reverse process in which the collision of two oppositely charged inverse micelles results two neutral IMs. In (a), the charge generation process is depicted in the absence of an electric field during which regular CIMs are generated. In (b), the same is depicted in the presence of an electric field during which three different types of CIMs are generated in different proportions.

For measurements in which the bulk of the device is replaced by pure dodecane after a long polarizing voltage, the currents match well with the Mott-Gurney equation. By varying the duration of the polarizing voltage step, it is confirmed that the measured Mott-Gurney currents are due to newly generated CIMs. Further investigation reveals that the CIMs responsible for the second peak in the reversal current are negatively charged. Also, it is found that the presence of newly generated CIMs does not affect the shape of the reversal current, which indicates their presence does not affect the field in the device. This leads to the conclusion that the generated CIMs are very close to the electrodes. These findings indicate that three types of CIMs are generated in the bulk in the presence of an electric field, i.e. 100 % positively and 95 % negatively charged IMs that are never released and 5% negatively charged IMs that are released. The difference in

the interfacial behavior of the generated CIMs can be explained by the location of the charge with in the CIMs, see Fig. S.2. For most of the generated CIMs, the location of the charge is at the outside of the IMs, so that they attracted very strongly by their image charge in the electrode and are never released. However, for 5 % of the generated negative CIMs, the charge is closer to the center of the IM, resulting in a reduced force of attraction from the electrode. Hence, these CIMs can be released from the electrode when the voltage is reversed or switched off. Also, it is found that the presence of neutral and regular CIMs speeds up the decay of the generated CIMs.

On the basis of the findings of chapter 5, in chapter 6 a model is presented in which the release of SCIMs from the interface layer is space charge limited. In this model, charges are released from one interface in such a way that the field at the interface becomes zero. The model explains a broad range of experimental results with some additional effects such as EHD flow in the system.

In chapter 7, the switching electrodynamics and interfacial properties of charged particles are studied in the presence of CIMs. For small applied voltages, for which the particles do not reach the electrodes, the dynamics of the system can be understood well on the basis of the PNP model in combination with EHD flows. However, for larger voltages, it is necessary to include particle charging at the electrodes, resulting in a 10-20 times increase in particle mobility.

In the concluding chapter 8, the insights about non-polar surfactant systems that are acquired in this work are summarized, and interesting avenues for further work on this topic are suggested.

Samenvatting

Elektronische beeldschermen om informatie weer te geven zijn deel van ons dagelijks leven, maar de technologieën die er vandaag voor gebruikt worden zijn verre van energie-efficiënt. In een tijd waarin duurzaamheid steeds belangrijker wordt is het nodig om energiezuinigere beeldschermen te ontwikkelen. Elektroforetische beeldschermen (EPDs) zijn hiervoor een veelbelovende optie: ze verbruiken bijna geen energie doordat ze geen schermverlichting bevatten en bistabiel zijn. In vergelijking met de huidige LCD- en LED-beeldschermen bieden ze bovendien een grote kijkhoek en een goede resolutie onder direct zonlicht. Tegenwoordig worden EPDs slechts in een beperkt aantal toepassingen zoals elektronische boeken gebruikt. Dit komt doordat het beeld traag ververst wordt (waardoor video onmogelijk is), en de weergave van gesatureerde kleuren voorlopig niet mogelijk is. Als deze problemen zouden opgelost worden, zouden EPDs in veel meer toepassingen gebruikt kunnen worden. Om daar toe te komen is het nodig om de fysische principes waarop deze technologie gebaseerd is beter te begrijpen.

In essentie bestaat elk beeldpunt van een zwart-wit EPD uit microcapsules gevuld met een dispersie van zwarte en witte pigmentdeeltjes in een apolaire vloeistof met surfactant (zie figuur S.1). Het surfactant wordt toegevoegd omwille van twee redenen: om de deeltjes te stabiliseren en om ze een elektrische lading te geven. De materialen worden zo gekozen dat witte en zwarte deeltjes een tegengestelde lading krijgen. De zwarte deeltjes absorberen licht, de witte deeltjes verstrooien het. De microcapsules met de dispersie bevinden zich tussen twee elektroden, waarvan er één transparant

is. Wanneer er een spanning wordt aangelegd, bewegen de witte en zwarte deeltjes naar tegengestelde elektroden. Als de transparante elektrode bijvoorbeeld op de grootste potentiaal staat en de zwarte deeltjes zijn negatief geladen, zullen deze deeltjes naar de transparante elektrode bewegen en daar het licht absorberen, waardoor het beeldpunt zwart is. Het

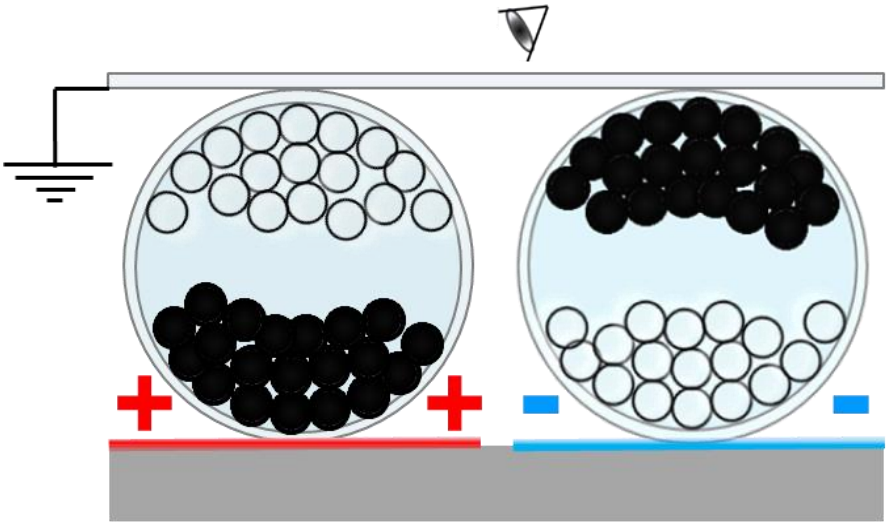

Figuur S.1: Beeldpunten in een EPD bevatten microcapsules gevuld met positief geladen witte deeltjes en negatief geladen zwarte deeltjes. De deeltjes bewegen tussen de elektroden wanneer er spanningen aangelegd worden. Op die manier kan er voor gezorgd worden dat enkel de witte of enkel de zwarte pigmentdeeltjes zichtbaar zijn

toegevoegde surfactant is nodig om de deeltjes op te laden, maar heeft ongewenste neveneffecten. Niet al de surfactantmoleculen worden geadsorbeerd op de deeltjes of op andere oppervlakken: velen blijven vrij in de dispersie onder de vorm van ongeladen en geladen micellen. De geladen micellen (CIMs) leiden tot een hogere geleidbaarheid van de dispersie, waardoor het elektrisch veld wordt beïnvloed. Daardoor verandert de beweging van de deeltjes, en dit zorgt ervoor dat het beeldscherm trager wordt. Bovendien zijn de vrije CIMs verantwoordelijk voor een hoger energieverbruik en voor patroonvorming bij de elektroden, waardoor de levensduur van het toestel vermindert.

Een zeer vergelijkbare technologie, met geladen pigmentdeeltjes in een apolaire vloeistof met surfactant, wordt gebruikt in een nieuwe soort

industriële drukmachines. Deze drukmachines met vloeibare toner hebben vele voordelen ten opzicht van de meer gangbare machines met droge toner. Ze kunnen een hogere resolutie, scherpere randen en een meer uniforme glans weergeven met een dunnere inktlaag, en drukken sneller en op een meer milieuvriendelijke manier. De techniek met vloeibare toner moet echter nog verder ontwikkeld worden voor hij algemeen bruikbaar is: het opladen en stabiliseren van de inktdeeltjes met surfactant, en de beweging en afzetting op een oppervlak is nog niet voldoende begrepen. Het zijn deze problemen en uitdagingen voor zowel elektroforetische beeldschermen als vloeibare toner die de motivatie vormden voor het werk dat ik beschrijf in dit doctoraatsproefschrift.

Na een inleidend hoofdstuk, waarin de achtergrond en stand van zaken rond het gedrag van lading in apolaire media wordt behandeld, beschrijf ik de gebruikte materialen en experimentele technieken in hoofdstuk 2. De belangrijkste methode die ik gebruikt heb om de elektrodynamica en het gedrag aan oppervlakken van geladen inverse micellen (CIMs) te onderzoeken, is gebaseerd op overgangsstroommetingen. Bij deze metingen wordt een spanningsstap aangelegd over een vloeistoflaag tussen twee elektroden, en wordt de resulterende stroom gemeten. Uit de stroom kan de beweging van de CIMs afgeleid worden. Dit heeft in het verleden reeds geleid tot een goed begrip van de manier waarop CIMs vanuit de vloeistof naar de elektroden bewegen.

In hoofdstuk 3 worden de overgangsstroommetingen beschreven voor het geval waarbij CIMs van de ene naar de andere elektrode bewegen. Deze metingen geven niet enkel informatie van het schakelgedrag van toepassingen die hierop gebaseerd zijn, maar laten ook toe het gedrag van CIMs aan een oppervlak te onderzoeken. Door de ladingsinhoud en de gebruikte spanningen te variëren, heb ik acht verschillende soorten gedrag kunnen onderscheiden. De metingen worden vergeleken met simulaties gebaseerd op de Poisson-Nernst-Planck (PNP) vergelijkingen. In de meeste gevallen levert dit een goede overeenkomst op, maar wanneer de ladingsinhoud groot is en de spanningen hoog, is er een duidelijk verschil in de vorm van een stroompiek die vroeger dan verwacht optreedt. Dit wordt verklaard door middel van elektrohydrodynamische (EHD) stroming, en verifieer deze verklaring door de beweging van enkele deeltjes te volgen onder de microscoop. In sommige gevallen is er ook een tweede

onverklaarde stroompiek zichtbaar. Deze piek wordt toegeschreven aan nieuw gegenereerde CIMs.

In hoofdstuk 4 ga ik dieper in op de eigenschappen van deze nieuw gegenereerde CIMs, door overgangsstroommetingen uit te voeren waarbij de spanning plots verhoogd wordt (maar niet van teken wisselt). Door deze metingen te vergelijken met simulaties en met analytische berekeningen, kom ik tot de conclusie dat deze gegenereerde CIMs dezelfde grootte en mobiliteit hebben als normale CIMs. De metingen bevestigen ook dat de nieuwe CIMs gegenereerd worden door een disproportionatieproces in de vloeistof. De resultaten uit dit hoofdstuk leiden tot de vraag waarom de gegenereerde micellen zich aan een oppervlak anders gedragen dan de normale micellen.

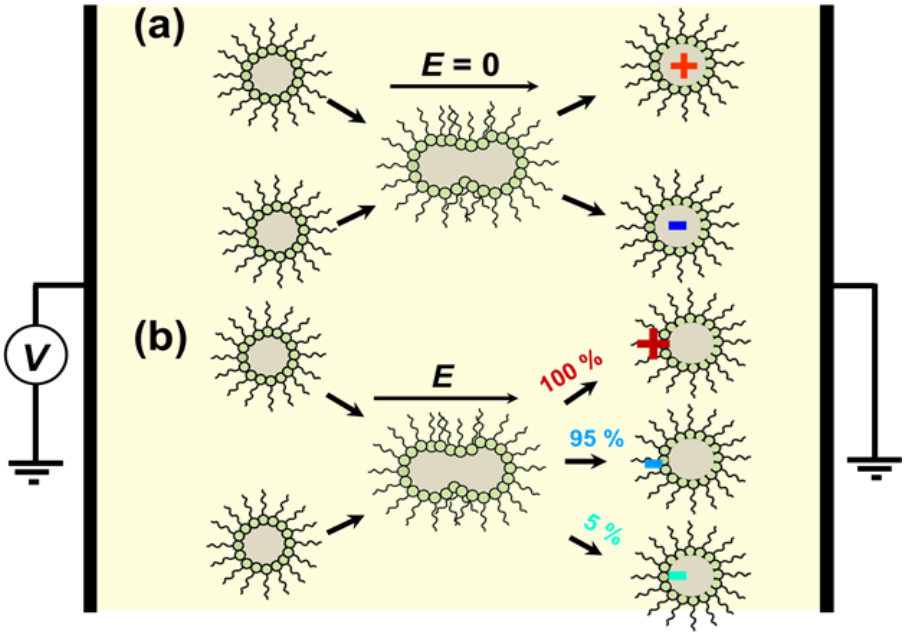

Figuur S.2: (a) Schematische voorstelling van het generatieproces waarbij in een botsing van twee neutrale inverse micellen een lading kan uitgewisseld worden. (b) Een meer nauwkeurige beschrijving waarbij lading in de gegenereerde inverse micellen zich aan de rand van de micelle bevindt. Als er een elektrisch veld aanligt, bewegen deze micellen naar de elektroden voor ze vervallen tot normale micellen, en worden ze in slechts 5% van de gevallen terug vrijgegeven.

In hoofdstuk 5 wordt een gedetailleerde studie gepresenteerd naar de oorsprong van de tweede stroompiek in schakelstromen, de eigenschappen van de micellen die er verantwoordelijk voor zijn, en hun gedrag aan een oppervlak. De oorsprong van de piek wordt onderzocht door de amplitude en de duur van de aangelegde spanningen, de dikte van de testcel en de concentratie surfactant in de vloeistof te variëren. De integraal van de stroompiek neemt toe voor langer aangelegde polariseerspanningen, voor dikkere testcellen en voor grotere concentraties surfactant, tot hij satureert. Dit bevestigt dat de gegenereerde CIMs het gevolg zijn van disproportionatie (zie figuur S.2), maar de metingen tonen dat slechts 5 % van de gegenereerde CIMs bijdraagt tot de stroompiek.

Wanneer de vloeistof in de testcel na de polariseerspanning wordt vervangen door puur dodecaan, blijken de stroommetingen goed beschreven te worden door de Mott-Gurney formule, die ruimteladingsgelimiteerde injectie van lading beschrijft. Aan de hand van een variant op deze meting kan ik afleiden dat de tweede stroompiek enkel veroorzaakt wordt door negatieve CIMs die zeer dicht aan het oppervlak vertrekken. Deze waarnemingen leiden tot de conclusie dat drie soorten micellen worden gegenereerd: positieve micellen die, eens ze een oppervlak bereiken, niet meer loskomen, en negatieve waarvan 95 % ook niet meer loskomt en 5 % terug in de vloeistof geinjecteerd wordt. Ik verklaar deze verschillen door de plaats van de lading in de CIMs (zie fig S2): waar in normale CIMs de lading zich in het centrum bevindt, zit ze voor de nieuw gegenereerde ladingen dicht tegen de rand van de CIM, waardoor ze zeer sterk aangetrokken worden tot hun beeldlading in de elektroden. In 5 % van de negatieve gegenereerde CIMs zit de lading toch ver genoeg van de rand dat ze nog opnieuw kunnen vrijkomen als de spanning wordt omgekeerd of wegvalt. De gegenereerde CIMs vervallen uiteindelijk terug naar normale CIMs (met de lading in het centrum), en dit proces verloopt sneller als er normale neutrale of geladen inverse micellen in de buurt zijn.

Op basis van de resultaten in hoofdstuk 5, werk ik in hoofdstuk 6 een model uit waarin ruimteladingsgelimiteerde injectie van lading van CIMs verwerkt is. Hierbij wordt de lading op zo'n manier vrijgegeven dat het elektrisch veld aan het oppervlak steeds gelijk blijft aan nul. Simulaties op basis van dit model (aangevuld met verklaringen aan de hand van EHD stroom), beschrijven een brede waaier aan experimentele resultaten.

In hoofdstuk 7 wordt het schakelgedrag van geladen colloïdale deeltjes in dispersies met CIMs onderzocht. Voor kleine schakelspanningen, waarbij de deeltjes niet voldoende tijd hebben om de elektrodes te bereiken, wordt hun gedrag goed beschreven door de PNP vergelijkingen in combinatie met EHD stroming. Voor grotere spanningen wordt het duidelijk dat de deeltjes aan de elektrode van lading kunnen veranderen, waarbij de lading soms omkeert en soms tot 20 keer toeneemt.

In het afsluitende hoofdstuk 8 worden alle behaalde resultaten nog eens samengevat, en suggereer ik interessante mogelijkheden voor verder onderzoek.

List of Figures

Figure S.1: Pixels of an EPD, each consisting of a microcapsule filled with positively (white particles) and negatively charged (black particles) particles. The particles move between the electrodes in response to an applied electric field. The presence of the particles next to the opposite polarity electrode (in the direction of viewing angle) results in black and white pixels to a viewer. xiv

Figure S.2: A depiction of the disproportionation mechanism in which the Brownian collision of two neutral inverse micelles (IMs) results in two oppositely charged inverse micelles (CIMs) or the reverse process in which the collision of two oppositely charged inverse micelles results two neutral IMs. In (a), the charge generation process is depicted in the absence of an electric field during which regular CIMs are generated. In (b), the same is depicted in the presence of an electric field during which three different types of CIMs are generated in different proportions..... xvii

Figuur S.1: Beeldpunten in een EPD bevatten microcapsules gevuld met positief geladen witte deeltjes en negatief geladen zwarte deeltjes. De deeltjes bewegen tussen de elektroden wanneer er spanningen aangelegd worden. Op die manier kan er voor gezorgd worden dat enkel de witte of enkel de zwarte pigmentdeeltjes zichtbaar zijn xx

Figuur S.2: (a) Schematische voorstelling van het generatieproces waarbij in een botsing van twee neutrale inverse

micellen een lading kan uitgewisseld worden. (b) Een meer nauwkeurige beschrijving waarbij lading in de gegenereerde inverse micellen zich aan de rand van de micelle bevindt. Als er een elektrisch veld aanligt, bewegen deze micellen naar de elektroden voor ze vervallen tot normale micellen, en worden ze in slechts 5% van de gevallen terug vrijgegeven. xxii

Figure 1.1: Each pixel in an EPD consists of microcapsules filled with negatively charged black and positively charged white particles in a non-polar liquid. In response to a voltage, the positively charged white and negatively charged black particles move to opposite electrodes resulting in black and white pixels. 5

Figure 1.2: A few devices based on V-EPDs are shown. In (a) the Amazon Kindle ebook reader is an example of a typical monochrome reflective display featuring low power consumption (b) the Sony E-ink based tablet: Sony DPTS1 digital paper system (c) E ink's triton color EPD offers 16 levels of gray scale and is able to displays 4096 colors – be it in a poor color quality (d) Plastic logic e-ink based flexible displays (d) Motorola Motofone (e) Sony's FES e-ink based watches. 6

Figure 1.3: Schematic illustration of four-stacked cell of an IP-EPD. Each cell contains charged color particles dispersed in a non-polar liquid and the electrodes are situated inside at the edges of the cell. 7

Figure 1.4: An example of a printer based on liquid toner (HP indigo 10000 digital press) [52]. 8

Figure 1.5: A few commonly used and studied surfactants: (a) anionic Sodium dioctylsulfosuccinate (Aerosol OT) (b) nonionic sorbitan trioleate (Sorb) (c) nonionic polyisobutylene succinimide (PIBS) (d) anionic zirconyl 2-ethyl hexanoate (Zr(Oct)2) [21,28]. 10

Figure 1.6: Illustration of the disproportionation mechanism in which a collision of two neutral micelles results in an intermediate hypothetical structure that then splits into two oppositely charged inverse micelles. 12

Figure 1.7: The linearly increasing concentration of charged inverse micelles with increasing weight fraction (ϕ_m) of OLOA 11K in dodecane supports the disproportionation mechanism of charging. 13

Figure 1.8: (a) Illustration of the Stern plane and electrical double layers around a negatively charged particle (black sphere) suspended in a liquid containing z:z ions. The postive ions are depicted as blue color spheres while the negative are depicted as red color spheres. In (b) the change in potential with distance *x* is shown. 18

Figure 1.9: Schematic illustration of two sterically stabilized particles. 20

Figure 2.1: The chemical structure of (a) n-dodecane (b) OLOA 11K. The polar character of the head is a result of the amine groups. The nonpolar tail and the polar head are linked by a succinimide group. 28

Figure 2.2: Schematic of (a) a glass substrate of thickness 1.1 mm coated on one side with a 20 nm thick layer of indium tin oxide (b) The measurement device is made by assembling the two substrates so that the electrodes overlap as indicated by *S* and the contact areas are not covered. Glass spacers mixed in UV-cured glue are used to hold the substrates together at a distance *d* from one another. 30

Figure 2.3: In (A) a picture of the transient current measurement setup. In (B) a schematic of the various parts of setup is shown: (a) the measurement device (b) the NI-DAQ device by which a voltage is applied across the device and the corresponding current in the external circuit is measured simultaneously (c) the Keithley 428 current amplifier (d) the input/output control section with graphical user interface. 31

Figure 2.4: Schematic of a device filled with a mixture of surfactant in a solvent. (a) During the short circuit time, the charges are uniformly distributed in the device. (b) In response to the polarizing voltage step, charges move towards the opposite polarity electrodes resulting in a

current in the external circuit. (c) Typical measured currents as a function of polarizing voltage amplitude are shown. The measured current has two phases, the initial transient phase, in which the current decreases very quickly and the quasi steady state phase in which approximately a constant current is measured. 32

Figure 2.5: All the measurements that are shown in this dissertation are performed on devices which have an area of S = 1 cm^2 while the distance between the electrodes d varies from 4 to 50 μm from experiment to experiment. Since the size of the electrodes is much larger than the distance between them, the device can be considered to be a one-dimensional structure in which all quantities vary only along the x axis. 36

Figure 2.6: The match between measured transient polarization current measurements (colored dots) (for the device with d = 48.36 μm and filled with ϕ_m = 0.003 of OLOA 11K in dodecane) and the simulations (black lines) validating the model based on drift, diffusion with generation/recombination of charged inverse micelles. The simulation parameters are $\bar{n}$ = 10 μm^{-3} and μ = 1320 $\mu m^2/Vs$. The mismatch for the quasi steady state currents (between measurements and simulations) for low voltages is due to charge injection from the electrodes which is not included in the model. It has been reported that for low voltages, the quasi steady state current is proportional to the electric field near the electrodes [90]..... 37

Figure 2.7: A transient current measurement for a polarizing voltage step 0→V0 (V0 = 5 V) on the device with d = 48.36 μm and filled with ϕ_m = 0.003 of OLOA 11K in dodecane. The voltage is applied at t = 0 s, when the charge distribution in the device was uniform. By integrating the current (shown by the filled pattern) and using Eq. 2.13 the value of the equilibrium concentration is obtained. The value of the mobility is obtained from the initial current using Eq. 2.14. 39

Figure 3.1: Schematic representation of a measurement device with two parallel electrodes separated at a distance d with

overlapping area S = 1 cm^2. In (a), starting from the homogeneous equilibrium situation, a voltage step V_0 is applied and the CIMs travel towards the electrodes of opposite polarity resulting in a current in the external circuit. Eventually they end up in the diffuse double layers at the electrodes. In (b) the voltage is reversed to V_1 and the transient reversal current is measured. 45

Figure 3.2: Schematic of the particle tracking setup. The particles are tracked in the x-y plane. In the absence of EHD flow, the particle motion will be along the z axis and no significant change in the x-y position of the particle is expected while in the presence of EHD flow the motion of the particle will be multidimensional. 46

Figure 3.3: The measured reverse currents (colored dots) are compared with the simulated reverse currents (black lines) for device 1 (ϕ_m=0.0003 OLOA 11K, d = 4.0 μm, S = 1 cm^2 and λ =13) for 2 V→ -V_1, with V_1 = 0, 0.5, 1, 2, 5 and 7 V. For $V_1 \geq$1 V, after a short initial phase the currents are approximately constant until the transit time, after which they rapidly decrease and become very small..... 48

Figure 3.4: Measured (colored dots) and simulated (black lines) transient reversal currents for device 2 (ϕ_m = 0.003 of OLOA 11K in dodecane, d = 48.4 μm and S = 1 cm^2 and λ =17000) for 0.15 V→-V_1, with V_1 = 0, 0.15, 0.5, 1.5, 5, 15 and 50 V. The match between the measurements and the simulation validates the model. The simulation parameters are $\bar{n}$ = 10 μm^{-3} and μ = 1320 μm^2/Vs. 50

Figure 3.5: A comparison between measured (colored dots) and simulated (black lines) transient reversal currents for device 2 (ϕ_m = 0.003 of OLOA 11K in dodecane, d = 48.4 μm, S = 1 cm^2 and λ =17000) for 15 V→-V_1, with V_1 = 0, 0.15, 0.5, 1.5, 5, 15 and 50 V. The match between measured and simulated currents for smaller voltages validates the model. For larger voltages the peak in the measured currents occurs earlier than that of the simulations. Also, a second peak is observed in the measurements which does not match with the simulations. A detailed study about the origin and the

properties of CIMs relating to this peak is presented in chapters 5 and 6. The simulation parameters are $\bar{n}$ = 10 μm^{-3} and μ = 1320 μm^2/Vs. 51

Figure 3.6: Simulated variation in (a) the electric field and (b) concentration of positive CIMs as a function of time in device 2 (ϕ_m = 0.003 of OLOA 11K in dodecane, d = 48.4 μm, S = 1 cm^2 and λ =17000) for the reverse voltage step 15 V→-5 V. The corresponding measured reverse current is shown by green dots with the simulation in black line in Fig. 3.5. Positive CIMs travel from near the positive electrode (x = 48.4 μm) towards the negative electrode (x = 0). In (b) for the purpose of visibility, the limit of y axis is set to 40 μm^{-3}, nevertheless, the area under each curve is equal to $\bar{n} \times d$. The simulation parameters are $\bar{n}$ = 10 μm^{-3} and μ = 1320 μm^2/Vs. 52

Figure 3.7: Measured (colored dots) and simulated (black lines) transient reversal currents in device 2 (d = 48.4 μm and S = 1 cm^2 with ϕ_m = 0.003 of OLOA 11K in dodecane) for reverse voltage steps 15 V→-V_1 (8,10,12,15 V). The deviations before reaching the maximum current are ascribed to the occurrence of EHD instabilities. The simulation parameters are $\bar{n}$ = 10 μm^{-3} and μ = 1320 μm^2/Vs. 54

Figure 3.8: Transient trajectories in the *xy*-plane of positively charged PMMA tracer particles in device 2 (ϕ_m = 0.003 of OLOA 11K in dodecane) for polarizing voltages 0→V (black dots) and reverse voltages V→ -V (colored dots). The direction of motion is indicated by arrows. (a) For small voltages (V < 1.5 V) the lateral motion is small indicating the absence of EHD flow. (b) For large voltages (V > 1.5 V), the lateral motion is small for the polarizing voltage and large for the reverse voltage verifying the occurrence of EHD flow. 56

Figure 4.1: Schematic illustration of (a) a stepwise increasing voltage 0→V_0→V_1 (b) the charge generation process as a result of a disproportionation mechanism. 62

Figure 4.2: A comparison between the simulated (black line), analytically calculated (red line) and measured transient current (blue dots) for the device with $d = 19.5$ μm filled with ϕ_m of OLOA 11K in dodecane for a stepwise increasing voltage $V_0 \rightarrow V_1$. In (a) for $\phi_m = 0.1$, $\bar{n} = 439$ μm^{-3}, $V_0 = 30$ V and $V_1 = 60$ V. In (b) for $\phi_m = 0.03$, $\bar{n} = 70$ μm^{-3}, $V_0 = 3$ V and $V_1 = 10$ V. The level of the generation limited current (I_g) is shown by red color dots. In (c & d), the corresponding transient concentration variation of the generated positive (red color lines) and negative (blue lines) CIMs are shown at linearly spaced times, i.e. $t = j \times t_{gtr,1}$ with $j = 1, 2, \ldots, 10$. 69

Figure 4.3: Measured transient currents (colored dots) due to bulk generation of new charges are compared with the simulations (black lines) for $V_0 \rightarrow V_1$ performed on the device with d =19.5 μm and S = 1 cm^2. The device is filled with (a) ϕ_m = 0.01 (b) ϕ_m = 0.03 and (c) $\boldsymbol{\phi_m}$ = 0.1. 71

Figure 4.4: Linearly increasing equilibrium concentration of the initially present CIMs ($\bar{n}$) with increasing surfactant mass fraction verifies the disproportionation mechanism, as shown by the linear trend line (red line): $\bar{n} \cong 4500\,\mu\,\text{m}^{-3} \times \phi_m$. 72

Figure 4.5: The quasi steady-state current scales quadratically with ϕ_m (ϕ_m= 0.01, 0.03 & 0.1). The trend line (red line) shows $I_g = 3050 \times \phi_m^2$ nA. 73

Figure 4.6: The transient generation currents (color dots) are compared with the simulations (black lines) for ϕ_m = 0.1 and V_0=10 V and V_1= 20 V to 60 V from Fig. 2 (c) on linear and normalized axes. 73

Figure 5.1: Schematic illustration of the voltage versus time sequences for various types of transient current experiments. Type A: the duration t_0 is varied. Type B: repeated switching of the voltage. Type C: the short-circuit time t_{s1} is varied from 1 to 30 s. Type D: the bulk liquid is replaced by dodecane (clean) and V_3 is varied. Type E: t_{s4} is varied from 100 s to 5000 s. Type F: t_{s5} is varied from 500 s to 50000 s. 80

Figure 5.2: Reversal current measurement of type A for OLOA 11K in dodecane. (a) Reverse transient current for different durations t_0 of the polarization pulse for a device with d = 20 μm and ϕ_m = 0.003. (b) Integral of the second peak Q_{sp} on a semilogarithmic scale as a function of the duration of the polarizing voltage pulse, for different cell thicknesses d, with ϕ_m = 0.003. (c) Integral of the second peak Q_{sp} on a semilogarithmic scale as a function of the duration of the polarizing voltage pulse for different mass fraction ϕ_m for a device with d = 20 μm. The black lines show a linear fit with the experimental data. 82

Figure 5.3: Results of experiment type B showing the effects of the magnitude and duration of the oscillating voltage on the integral of the second peak. The experiments are performed in a device with d = 21 μm filled with ϕ_m = 0.003 of OLOA 11K in dodecane. In (a), for small voltages (V_0 & V_1 < 1V), the peak does not appear. In (b), for large voltages (V_0 & V_1 > 1 V) the contribution due to generated charges increases with increasing number of voltage cycles, therefore an increasing peak is observed until it reaches a saturation level. In (c), the integral of the second peak increases linearly (black lines) with increasing number of voltage cycles and the saturation level/linear trend line of the integral is independent of the magnitude of the applied voltage (V_0 & V_1 > 1 V). T is the total duration for which the oscillating voltage is applied. 83

Figure 5.4: Transient current measurements ($|I|$) in response to a voltage step $0 \rightarrow \pm V_{2,3}$ ($V_{2,3}$ = 5 V) performed in the device with d = 20 μm filled with a surfactant mixture of ϕ_m = 0.003. In (a) the results of the experiment of type C show the effect of the relaxation time (t_{s1}) on the current peak while in (b) the results of the experiment of type D show the effect of the polarizing voltage step duration (t_0) on the duration of the plateau current between 0.03 and 1s for $t_0 \geq$ 500s. 86

Figure 5.5: A comparison between transient current measurements (color dots) and the currents calculated from the Mott-Gurney equation (black lines) for the type D experiment

(d = 20 μm filled with ϕ_m = 0.003 for 0→V_0). (a) In response to the voltage step 0→V_3. (b) For 0→-V_3 and (c) for 5 V→-V_3. The measured currents are in agreement with the Mott-Gurney equation up to the time t^* and then decrease rapidly. The fitting parameters are: μ = 1320 μm^2/Vs and N_{SCIMs} = 500 μm^{-2} (Q^*= 8 nC) respectively 88

Figure 5.6: Measured currents of the polarizing voltage step 0→V_0 in the case that one substrate has been replaced, for a cell with d = 20 μm filled with ϕ_m = 0.003. There is only a significant current when the applied voltage step is negative. 90

Figure 5.7: In (A) various steps (1-6) of the experiment are depicted. In (B) the outcome of each step (a-f) of the experiment is illustrated with the location and motion of regular CIMs (blue and red circles) and generated CIMs (green and cyan circles) (a): initial situation (only regular CIMs), (b): polarizing step, (c): after short circuit of t_s = 3 s, (d): after short circuit of t_s = 30 s, (e): after removing the regular and neutral CIMs (type B), (f): voltage step after cleaning, (g): after replacing the bottom substrate. In (B (b-g)), the generated positive SCIMs are not shown because they never release from the electrode. 91

Figure 5.8: Schematic illustration of the six different types of charged and neutral IMs. The main physical difference between CIMs is the location of the charge. The generated CIM in which the charge is very close to the outside (100 % of the positive and 95 % of the negative generated CIMs) are attracted strongly by the electrodes and are never released. The CIMs in which the charge is more towards the center (5 % of the generated negative CIMS) or in the center (regular CIMs) are released when the voltage is reversed or switched off. 92

Figure 5.9: Results of the experiment types E (a & b) and F (c & d), which show the decay of SCIMs generated during a polarizing voltage step (0→V_0) of 10000 s in a device with d = 20 μm and filled with OLOA 11K in dodecane. In (a), the decreasing peak as a function of the short

circuit duration t_{s4} shows the decrease of SCIMs over time in the presence of regular CIMs and neutral inverse micelles for $\phi_m = 0.003$. In (b), the integral of the peak is plotted on a semilogorithmic scale (color symbols) as a function of the short circuit duration t_{s4} and fitted with an exponent (black lines). In (c), the decreasing currents with increasing short circuit time t_{s5} represent how the number of SCIMs decreases over time for the experiment type F. In (d), the decreasing integral of the currents from (c) (color symbols) are shown on a semilogorithimic scale, and fitted with an exponential (black lines), revealing a slower decrease in numbers of SCIMs. 94

Figure 6.1: Schematic representation of the measurement device with two parallel electrodes separated at a distance d with an overlapping area S = 1 cm^2. The device is filled with a suspension of OLOA 11K in dodecane. The regular CIMs are depicted by red and blue color circles while the generated CIMs are depicted by cyan and yellow color circles. In (a), in response to a polarizing voltage step ($0 \rightarrow V_0$), the formation of diffuse double layers for the regular CIMs and interface layers for the newly generated CIMs (light magenta color) is illustrated. The SCIMs in the interface layer are shown in cyan, the other adsorbed CIMs are not shown In (b), the release of the regular CIMs and SCIMs is depicted when the voltage is reversed ($V_0 \rightarrow -V_1$) rapidly after a polarizing voltage step. In (c), intact interface layers with SCIMs are illustrated after cleaning the device..... 104

Figure 6.2: Measured currents (colored dots) for the experiment type A are compared with the simulated currents (black lines) for a device with d = 20 µm which was filled with a suspension (a) ϕ_m = 0.003 (b) ϕ_m = 0.006 of OLOA 11K in dodecane. The full colored lines show the calculated currents using Eq.6.17 : $\frac{\varepsilon_o \varepsilon_r S V_1}{d^2} \sqrt{\frac{\mu k_B T}{2et}}$. The constant currents (I_{ss}) shown by dotted color lines match with the Mott-Gurney Eq. 6.23 showing a V_1^2 dependency. 108

Figure 6.3: Simulated transient profile of (a) the electric field (b) the concentration of the released SCIMs for the experiment

type A in a device with d = 20 µm with ϕ_m = 0.003. The SCIMs are released from the interface layer situated at the right electrode (shown by a red line) clamping the field to zero. The stationary state is reached around 45 ms and lasts up to 800 ms. The simulation parameters are: μ =1320 µm^2/Vs and N_{SCIMs}= 500 µm^{-2} 109

Figure 6.4: Measured transient currents $|I|$ (colored dots) for the experiment type B are compared with the simulated currents (black lines) for 5 V→-V_2. The measurements are performed on devices with thickness d filled with a suspension of OLOA 11K in dodecane (a) d = 20 µm with ϕ_m = 0.001) (b) d = 20 µm with ϕ_m = 0.003 (c) d = 46 µm with ϕ_m = 0.001 (d) d = 46 µm with ϕ_m = 0.003. 111

Figure 6.5: Simulated transient profile of (a) the electric field (b) the concentration of the regular CIMs and SCIMs for the experiment type B in a device with d = 20 µm filled with a suspension ϕ_m = 0.001 OLOA 11K in dodecane. The SCIMs are released from the interface layer situated at the left electrode shown by red vertical line. The SCIMs are released when the field changes sign at the boundary of the interface layer towards the bulk. The simulation parameters are: μ =1320 µm^2/Vs, $\bar{n}$ = 3.6 µm^{-3} and N_{SCIMs}= 500 µm^{-2} 112

Figure 7.1: Schematic of the HFTC setup. The setup comprises (a & a') the liquid toner cell with two circular electrodes, (b, c) filling and closing of the electrodes of the toner cell. (d) A temperature sensor is used to monitor the temperature of the cell (e) The Keithley source meter is used to apply a voltage and to measure the corresponding current simultaneously. (f) A pc is used to control the electronics of the setup and to display the current-voltage profile. 121

Figure 7.2: (a) The single particle tracking set up. (b) A glass substrate with ITO interdigitated electrodes. A thin layer of liquid toner is deposited on the substrate and placed underneath the microscope objective and an area is brought into focus. Then a ac/dc voltage is applied across the electrodes and images are acquired..... 122

Figure 7.3: Schematic illustration of the measurement setup with two parallel circular steel plates with area S separated at a distance d. The space between the electrodes is filled with a prepared dispersion and then a triangular voltage of 5 Hz is applied across the electrodes 124

Figure 7.4: The measured currents for the experiment type A (red color dots) for a solution of Solsperse $\phi_m = 0.0005$ in lytol using the HFTC setup with d = 40 μm and S = 4.93 cm^2 are compared with simulated currents (black lines) for triangular wave voltages of frequency 5 Hz. The peak values of the applied voltages are (a) V_p = 5 V (b) V_p = 50 V (c) V_p = 100 V (d) V_p = 200 V (e) V_p = 300 V (f) V_p = 400 V. The values of simulation parameters are: μ = 210 $\mu m^2/Vs$ and $\bar{n}$ =7.5 μm^{-3}. 127

Figure 7.5: (a) The variation of the mobility of Solsperse CIMs in lytol with ϕ_m. (b) The linearly increasing concentration on logarithmic axes of the CIMs with ϕ_m verifies the bulk disproportionation mechanism and the black line shows the trend line: $\bar{n} = 16500 \times \phi_m\ \mu m^{-3}$..... 129

Figure 7.6: The simulated variations in the electric field (a & c) and the concentration of the positive CIMs (b & d) between the electrodes in response to a triangular voltage $0 \rightarrow V(t)$ for a duration of 0.1 s. The electrodes are separated at a distance d = 40 μm and have an overlapping area of S = 4.93 cm^2. For (a, b), the peak value of the applied voltage is 50 V while for (c, d), the peak value of the applied voltage is 400 V. The values of simulation parameters are: μ = 210 $\mu m^2/Vs$ and $\bar{n}$ =7.5 μm^{-3}..... 130

Figure 7.7: The measured current and the applied voltage in the experiment types A and B are shown. All the cycles of the current measured with the HFTC setup (S = 4.63 cm^2 and d = 40 μm) in response to a triangular voltage ($0 \rightarrow V(t)$, $V(t) \rightarrow -V(t)$ and $-V(t) \rightarrow V(t)$) of 5 Hz with a total duration of 2.3 s are placed one over another. The measured current for the first quarter cycle of the voltage ($0 \rightarrow V(t)$), during which the charges move from a uniform distribution, is shown by a red line (0.05 to 0. 1 s). (a & b) show the currents for a solution of Solsperse with $\phi_m = 0.0005$ in lytol (without toner

particles) in response to V_p = 100 V and V_p = 400 V respectively. (c)- (f) Measured currents for a dispersion with $\phi_m = 0.2$ of toner particles and $\phi_m = 0.001$ of Solsperse in lytol for V_p =(c) 100 V (d) 200 V (e) 300 V and (f) 400 V. For increasing V_p, a second peak in the interval t = [0.05 to 0.067 s] is observed in the current (inset figure in d, e & f). This peak is related to effects of the interfaces on the liquid toner particles and the peak increases each period until it reaches saturation. 132

Figure 7.8: The integral of the current (shown in Fig. 7.7) after the capacitive part is subtracted is plotted as a function of time. The filled data points show the integral of the current for $-V(t) \rightarrow V(t)$ while the empty data points show the same for $V(t) \rightarrow -V(t)$. In (a) the integral of the current peaks for a solution of $\phi_m = 0.0005$ Solsperse in lytol (black color symbols) is compared with the integral of the current peaks for a mixture of Solsperse ($\phi_m = 0.001$) and toner particles ($\phi_m = 0.2$) in lytol (blue color) for V_p = 400 V. In (b), the integral of the current peaks for a mixture of Solsperse ($\phi_m = 0.001$) and toner particles ($\phi_m = 0.2$) in lytol. In (c), the integral of the current peak due to the particles is plotted from Fig. 7.7 (d, e & f). 134

Figure 7.9: Results of experiment type E (a) the trajectory of a single liquid toner particle in the 'x' direction without and with a sinusoidal voltage of V_p = 50 V with a frequency of 10Hz. (b) Histogram of the hydrodynamic radius of 100 liquid toner particles estimated from the Brownian motion of particles for a duration of 2 s. (c) The mobility histogram of 90 liquid toner particles. The particles with zero mobility are not included in the mobility histogram. 136

Figure 7.10: The result of the experiment type C for which the original liquid toner is diluted to 50% in lytol. In (a) all cycles of the current measured with the HFTC setup (S = 4.63 cm^2 and d = 40 μm) in response to a triangular voltage with V_p = 400 V ($0 \rightarrow V(t)$, $V(t) \rightarrow -V(t)$ and $-V(t) \rightarrow V(t)$) of 5 Hz with a total duration of 2.3 s are placed one over another. The measured current for the first quarter cycle of the voltage ($0 \rightarrow V(t)$), during which

the charges move from a uniform distribution, is shown by red dots (0.05 to 0. 1 s). Also, the current measured using the same device for a solution of Solsperse ϕ_m = 0.0005 in lytol during the 23 voltage cycle is shown by a black color line with black dots In (b), the corresponding integral of the current by subtracting the capacitive jump are plotted as a function of peak voltage. The filled data points show the integral of the current for *-V(t)→V(t)* while the empty data points show the same for *V(t)→ -V(t)*. Clearly, with increasing number of the voltage cycles, the integral of the current increases for a few cycles and then saturates. 138

Figure 7.11: Schematic depiction of the various steps of the proposed desorption mechanism at an interface for a triangular voltage of V_p = 400 V with f = 5 Hz. In (a), at t = 0 s, the charged particles are uniformly distributed in the device t < 0 s). In (b) in response to the voltage the charged particles start to move to the opposite polarity electrodes. In (c), when the charged particle contacts the opposite polarity electrode, then the counter CIMs are desorbed (shown by black circles) form the particles leading to an increase of the particles charge..... 140

Figure 7.12: A comparison between the measurement (red dots) and simulations (black line) for the dispersion with CIMs and particles (Type B). The measured currents are from Fig. 7.7 (f) for t = [0, 0.1 s] and t = [2.2, 2.3s] (the duration for which the small peak between t = 2.25 to 2.26 s is saturated) are combined and plotted in the same figure for a complete period of the voltage (V_p = 400 V and f = 5 Hz). In (a), the measured currents are compared with the first type of simulation. In (b), the same measured currents are compared with the second type simulation. The simulation in (b) matches quite well with the measurement from t = 0 to 0.16 s. The match between the measurement and the simulation for the peak observed between t = 0.1 to 0.16 s, indicates that the peak is due to fast particles which have mobility 4000 $\mu m^2/Vs$. 142

Figure 7.13: Result of experiment type D on undiluted liquid toner for a triangular wave voltage of -400 V to 400 V with

frequency 5 Hz. In (a) the absolute value of the current measured for $0 \rightarrow V(t), -V(t) \rightarrow V(t)$ and $V(t) \rightarrow -V(t)$ are placed one over another. With increasing number of cycles an increasing peak is observed in the current. In (b) the integral of each peak is plotted as a function of time. The filled color symbols show the calculated integral of the current for $-V(t) \rightarrow V(t)$ while the unfilled symbols show the same for $V(t) \rightarrow -V(t)$. 144

Figure 7.14: Results of experiment type F showing the effect of a DC voltage of 300 V on a layer of liquid toner on ITO interdigitated electrodes with spacing d = 200 μm. The electrodes are indicated by the space between red or green lines and the polarity of the applied voltage on the corresponding electrode is indicated by a plus or minus sign next to them. In (a, c) the time and voltage sequence is shown while in (b, d) the microscope transmission images which are acquired during 0 to 21 s (c) and 28 to 49 s (d) are combined by integrating the intensity of each image along the x direction. The dark areas in the image indicate the presence of particles. In (c) from t = 0 to 2 s, when no voltage is applied across the electrodes, the particles are relatively uniformly distributed between the electrodes and at t = 2 s the voltage is applied and the particles move to the electrodes with opposite sign (dashed green box). The region in the white dashed box shows that there is a change in the concentration of particles near the electrodes. This change corresponds to particle charging due to charge injection from the electrodes. After a duration of 21 s, the electrodes are short circuited for a few seconds, then in (d) again the same voltage is applied at t = 30 s. The gray areas next to the negative electrodes indicate that most of the particles are near the negative electrodes at this time. With increasing duration of the voltage, a few lines can be seen between the electrodes, these lines correspond to particles of which the charge is inverted due to charge injection from the electrodes. 145

List of Symbols

Symbol	Unit	Description
c	$molm^{-3}$	Concentration of a surfactant in a mixture
C	F	Electric capacitance
d	m	Separation between electrodes
D	m^2s^{-1}	Diffusion constant of charged and neutral inverse micelles
e	C	Electronic charge
E	Vm^{-1}	Electric field
f	Hz	Frequency
G_A	J	Van Der Waals interaction energy
G_{el}	J	Electrostatic interaction energy
G_T	J	Total interaction energy
I	A	Current
I_{ss}	A	Stationary state currents
I_{DL}	A	Double layer re-arrangement current
J	Am^{-2}	Current density
k_B	JK^{-1}	Boltzmann's constant
K	No Unit	Equilibrium constant
$\bar{n}_0$	m^{-3}	Concentration of neutral inverse micelles at equilibrium
n_0	m^{-3}	Concentration of neutral micelles
$\bar{n}$	m^{-3}	Concentration of charged inverse micelles at equilibrium
$n_{\pm}$	m^{-3}	Concentration of positive and negative charged inverse micelles
$n_{tot\pm}$	m^{-3}	Sum of the concentration of initial

		present charged inverse micelles in the bulk
$n_{g\pm}$	m^{-3}	Concentration of newly generated positive and negative charged inverse micelles in the presence of an electric field
n_{s+}	m^{-3}	Concentration of generated positive sticky charged inverse micelles
n_{s-}	m^{-3}	Concentration of generated negative sticky charged inverse micelles
n_{SCIMs}	m^{-3}	Concentration of generated special charged inverse micelles
N_{SCIMs}	m^{-2}	Density of SCIMs at interface layer
$N_{g\pm}$	No Unit	Number of generated charged inverse micelles during the transient
Q_{el}	C	Charge density on an electrode
r_d	m	Distance between two identical molecules
r	m	Radius of charged inverse micelles
R	m	Center to center distance between two spheres
$\langle R_i^2 \rangle$	m^2	Mean square displacement
S	m^2	Areas of electrode
t	s	Time
t_0	s	Duration of a polarizing voltage step
t_1	s	Duration of a reversal voltage step
$t_{tr,i}$	s	Transit time
t_{si}	s	Short circuit duration
t_{ss}	s	Duration of stationary state current
T	K	Absolute temperature
v	ms^{-1}	Velocity
v_{Diff}	ms^{-1}	Average diffusion speed
V_p	Volt	Peak voltage
V_0	Volt	A polarizing voltage step
V_1	Volt	A step wise increasing or reversal voltage step
x	m	Distance
X_{diff}	m	Average displacement from an initial position
π	No Unit	Mathematical constant
η	mPas	Dynamic viscosity
σ	Sm^{-1}	Electrical conductivity
ε_0	Fm^{-1}	Vacuum permittivity

ε_r	No Unit	Relative permittivity
λ_B	m	Bjerrum length
ϕ_m	No Unit	Weight fraction of a surfactant in a mixture
χ	No Unit	Fraction of charged inverse micelles in a mixture
β_{11}	Jm^6	Van der Waals interaction constant
κ	m^{-1}	Debye Hückel parameter
ς	V	Zeta potential
Ψ_0, Ψ_s	V	Potential
ρ	Cm^{-3}	Space charge density
β	m^3s^{-1}	Generation rate constant
α	m^3s^{-1}	Recombination rate constant
$\Psi_{\pm}$	$m^{-2}s^{-1}$	Flux due to initially present charged inverse micelles
$\Psi_{g\pm}$	$m^{-2}s^{-1}$	Flux of newly generated charged inverse micelles
Ψ_{s+}	$m^{-2}s^{-1}$	Flux of newly generated positive sticky charged inverse micelles
Ψ_{s-}	$m^{-2}s^{-1}$	Flux of newly generated negative sticky charged inverse micelles
Ψ_{SCIMs}	$m^{-2}s^{-1}$	Flux of newly generated special charged inverse micelles
μ	$m^2V^{-1}s^{-1}$	Mobility of the initially present charged inverse micelles
μ_g	$m^2V^{-1}s^{-1}$	Mobility of newly generated charged inverse micelles
Δ	m	Thickness of interface layers
λ	No Unit	Normalized charge content of a device
φ_i	No Unit	Ratio of the applied voltage and thermal voltage
$\delta(t)$	s^{-1}	Dirac delta function
λ_{DL}	m	Debye length
τ_{DL}	s	Double layer charging time
Δt	s	Time step

List of Abbreviations

Abbreviation	Description
EPDs	Electrophoretic displays
IP-EPDs	In plane electrophoretic displays
V-EPDs	Vertical electrophoretic displays
DLVO	Deryaguin-Landau-Verwey and Overbeek
IMs	Inverse micelles
CIMs	Charged inverse micelles
ITO	Indium tin oxide
HFTC	High field toner cell
PIBS	Polyisobutylene succinimide
PNP	Poisson-Nernst-Planck
EHD	Electrohydrodynamics
PMMA	poly (methyl methacrylate)
SCIMs	Special charged inverse micelles

Chapter 1

Introduction

Displaying information electronically is part of our daily life, but consumes a lot of energy. Most of the display technologies today use a backlight. Nevertheless, there is a technology known as electrophoretic displays (EPDs) that is based on the movement of charged pigment particles in a liquid under the influence of an electric field. EPDs look very similar to printed paper: they are based on the scattering of ambient light and do not require a backlight. In addition to their very low power consumption, EPDs have many advantages over the conventional LCDs/LEDs, such as a large viewing angle, bi-stability and a high contrast under direct sunlight. The main disadvantages are slow switching speed and low color saturation.

The same principle of controlling pigment in a liquid by applying electric fields is used in a relatively new technology for industrial printing. This so-called “liquid toner printing” has many advantages over the more common dry toner based printing, such as a higher resolution, sharper image edges and higher printing speed. Despite of these advantages, liquid toner based printing is still under development and covers only a small market. A better understanding of electrokinetics in non-polar liquids is needed in order to develop liquid toner printing into a mature technology.

In order to tackle the challenges of both EPDs and liquid toner printing, fundamental processes in nonpolar liquids, such as particle charging, charge stabilization and the behavior of charge at interfaces, need to be understood better. This dissertation is primarily motivated by the above mentioned problems of EPDs/liquid toners and particularly focuses on the electrodynamics and interfacial behavior of charges in EPDs/liquid toner-like systems.

In addition to providing the background for upcoming chapters, this chapter also provides details of the physical principles and material properties on which EPD technology is based. As is clear from the name, EPD is a technology based on the controlled movement of charges in a liquid in response to an applied electric field. In the first section of this chapter, details about the types of liquid and the mechanisms leading to stable charge in a liquid are provided. Afterwards, several applications of non-polar liquids are discussed. In the subsequent sections, charging and charge stabilization in an EPD-like system is described.

1.1 Formation of Charge in Liquids

Liquids can be polar or non-polar depending on the molecular structure and the distribution of electric charge within the constituent molecules. Polar molecules have a permanent dipole moment, the most common example being water. However, in the absence of an electric field, the dipole moments of the molecules cancel out due to the random orientation of molecules throughout the liquid. Non-polar molecules do not have a permanent dipole moment due to coinciding centers of positive and negative charges in the molecules, with a typical example being alkanes.

A liquid between two charges affects the electric field and force between them, because of the alignation of (induced) dipoles. The effect of matter on the field intensity is defined by the electric polarizibility or by the relative dielectric constant (ε_r).On the basis of the relative dielectric constant, liquids are broadly categorized in three categories: polar ($\varepsilon_r > 40$), weakly polar ($\varepsilon_r > 5$), and non-polar ($\varepsilon_r < 5$) liquids [1].

The presence of charge in a liquid can be assessed on the basis of the Bjerrum length, which is the distance at which the electrostatic interaction between two opposite ions is balanced by thermal energy [2,3]. In other words, the Bjerrum length is the minimum distance between two opposite ions allowing them to remain stable and out of range of the electrostatic binding force. The Bjerrum length (λ_B) is expressed as [4]:

$$\lambda_B = \frac{z_1 z_2 e^2}{4\pi\varepsilon_0\varepsilon_r k_B T} \tag{1.1}$$

Here, z_1, z_2 are the valencies of the ions, e is the elementary charge (C), ε_0 = 8.85×10^{-12} Fm^{-1} is the vacuum permittivity, k_B = 1.38×10^{-23} JK^{-1} is Boltzmann's constant and T is the absolute temperature (K). The Bjerrum length of symmetric univalent ions in a polar medium such as water ($\varepsilon_r = 78$) can be calculated using Eq. 1.1 to be 0.71 nm while that in a non-polar medium such as dodecane ($\varepsilon_r = 2$) is 28 nm. When a symmetric univalent electrolyte such as NaCl is dissolved in water, a hydration shell of a width comparable to the Bjerrum length is formed around the ions (Na^+ and Cl^-) which stabilize them and prevent their association. However, in non-polar liquids the large Bjerrum length prevents ions from separating, therefore the presence of free ions is expected to be insignificant. Similarly, particle charging is not expected in non-polar liquids [3]. Nevertheless, due to the presence of amphiphilic molecules, most commonly surfactants, non-polar liquids can exhibit surprisingly strong charge related effects [2,4,5–14,15–27] which are being used in many applications, some of which are listed in the next section.

1.2 Applications of Non-Polar Colloids

The ability to control the conductivity of non-polar liquids by the addition of a surfactant has many practical and industrial implications, such as in oil refineries [16,28], drug delivery system [29], liquid toner [30], electrorheological fluids [31,32], development of new crystalline materials [32–37], electrostatic lithography, inkjet printing, photo electrophoresis and electrophoretic displays [14,38–42]. In most of these applications, particles are dispersed in a non-polar liquid and a surfactant is added to electrically charge and to stabilize the particles in the dispersion [3]. How precisely surfactants cause charging and stabilization is

discussed in sections 1.4, 1.5 and 1.6. Since this work is largely motivated by electrophoretic display and liquid toner applications, in the following section the working principle, the advantages and the disadvantages for each of them are described.

1.2.1 Electrophoretic Displays (EPDs)

Electrophoretic displays (EPD) are a display technology that might evolve into low-cost, low-power, full-color, paper-like, flexible displays with video capabilities [43]. The main advantages of EPDs over other displays are low power consumption, light weight, flexibility [44], high contrast under ambient light, large viewing angles, image bi-stability and an appearance similar to that of ink on paper [14,38,39,41,45,46]. At this moment, the main drawbacks of EPDs are a long response time (larger than 100 ms [47]), poor/unstable reflective grayscale reproducibility, flicker and ghost images [43].

Electrophoretic displays are based on the movement of charged particles dispersed in a non-polar liquid induced by an electric field. Based on the direction of movement of the particles in an EPD, EPDs can be categorized as vertical plane EPD (V-EPD) and horizontal or in plane EPD (IP-EPD). The parameters which generally define the performance of EPDs are the liquid viscosity, the charge on the particles, and the separation between the electrodes (d). In the following, the working principle with advantages and downsides of each type of EPD are discussed.

Typically, each pixel of a vertical plane EPD consists of many microcapsules filled with a mixture of black and white particles and surfactant in a non-polar solvent [38,39], as shown in Fig.1.1. The surfactant and the particles are chosen in such way that the white particles and the black particles become oppositely charged (e.g. positively charged white particles and negatively charged black particles) [3]. The diameter of the capsules varies from 30 μm to 300 μm while the diameter of the particles is around 1 μm [39]. The capsule is sandwiched between two parallel electrodes, one of which is transparent. Upon application of a voltage, the charged particles inside the capsules move towards the opposite polarity electrode. The black particles absorb light resulting in a dark pixel while the white particles scatter light resulting in a white pixel. The white state is achieved through diffuse scattering of the light, therefore a large difference

in refractive index between the white particles and the surrounding liquid is important [39,46]. The size of the particles or scattering structure (refractive index variation and surface roughness) is chosen in the order of the wavelength of visible light to maximize the scattering of light [39,46].

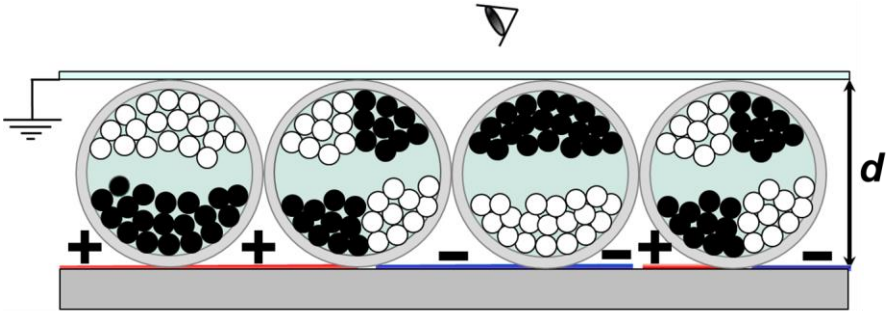

Figure 1.1: Each pixel in an EPD consists of microcapsules filled with negatively charged black and positively charged white particles in a non-polar liquid. In response to a voltage, the positively charged white and negatively charged black particles move to opposite electrodes resulting in black and white pixels.

Continuous efforts are being made to realize high-quality full color V-EPDs. A simple approach to achieve a color display is by adding a color filter array (CFA) onto an essentially monochrome display. A limited success is achieved through this approach because color filters absorb light and thereby reduce reflectivity. Furthermore, only side-by-side combinations of the primary colors are achieved by the filter, which results in reduced resolution, color saturation and brightness of the pixels [46]. Another approach in which side-by-side color reflective displays are used instead of using a CFA, results in a more reflective white state and compromised colors. Recently, E-ink has introduced “advance color epaper” (ACeP) displays in which eight colors have been achieved. ACeP is based on three transparent charged pigments and a white scattering charged pigment. The controlled movement of the pigments results in color modulation [48]. However, in terms of color display quality and video imaging V-EPDs are still in the development stage and much more work needs to be done in this direction [43]. A few devices which are based on V-EPDs are shown in Fig. 1.2.

Figure 1.2: A few devices based on V-EPDs are shown. In (a) the Amazon Kindle ebook reader is an example of a typical monochrome reflective display featuring low power consumption (b) the Sony E-ink based tablet: Sony DPTS1 digital paper system (c) E ink's triton color EPD offers 16 levels of gray scale and is able to displays 4096 colors – be it in a poor color quality (d) Plastic logic e-ink based flexible displays (d) Motorola Motofone (e) Sony's FES e-ink based watches.

An alternative approach to achieve a display similar to printed paper is an in-plane EPD (IP-EPD) [42]. In contrast to V-EPDs, in IP-EPDs the EPD is filled with a non-polar liquid containing charged particles. Similar to a V-EPD, in an IP-EPD the dark state is achieved by the absorption of light by the dispersed particles uniformly in the cell [43]. A white state however is achieved by collecting the charged particles in a small area next to the electrodes on an application of a voltage, which allows the light to pass through the cell/pixel [43], see Fig. 1.3. Color can be achieved by subtractive color mixing and with multi-layer stacks of the cell on top of a white reflector, see Fig. 1.3. Each cell contains a dispersion of colored particles (generally cyan, magenta, yellow and black). Since each cell can be switched to a transparent state by application of a voltage all color combinations can be achieved [41].

The main advantage of IP-EPDs over V-EPDs is their ability to create highly saturated color without the use of color filters [43]. The main drawback is that to have a clear transparent state, the distance between the electrodes must be very large which reduces the switching speed of the particles (since the switching time scales quadratically with the electrode separation $t = d^2/\mu V$, d is the distance between the electrodes, μ is the mobility of charged particles and V is the applied voltage). For applications in which a static image is to be displayed for a long time, such as product labeling, IP-EPDs are the suitable choice.

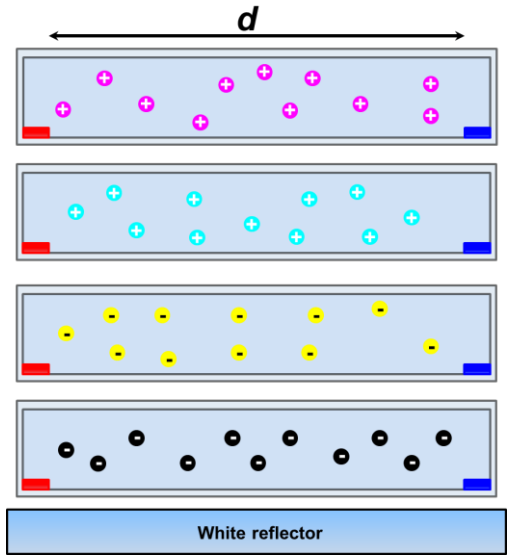

Figure 1.3: Schematic illustration of four-stacked cell of an IP-EPD. Each cell contains charged color particles dispersed in a non-polar liquid and the electrodes are situated inside at the edges of the cell.

1.2.2 Liquid Toner

Liquid toners are an alternative to the dry toners that are used in most xerographic copiers and printers. Liquid toners are dispersions consisting of charged pigment particles dispersed in a dielectric liquid while dry toners are powders of pigment particles that get charged triboelectrically or by adding a surface active agent [30,49,50]. The main difference between liquid and dry toner (apart from the fact that one is liquid and the other is not) is the size of the pigment particles. The size of dry toner particles has to be above a

critical size limit of at least 5 to 9 μm, otherwise they form a dust cloud which poses controlling problems in the printing process [51]. There is no size limitation for liquid toner particles. Generally for standard printing the size varies from 1 μm to 2 μm. The small size of liquid toner particles offers many advantages over dry toner such as high-resolution imaging, uniform gloss, sharp image edges and very thin image layers [51]. Furthermore, liquid toner printing allows high printing speeds of up to 56 meters/min (4 colors (HP indigo 10000, Fig. 1.4)) [51] while the maximum reported color printing speed of a dry toner based printer is 21.5 meter/s (Xeikon 9800). Special efforts are being made to use vegetable oil as a carrier liquid (HP Indigo and XEIKON Trillium) so that the printing process is more environmentally friendly. Despite of these advantages, liquid toner printing is still in its infancy and there are many fundamental/practical issues that are not solved yet.

Figure 1.4: An example of a printer based on liquid toner (HP indigo 10000 digital press) [51].

1.3 Surfactants

Because of the many practical and industrial implications, non-polar dispersions have been investigated intensively during the past decade using various techniques based on electrical and optical methods [10,14,24,27,28,52,53]. The aim of all these investigations is to understand the fundamental mechanisms of surfactant mediated charging and charge stabilization in non-polar dispersions. These studies have provided a good understanding about non-polar dispersions. In this and the following sections, an overview of various existing theories on surfactant

mediated charging and particle stabilization in non-polar dispersions is presented.

Before going into detail about surfactant mediated charging mechanisms, it is relevant to have a good understanding about surfactant molecules, types of surfactants and the behavior of surfactants in non-polar liquids. A surfactant molecule consists of a polar and a non-polar part. In general, the polar part (called the head) is hydrophilic while the non-polar part (tail) is lipophilic. Due to the amphiphilic nature they tend to be adsorbed at interfaces. For example in a system with oil and water, the surfactant molecules orient themselves in such a way that the hydrophilic head is in the water and the lipophilic tail is in the oil. The tail of surfactants is usually similar from one surfactant to another and is typically made of a chain of carbon and hydrogen. The heads show a range of chemical types. On the basis of the polar head group, the chemical structure of surfactant can be categorized as ionic, non-ionic or amphoteric. A few examples are shown in Fig. 1.5. If the head group of a surfactant molecule is positively or negatively charged in the solvent then the surfactant is ionic. If the head groups are both positive and negative then the surfactant is amphoteric or zwitterionic and if it does not carry any charge then the surfactant is nonionic [54,55].

When a surfactant is introduced in a non-polar liquid as a solute, due to the highly non-polar environment the polar heads of the surfactant molecules attract one another and tend to aggregate. The structure of aggregated surfactants is known as an inverse micelle (IM). For low concentrations of surfactant and in the absence of impurities, the shape of IMs usually is spherical [3,6,11,12,19,20]. The IMs comprise a polar core and a non-polar shell. The polar interior of inverse micelles offers an environment for various chemical and biological reactions that do not occur in normal conditions [56]. The driving force for the formation of inverse micelles is a decrease in enthalpy of the system as a result of attraction between polar head groups [3].

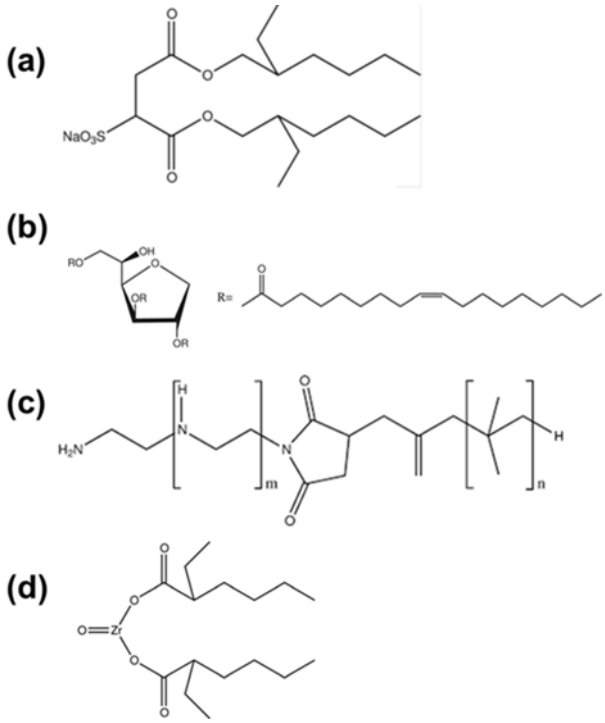

Figure 1.5: A few commonly used and studied surfactants: (a) anionic Sodium dioctylsulfosuccinate (Aerosol OT) (b) nonionic sorbitan trioleate (Sorb) (c) nonionic polyisobutylene succinimide (PIBS) (d) anionic zirconyl 2-ethyl hexanoate (Zr(Oct)2) [20,27].

1.4 Charge Formation in Non-Polar Liquid With Surfactant

Free ions can exist in non-polar liquids only if they are encapsulated by a structure of a size in the order of the Bjerrum length that can prevent them from re-associating [2,3,6,25]. When the concentration of an added surfactant is above a certain value known as the critical micelle concentration (CMC), inverse micelles (IMs) are formed in the liquid [3,12,19]. The IMs are structures which can stabilize charge in their core. If the size of inverse micelles is larger than the Bjerrum length, then all ions inside such IMs will be stabilized [12]. If the size is smaller than the Bjerrum length then an equilibrium between charged and uncharged IMs exists [3]. How micellar ions form in a non-polar liquid with added

surfactant is a subject of debate [2,3,25]. In general, there are two theories which explain the origin of charges in non-polar liquids with surfactant.

1.4.1 Dissociation Mechanism

According to the dissociation theory, charged inverse micelles (CIMs) can be formed in the liquid because of the dissociation of surfactant molecules or impurities [24,25]. The stabilization of dissociated ions in inverse micelles happens very easily, so that all ions are stabilized. The dissociation of a molecule can be expressed as:

$$AB \rightleftharpoons A^+ + B^- \tag{1.2}$$

Applying the law of mass action, the concentrations of CIMs are:

$$n_+ = n_- = \sqrt{Kc} \tag{1.3}$$

Here, c is the concentration of surfactant in the liquid (that is assumed to be proportional to the concentration of ionizable molecules) K is the equilibrium constant and $n_+ = n_-$ is the concentration of CIMs. According to this theory, the concentration of CIMs scales with the square root of the concentration of surfactant present in the liquid. This behavior has been verified in some surfactant systems when the concentration of the surfactant is very low [19]. However, for larger concentrations of surfactants, the validity of this theory is a subject of debate [25].

1.4.2 Disproportionation Mechanism

According to the disproportionation theory, the collision of two neutral micelles via Brownian motion results in an intermediate hypothetical structure, which then again splits into two oppositely charged inverse micelles (CIMs), as depicted in Fig. 1.6. Similarly, the reverse process in which the collision of two oppositely charged micelles results in two neutral micelles is also possible [12,19,23,57]. However, the existence of this intermediate structure is never verified experimentally. The disproportionation of two micelles can be written as:

$$2A \rightleftharpoons A^+ + A^- \tag{1.4}$$

Applying the law of mass action, the concentration of charged inverse micelles in equilibrium can be obtained as:

$$n_+ = n_- = \bar{n} = \sqrt{K}\, n_0 \tag{1.5}$$

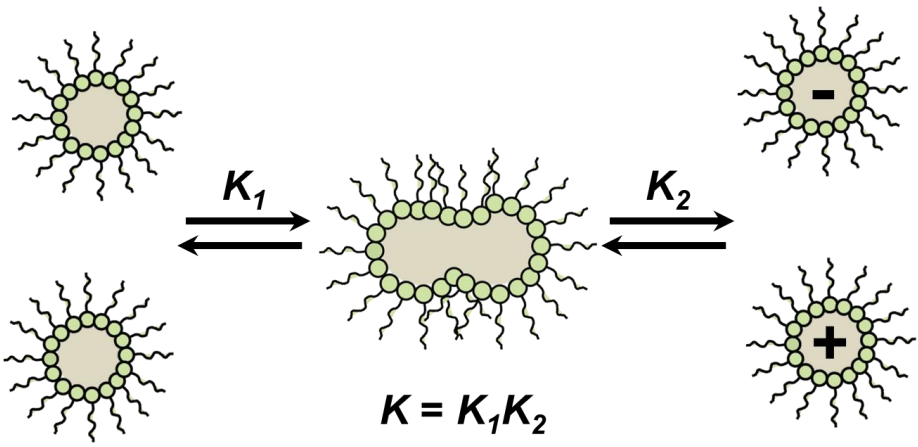

Figure 1.6: Illustration of the disproportionation mechanism in which a collision of two neutral micelles results in an intermediate hypothetical structure that then splits into two oppositely charged inverse micelles.

If disproportionation is the charging mechanism, then according to Eq. 1.5, the equilibrium concentration of CIMs should scale linearly with the concentration of neutral inverse micelles present in the suspension. This fact has been verified for a number of surfactant systems such as AOT, OLOA 1200/11K and Span 85 [11,12,19,23,58]. An example verifying the mechanism is shown in Fig.1.7 in which the concentration of CIMs in the solution is proportional to the weight fraction of surfactant present in the solution.

The electrostatic energy of a CIM of radius r in the bulk is: $k_B T \lambda_B / 2r$ (assuming $z = z_1 = z_2$) [12,17]. This is the energy required to separate a CIM from a pair of opposite CIMs to infinity [59]. Using Boltzmann statistics, the expression for the concentration of CIMs ($n_+ = n_- = \bar{n}$) under equilibrium conditions can be obtained [12,17,60]:

$$n_+ = n_- = \bar{n} = n_0 e^{-\left(\frac{\lambda_B}{2r}\right)} \tag{1.6}$$

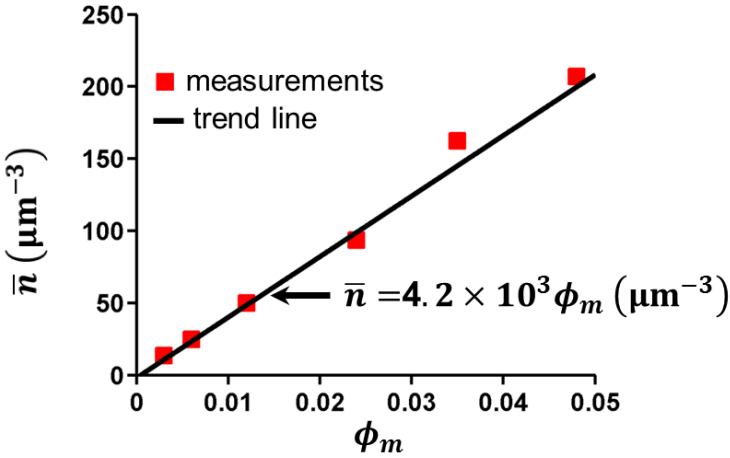

Figure 1.7: The linearly increasing concentration of charged inverse micelles with increasing weight fraction (ϕ_m) of OLOA 11K in dodecane supports the disproportionation mechanism of charging.

The fraction of charged inverse micelles can be obtained as [12,17,60]:

$$\chi = \frac{n_+ + n_-}{n_0} = 2e^{-\left(\frac{\lambda_B}{2r}\right)} \tag{1.7}$$

Eq. 1.7 can also be written in terms of an equilibrium constant as:

$$\chi = 2\sqrt{K} \tag{1.8}$$

Eq. 1.7, leads to the conclusion that the fraction of CIMs is independent of the concentration of surfactant and only depends on the Bjerrum length and the micellar core radius.

The linear increase in the conductivity of a non-polar solution with the increasing concentration of the surfactant such as AOT, PIBS, SPAN and Solsperse supports the disproportionation mechanism of charging. However, the performed studies are limited to a few surfactant systems, which are not enough to reach a solid conclusion. A further critical discussion on this topic can be found in the review by Dukhin [25].

1.5 Charging of Colloidal Particles Promoted by Surfactants

The mechanism of charging and charge stabilization in polar colloids is well understood in terms of ionization of surface groups and adsorption of potential-determining or surface-active ions [2,3,12]. This mechanism is less likely to occur in non-polar media because the desorbed protons or hydroxyls are not encapsulated/complexed by the solvent. Morrison in his landmark review [3] introduced three mechanisms by which a colloidal particle in a surfactant added non-polar dispersion could get charged. The introduced mechanisms are (1) acid base interaction (2) preferential adsorption and (3) dissociation of surface groups. Electrokinetic/adsorption measurements performed on various non-polar dispersions have provided the evidence of these mechanisms and recently surface force measurements have demonstrated the existence of long range electrostatic repulsion between colloidal particles in non-polar dispersions [7,18,19]. Here, these mechanisms are described consecutively and the evidence gathered by performing various measurements is presented.

1.5.1 Acid Base Interaction

Acid–base interactions between the particle surface and surfactant molecules which result in charged particles was proposed by Fowkes and co-workers [16]. They suggested that the charging of a colloidal particle is a three step process which begins with adsorption of neutral surfactant molecules on the surface of particles. Subsequently, a charge is transferred between the surface and the adsorbed molecules via acid–base interaction and finally the charged ions are desorbed into inverse micelles leaving behind equal and opposite charge on the surface. The polarity and magnitude of the particle charge depends on the relative acidity or basicity of the particle surface and the surfactant molecule. In the case that the particle surface is more acidic than the surfactant the surface will either donate a proton or accept an electron, resulting in a negative surface charge. In the case when the surface is more basic either an electron is donated or a proton is accepted by the surface, resulting in a positively charged particle. The degree of charge transfer between the surface and the surfactant depends on the relative difference in proton or electron pair donicity. On the basis of measurements, it is found that the mechanism is particularly relevant in the

case of nonionic surfactants, for which in the absence of an ionizable group it is difficult to determine an origin for the observation of charged surfaces [4,26].

A recent experimental verification of this mechanism was put forward by Poovarodom et al., by comparing the effect of Span and OLOA 11K on the mobility of silica particles with acidic or basic functionality dispersed in a non-polar liquid [4,61]. They found that the presence of Span 80 led to positive particle charging irrespective of the surface characteristics (acidic or basic) while the presence of OLOA 11K always resulted in negatively charged particles. This behavior was attributed to the acidic (Span) and basic (PIBS) nature of the surfactants. Furthermore, from the results they postulated that the polarity of charge is always determined by the nature of surfactant, however no convincing explanation is given for this. Similar results supporting this mechanism have been reported by Espinosa [9], Guo [57], Parent [62] and Lee et al. [4,63,64].

1.5.2 Preferential Adsorption

According to preferential adsorption, charged inverse micelles present in the bulk liquid get adsorbed asymmetrically to the particle surface resulting in a net charge on the particle surface. By measuring the force between two hydrophobized silica particles dispersed in a solution of AOT in dodecane using atomic force microscopy, McNamee et al. found that the particles become charged when the concentration of AOT is above the critical micelle concentration [65]. Taking into account the ionic nature of the surfactant and considering the fact that a proton exchange between the hydrophobic surface and the surfactant molecules is unlikely, the authors assumed that the surface charge of the particle is negative and charging is attributed to preferential adsorption of AOT anions. Convincing evidence supporting this mechanism is provided by Smith et al. [10]. They measured the electrophoretic mobility of hydrophilic and hydrophobic TiO_2 particles dispersed in a solution of AOT in toluene using differential-phase optical coherence tomography. Calculating the zeta potential from the measured values of the mobility, they found that the zeta potential is positive for the hydrophilic particle and negative for the hydrophobic [10]. On the basis of these observations they proposed that surface charge of different sign can be the result of preferential partitioning of the ionized surfactant’s cations and anions between the

particle and the core of inverse micelle in the bulk liquid, and the surface hydrophobicity plays an important role in the preferential partitioning [10,17,66]. An overview of experimental results supporting this mechanism can be found in a review by Smith et al. [20].

1.5.3 Surface Dissociation

The dissociation of a surface group and stabilization of dissociated ions by an inverse micelle has been used to explain the charging of particle surfaces in non-polar liquids. There are very few studies which explored this mechanism A further details concerning this mechanism can be found in a review by Smith et al. [20].

The charging mechanism of a colloidal particle in a surfactant added non-polar liquid is not completely clear yet, even though the majority of evidence supports acid-base mechanisms [9,26,57]. Nevertheless, systematic further studies are required to reach a solid conclusion. Further details on this topic can be found in reviews by Lyklema [2], Morrison [3], Gacek et al. [26] and Smith et al. [20].

1.6 Stabilization of Colloidal Particles

Numerous products and processes such as paints, liquid toners, and EPDs depend on colloidal stability. A colloidal dispersion is called stable if particles remain suspended in solution at equilibrium. The stability of a colloidal dispersion is affected by aggregation and sedimentation. The driving force behind such phenomena is the tendency of a colloidal dispersion to minimize the surface energy [67,68]. The stability of a colloid dispersion is governed by the balance of various attractive/repulsive forces such as van der Waals attraction, double-layer repulsion and steric or electro-steric attraction/repulsion. Generally colloids are stabilized either electrostatically or sterically. The theory that describes colloid stability electrostatically is known as Deryaguin, Landau Verwey and Overbeek or commonly DLVO theory. The DLVO theory combines van der Waals attraction and double layer repulsion and the stability/instability of the dispersions can be predicted by an energy distance plot [67,55,68]. The other theory deals with sterically stabilized colloids.

1.6.1 Electrostatic Stabilization (DLVO Theory)

The total interaction energy (G_T) between two charged particles is given by the sum of the Van der Waals (G_A) attraction and the electrostatic repulsion (G_{el}) [69,70]:

$$G_T = G_{el} + G_A \tag{1.9}$$

The total value of the interaction determines the stability of the dispersion. In the next sections, both the Van der Waals and electrostatic interactions are discussed, as well as the limits and validity of DLVO theory in the context of non-polar dispersions.

1.6.1.1 Van der Waals Attraction

For a one-component system, the force of attraction or repulsion between individual atoms or molecules at short distances is known as van der Waals forces. The molecular van der Waals force is due to three contributions: dipole–dipole (Keesom), dipole–induced dipole (Debye) and London dispersion interactions. The van der Waals attractive energy (G_A) between two identical molecules separated at a distance r_d is given by [2,68,69]:

$$G_A = -\frac{\beta_{11}}{r_d^6} \tag{1.10}$$

Here, β_{11} is a size dependent constant. In non-polar liquids the coherency is mainly determined by London–Van der Waals/dispersion forces [68].

1.6.1.2 Double-Layer Repulsion

The distribution of surface charge, counter ions and co-ions due to diffusion and electrostatic attraction/repulsion around a charged particle dispersed in a liquid is called the double layer. Using the Poisson equation with the Boltzmann distribution of *z*:*z* symmetric ions around the particle, Gouy and Chapman independently modeled the surface potential and charge distribution around the particle [1,68,69]. Stern modified the Gouy and Chapman model by introducing a first layer of counter ions next to the surface and taking into account the finite size of ions. The potential at the surface Ψ_0 decreases linearly to a value Ψ_s and then exponentially with

distance x. It becomes zero in the bulk solution, see Fig. 1.8. The potential at the slipping plane is also called the zeta potential ζ, which is measured

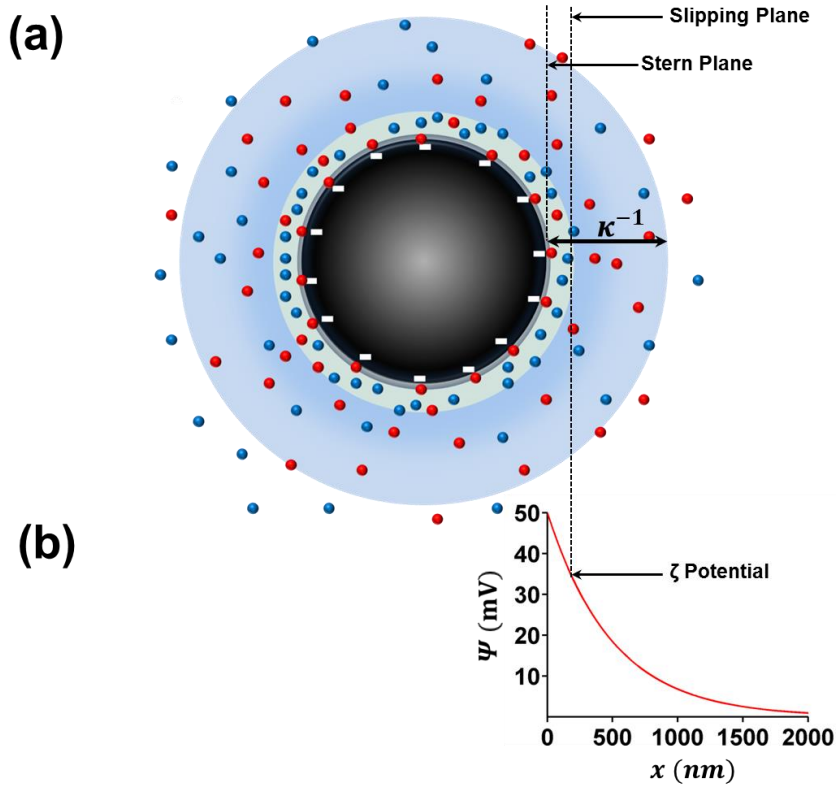

Figure 1.8: (a) Illustration of the Stern plane and electrical double layers around a negatively charged particle (black sphere) suspended in a liquid containing z:z ions. The postive ions are depicted as blue color spheres while the negative are depicted as red color spheres. In (b) the change in potential with distance *x* is shown.

electrokinetically. The thickness of the double layer depends on the concentration and the valency of ions and is given by the reciprocal of the Debye-Hückel parameter κ [1,2,68]:

$$\kappa^{-1} = \left(\frac{\varepsilon_0 \varepsilon_r k_B T}{2\bar{n} z^2 e^2}\right)^{1/2} \tag{1.11}$$

According to the DLVO theory, particles repel each other when the distance between them is so small that their electrical double layers begin to interpenetrate. The repulsive force is equal to the gradient in the overlap

potential. In a liquid with low ion concentration, the electrostatic energy of the interaction between two spheres of radius *r* is given by [2]:

$$G_{el} = \frac{\varepsilon_0 \varepsilon_r \zeta^2 r^2}{R} \, e^{-\kappa(R-2r)} \tag{1.12}$$

R is the distance between the centers of the particles. From Eq. 1.12, it is clear that G_{el} decays exponentially with increasing *R* and approaches zero at large *R*. The rate of decrease of G_{el} also depends on the value of κ^{-1}: larger the value of κ^{-1} slower the decay.

In the case of non-polar dispersions often the estimated values of the ionic strength are so small that the DLVO theory reduces to simple coulombic repulsion due to electrical double layer overlap. Also, when the concentration of particles in the dispersion is very large then the electrostatic repulsive force becomes insufficient to stabilize the particle because of (1) a long electrical double layer due to the low ionic strength (2) a slow variation of electric potential with distance from the particle surface (3) the net potential due to double layer overlap varies slowly with distance. All these effects result in a weak repulsive force between the particles [3]. Particles can be stabilized in a non-polar dispersion electrostatically when the weight fraction of particles ϕ_m is very low ($\phi_m < 0.01$) and the stability of such a dispersion can be explained on the basis of the DLVO theory. In various applications of non-polar dispersions, for which $\phi_m$of particles is usually very high ($\phi_m > 0.1$), another stabilization technique, known as steric stabilization, is employed.

1.6.2 Steric Stabilization

Steric stabilization is a mechanism that explains the ability of polymer/ surfactant additives to prevent coagulation of colloidal dispersions. It is believed that the additives cover the colloidal particle in such a way that the long tail extends into the bulk solution, as shown in Fig. 1.9. A sterically stabilized dispersion has many advantages over an electrostatically stabilized dispersion: a large concentration of particles can be stabilized, it is insensitive to electrolyte/surfactant concentration and it is suitable for multiphase systems. Further detail on this topic can be found in leading text books on colloidal science [55,68,71].

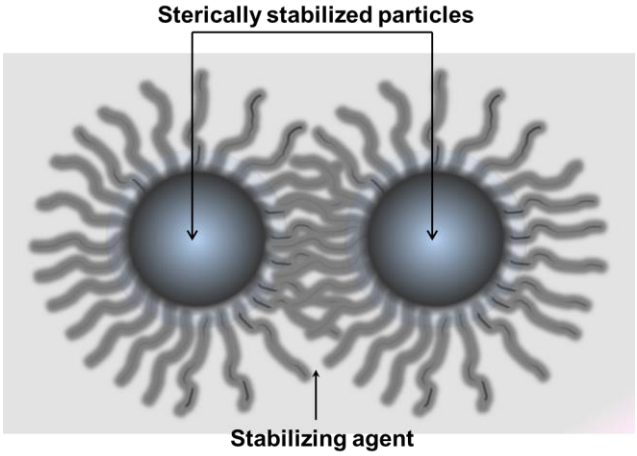

Figure 1.9: Schematic illustration of two sterically stabilized particles.

1.7 Scope and Overview of This Work

1.7.1 Scope

Non-polar dispersions with added surfactants have been investigated thoroughly during the past decades using electrical [11,12,23] and optical [10,12,17] techniques and force microscopy [19]. These investigations have led to the conclusion that due to the presence of a surfactant, inverse micelles (IMs) are formed in the dispersion of which a small fraction is charged [3,12,17]. The presence of IMs/charged inverse micelles (CIMs) plays an important role in charging and particle stabilization [17,19–21].

In general, two types of studies have been carried out to understand the role of CIMs/IMs in the charging and stabilization of colloidal particles [6,27]. In the first type of studies, the charging mechanism of IMs and the electrodynamics of CIMs are studied without the presence of the colloidal particles [13,23,72,73]. While in the second type of studies, the IMs/CIMs promoted bulk charging mechanisms of the colloidal particles have been investigated [9,20,26,64]. In the following, firstly, our current understanding about non-polar colloidal system is discussed and the issues which need further consideration are pointed out. Subsequently, the scope of this work is discussed.

In the first types of studies, the charging mechanism of IMs in the surfactant systems such as AOT, OLOA 1200/11K and Span 80 have been investigated and it has been found that the charging is due to a disproportionation mechanism. Since the investigations are limited to a few surfactant systems, no solid conclusion is drawn and the mechanism of charging is still a subject of debate [25]. On the basis of transient electrodynamical behavior of CIMs, the surfactant systems have been categorized in two broad categories [74]. The first category includes the surfactant systems which have a low generation rate of new CIMs and when a voltage larger than 1 V is applied all the CIMs present in the bulk are transported to the opposite polarity electrodes where they end up in the double layer [6]. Subsequently, the concentration of CIMs becomes very low in the bulk. The surfactant systems such as OLOA 11K, Solsperse and Span 80 with $r > 3$nm correspond to this category [75]. The second category corresponds to the surfactant systems in which the generation rate of new CIMs is very high and the bulk never depletes of CIMs. The CIMs of this category surfactant system form interfacial layers at the electrodes [76] and the electrical behavior have been modeled as a resistor in series with interface capacitances [13]. The surfactant systems such as AOT and Span 85 with $r < 3$nm correspond to this category. The difference in the interfacial behavior of CIMs has been attributed to the size of CIMs [75].

The electrodynamical behavior of the CIMs present in equilibrium in the first category surfactant have been understood on the basis of drift and diffusion and various electrodynamical regimes have been identified [72,73]. However, when the voltage is reversed after a polarizing voltage step of a few hundred seconds an additional peak is observed in the current which is not understood on the basis of the model [23,77]. The occurrence of this peak is a long standing problem and understanding the origin of this peak may shed light on the charging mechanism in non-polar liquids. In the first part of this dissertation (Chapter 2 to 6), the studies are performed to investigate the origin of the second peak in the current.

In the second types of studies the bulk charging mechanisms of colloidal particles have been investigated by varying surfactants [9,26,53], the head group of a surfactant [64,78], surface hydrophilicity/hydrophobicity of the particles [10]. On the basis of these investigations, three bulk charging mechanisms of the particles have been identified [3]: acid base

interactions [9,11,4,26], preferential adsorption [10,17] and surface dissociation [20]. However, the precise mechanism that leads to the particles charging is not clear yet [2,26].

For the applications such as EPDs and liquid toner printing, in which the charged pigment particles switch from one interface to interface,a better insight about the effect of the interfaces on the charge of pigment particles is also essential. In the second part of this dissertation (chapter 7), the performed studies on the charge of the pigment particles due to surface electrode interactions are presented.

1.7.2 Overview

Two types of studies are carried out. In the first type of studies (chapter 2 to 6), transient current measurements are used to investigate the electrodynamics and the interfacial behavior of CIMs in a non-polar liquid without colloidal particles. In chapter 2, the transient current measurement method, the interpretation of the measurements, the estimation of various parameters from the measurement and a theoretical model based on the Poisson-Nernst-Planck (PNP) equations with generation/recombination of CIMs are discussed. In chapter 3, the release of initially present CIMs from the interfaces is studied as a function of the charge content of the device and the applied polarizing/reversal voltages. Also, various electrodynamic regimes are explored.

Chapter 4 presents a study on newly generated CIMs in the presence of an applied polarizing voltage step. By increasing the voltage stepwise to a voltage of the same polarity, the mobility and the size of the newly generated CIMs is extracted. In addition to this, the bulk disproportionation mechanism for the generation of CIMs is verified. In chapter 5, the interfacial behavior of the generated CIMs, their release mechanism and their physical properties are investigated by performing various types of measurements. From these studies, it is concluded that three types of new CIMs are generated in the presence of an electric field, which are physically different from the initially present CIMs. Based on the findings of chapter 5, in chapter 6 a model is presented to explain the release of newly generated CIMs with analytical formulas. The results of the model are compared with the performed experiments.

The second type of study (chapter 7) investigates the electrodynamics of charged colloidal particles electrically and optically. The combined switching characteristics and interfacial behavior of charged colloidal particles and CIMs are investigated by varying the magnitude of the applied triangular wave voltage.

In the concluding chapter 8 an overview of the obtained results is provided. In addition to this, various aspects of the interfacial behavior of charge carriers that are not clear yet are also highlighted. The studies presented in this dissertation shed light on the electrokinetics of charged particles and CIMs when they are at the vicinity of electrodes. These studies provide a better and deeper understanding about non-polar dispersions.

Chapter 2

Transient Current Measurements

The detailed electrical characterization of non-polar liquids with added surfactant requires a fast, accurate and long-term measurement technique in combination with analysis based on a theoretical model. The aim of this chapter is to provide the necessary experimental and theoretical background for the following chapters. The first part of this chapter provides details about the specific non-polar surfactant systems, measurement devices and the measurement setup used in this work. In the second part, the relevant theory of electrodynamics of charge carriers in non-polar liquids with added surfactant is discussed, specifically in response to a polarizing voltage step.

2.1 Introduction

Because of their low dielectric constant, free charges practically do not exist in non-polar colloids, resulting in very low electrical conductivities. However, the addition of a surfactant to non-polar colloids often results in surprisingly large charge induced effects such as increased electrical conductivity and particle stabilization [3]. Due to the presence of surfactant in non-polar media, inverse micelles are formed of which a small fraction is charged, ranging from 10^{-5} to 0.1 at room temperature depending on the size of the inverse micelles [12,17,77]. These charged inverse micelles play an important role in charging and charge stabilization in non-polar colloids [6,12,17,19,20]. Surfactant mediated charging, particle charge stabilization and charge transport in non-polar colloids are used in many applications, the most well-known being electrophoretic displays [14,39]. However, little is known about the nature of the involved charges, the

precise charge stabilization mechanism, charge dynamics and the behavior of charges at the interfaces in non-polar colloids [2,25,43].

In general three types of techniques are used to characterize non-polar dispersions: electrical [6,49,52,79,80], optical [10,19,26,81,82] and small angle neutron scattering [62]. The main advantages of the electrical measurement techniques over the others are that they are fast, accurate and easy to perform. The low generation rate and the small fraction of CIMs in non-polar dispersions demand a very sensitive, fast, precise and long-duration measurement technique, because the currents decrease quickly and can be very low. Transient current measurements in response to a voltage step are an electrical technique to characterize non-polar surfactant systems, which fulfils the desired criteria. Therefore, in the first part of this dissertation, the transient current measurement technique is employed to study the electrodynamics of CIMs and their interfacial behavior without the presence of colloidal particles. In the second part of the dissertation, specifically in chapter 7, the electrodynamics and interfacial behavior of CIMs with/without colloidal particles are studied using a setup based on a high field toner cell (HFTC) and optical measurements that will be described in detail in chapter 7. There is no fundamental difference between the HFTC and transient current measurement techniques, except for the instruments used and the geometry of the measurement device. In this chapter, firstly details about the non-polar liquids and surfactants used during the course of this study are provided. Then, details of the transient current measurement setup, the interpretation of the currents, and how various parameters are extracted from the measured currents are discussed. Finally, a theoretical model based on the Poisson-Nernst-Planck equations is presented to interpret the measured currents.

2.2 Materials

Different non-polar surfactant systems have been used by the research community to explore surfactant mediated charging and charge induced effects in non-polar colloids. The most common and widely explored surfactant systems are ionic Aerosol OT or AOT and non-ionic

polyisobutylene succinimide (PIBS or OLOA) and sorbitan trioleate (Sorb or Span) in dodecane, hexane or other non-polar liquids. Two types of experiments were performed in this dissertation. In a first experiment, the isolated effect of the addition of surfactant in a non-polar liquid is studied using transient current measurements while in a second study non-polar surfactant systems containing particles are studied using the HFTC and optical measurements. In the next sections, details about the chemical structure and physical properties of the used non-polar liquids, surfactants and colloidal dispersions are provided.

2.2.1 Non-Polar Liquids

In Chapters 3 to 6, the electrodynamics and interfacial behavior of charge carriers are studied in dodecane, which is an alkane with twelve carbon atoms that exists in 355 different isomeric forms. In this study, n-dodecane (Sigma Aldrich with 99.9 % purity) is used, in which all carbon atoms are arranged in a single chain, as shown in Fig. 2.1 (a). Some physical properties of dodecane are: relative dielectric constant ε_r = 2, resistivity 10^{13} Ωm, dynamic viscosity η = 1.34 mPa. s and density 750 kgm^{-3}. In chapter 7, the electrodynamics and interfacial properties of charge carriers in the non-polar liquid lytol (supplied by Xeikon) are studied. Lytol is a mixture of vegetable oils and is used as a carrier liquid in liquid toner printing. In terms of physical properties, lytol is very similar to dodecane except for its dynamic viscosity, which is 5.5 mPa. s.

2.2.2 Surfactants

In Chapters 2 to 6, studies on the surfactant system OLOA 11K (Chevron) in dodecane are presented OLOA 11K is a very common and widely studied surfactant system [4,14,15,16,62,80] because of its excellent charging/stabilization properties [4,14,16,28,62,83]. It has been widely used in various applications, such as in the petroleum industry, in motor oil and in electrophoretic displays [14,28,62]. The described structure of OLOA 11K in the literature [20,62,84] is shown in Fig. 2.1 (b). However, the exact chemical structure is not revealed by Chevron and the company sells it as a mixture with mineral oil [4,15,20]. The surfactant OLOA 11K behaves similar to other variants of PIBS such as OLOA 1200 with an average molecular mass of around 950 g/mol, which is not sold any longer [84]. The

surfactant molecules of OLOA 11K have three principle parts: a non-polar polyisobutylene tail and a polar amine group head, which are connected by a succinimide functional group. The polar head features an approximate length of 1 nm and the nonpolar tail is about 4 nm [4,84].

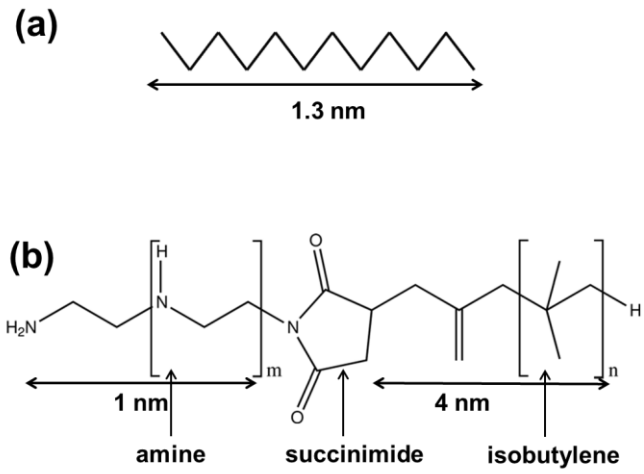

Figure 2.1: The chemical structure of (a) n-dodecane (b) OLOA 11K. The polar character of the head is a result of the amine groups. The nonpolar tail and the polar head are linked by a succinimide group.

In contrast to polar liquids, determining the critical micelle concentration in a non-polar liquid is very difficult because there is no sharp transition point [20,85]. Reported values of the CMC for OLOA 11 K in dodecane vary from 0.00005 to 0.002 weight fraction [4,23]. These differences are probably the result of different measurement techniques and different purities of the surfactant. The reported size of OLOA 11K charged inverse micelles is 10 nm [15,58,74,77]. The average number of surfactant molecules per inverse micelle has been estimated to be 500 [6].

The other studied surfactant system is Solsperse (Lubrizol hyperdispersant) in lytol with and without colloidal particles. Lubrizol sells its dispersants under the brand name “Solsperse”. The exact chemical and structural details of Solsperse are not known. Other details such as the mobility/size of

micelles that are known are discussed in chapter 7 with the measurement results.

Mixtures of OLOA 11K in dodecane or Solsperse in lytol are prepared at weight fractions (ϕ_m) ranging from 0.0001 to 0.1. These values of ϕ_m are above the critical micelle concentration. It is assumed that the addition of surfactant or particles in the liquid does not affect the physical properties of the liquid such as the dynamic viscosity and the relative dielectric constant. This assumption is valid because the used concentrations of the surfactant or particles were low ($\phi_m < 0.1$). However, as expected due to the formation of charged inverse micelles, the conductivity of the dispersions increases considerably [20].

2.3 Device Structure

The devices that are used for transient current measurements are made of two parallel glass substrates coated with indium tin oxide (ITO) with overlapping area S = 1 cm^2 as shown in Fig. 2.2. Quartz spherical balls mixed with ultraviolet curing glue (Norland NOA68) are used to hold the ITO coated glass substrates at a distance d. The thicknesses of the devices are confirmed using the interference fringes in the transmission spectra that are recorded with a spectrophotometer (PerkinElmer, Lambda 35). The ITO coated glass substrates were purchased from Delta Technologies. Devices with thicknesses of 5 to 50 μm were used for the experiments. Since the overlapping area of the electrodes S is much larger than the device thickness d, the device can be considered as a one dimensional structure in which all quantities depend only on one spatial coordinate x.

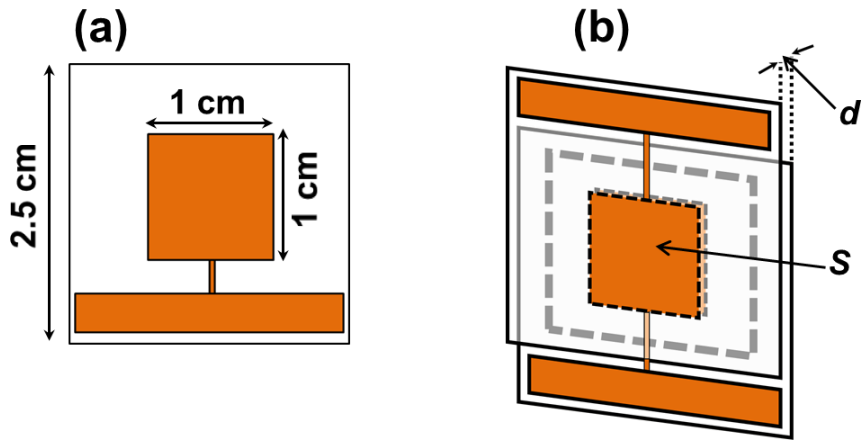

Figure 2.2: Schematic of (a) a glass substrate of thickness 1.1 mm coated on one side with a 20 nm thick layer of indium tin oxide (b) The measurement device is made by assembling the two substrates so that the electrodes overlap as indicated by *S* and the contact areas are not covered. Glass spacers mixed in UV-cured glue are used to hold the substrates together at a distance *d* from one another.

2.4 Transient Current Measurement Setup

A schematic of the transient current measurement setup is shown in Fig. 2.3. The setup can be divided into four sections. The first section of the setup is the device to be measured which is placed in a metallic box to shield it from electrical noise. The second section of the setup consists of a National Instruments USB-6212 data acquisition module (NI-DAQ). The third section is a Keithley 428 current amplifier and the fourth section is the computer controlling and synchronizing both measuring devices. With the help of the NI-DAQ device and a program written in LabVIEW, a voltage is applied across the electrodes of the device and the corresponding current is measured simultaneously with a sampling rate of 250 kS/s. Using the NI-DAQ, only a voltage in the range ± 10 V can be applied. A voltage amplifier with amplification 10X or 100X is sometimes used to extend the range of the applied voltages.

The current to be measured is supplied to the Keithley 428 current amplifier which converts the current into a voltage. The gain of the amplifier is adjustable in decade increments between 10^3-10^{11} V/A and the corresponding rise times of the device vary from 2 µs to 300 ms with increasing

amplification factor. The measured current is digitized using the NI-DAQ device.

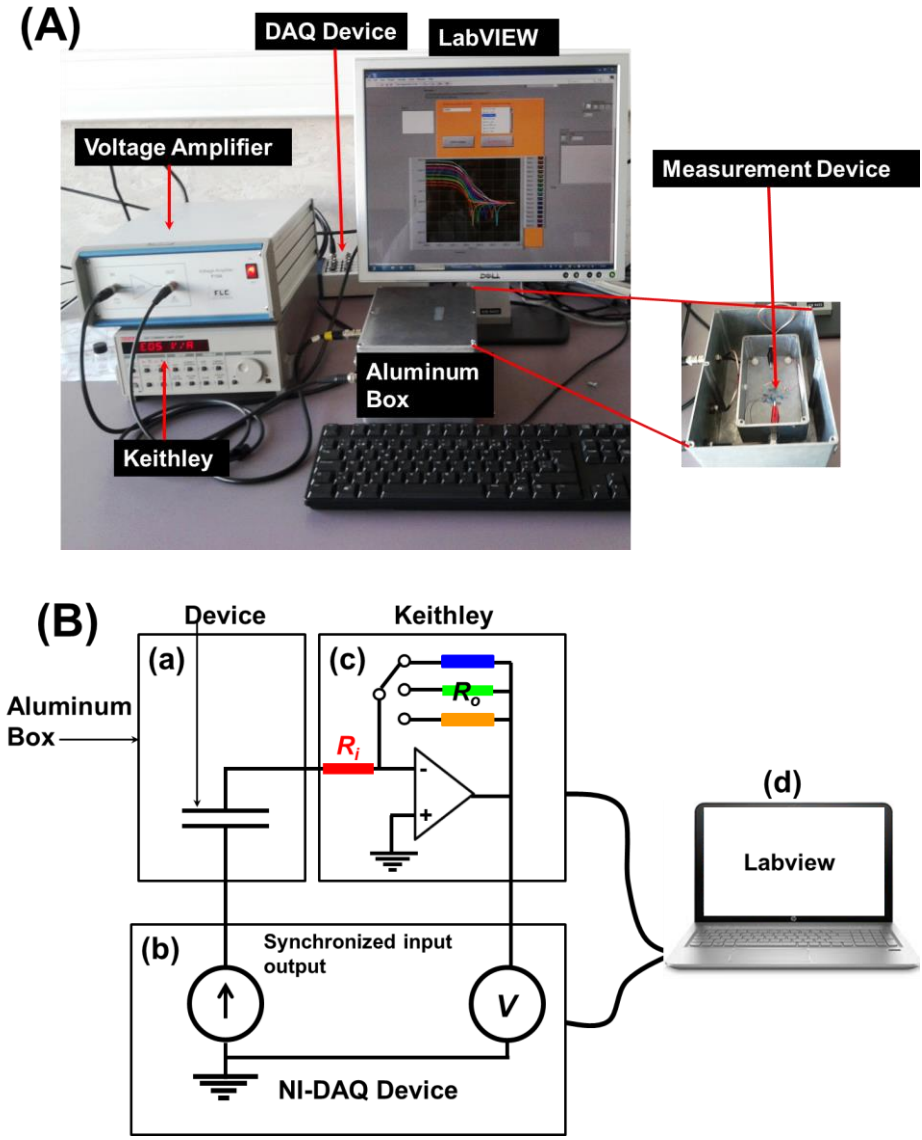

Figure 2.3: In (A) a picture of the transient current measurement setup. In (B) a schematic of the various parts of setup is shown: (a) the measurement device (b) the NI-DAQ device by which a voltage is applied across the device and the corresponding current in the external circuit is measured simultaneously (c) the Keithley 428 current amplifier (d) the input/output control section with graphical user interface.

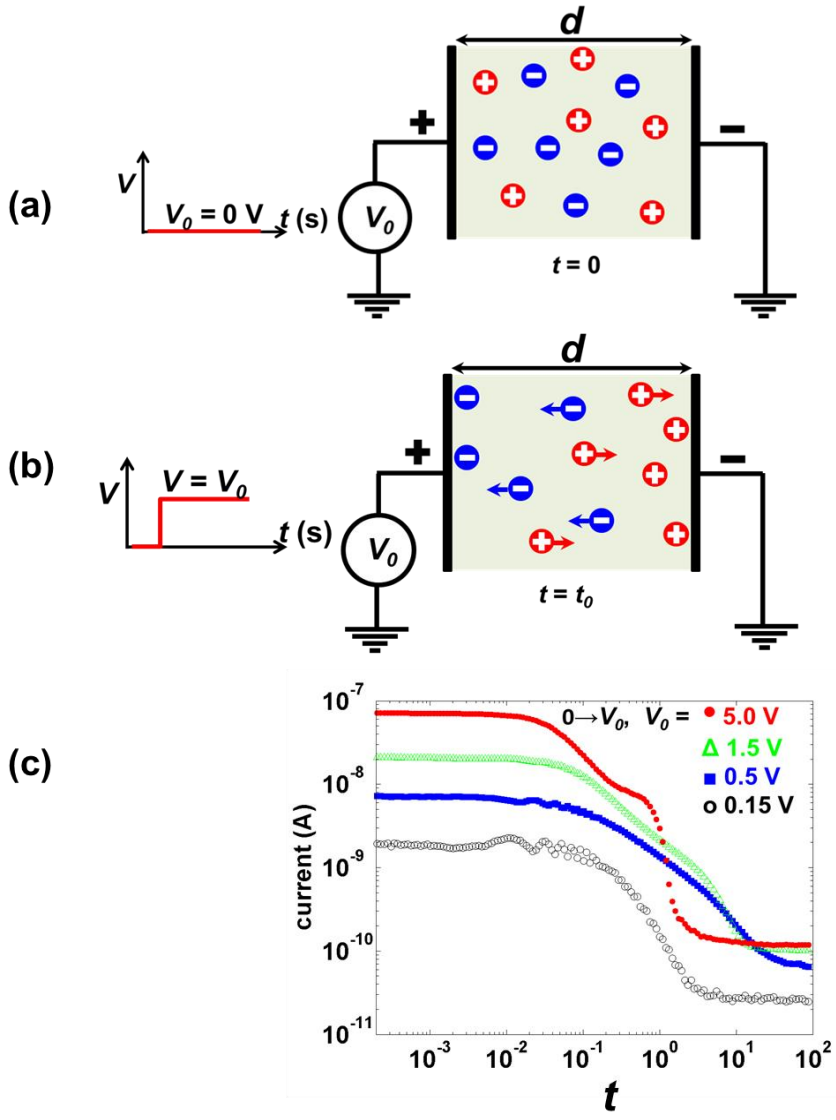

Figure 2.4: Schematic of a device filled with a mixture of surfactant in a solvent. (a) During the short circuit time, the charges are uniformly distributed in the device. (b) In response to the polarizing voltage step, charges move towards the opposite polarity electrodes resulting in a current in the external circuit. (c) Typical measured currents as a function of polarizing voltage amplitude are shown. The measured current has two phases, the initial transient phase, in which the current decreases very quickly and the quasi steady state phase in which approximately a constant current is measured.

2.4.1 The Current Measurement Procedure

Now the procedure is described which was followed in each transient current experiment in this dissertation. Firstly, the space between the electrodes of the device is filled with the prepared mixture and the electrodes are connected to the measurement setup. Before applying a voltage, the electrodes are short circuited for at least 1000 s to ensure a uniform distribution of charges throughout the device, as depicted in Fig. 2.4 (a). Afterwards, a polarizing voltage step V_0 is applied across the electrodes and the resulting polarization transient current is measured in the external circuit, as depicted in Fig. 2.4 (b). For a different polarizing voltage step V_0, the same procedure is repeated. The measured polarization currents as a function of the voltage are shown in Fig. 2.4 (c).

2.4.2 Interpretation of the Measured Currents

The measured currents in the external circuit are due to the movement of charges in response to an applied voltage and are given by Ramo's theorem [86,87]. For a device with two parallel electrodes, according to Ramo's theorem, the total charge on the electrode has two contributions, a capacitive charge and an induced charge. The first contribution is related to charging of the electrodes as a result of the applied voltage. The second contribution is due to the moving charge between the electrodes, which induces charge on the electrode and is weighed by the electric potential at that position [86,87]. Thus the total charge on the electrode for a 1D situation is: $Q_{el} = CV_0 + (S\int_0^d \rho\, x dx)/d$. Here, Q_{el} (C) is the total charge on the electrode, C = $(\varepsilon_0 \varepsilon_r S)/d$ (F) is the capacitance, V_0 is the magnitude of the applied polarizing voltage and ρ (C/m^3) is the charge density. The change in the charge at the electrode gives the current, can be calculated as: $I(t) = \frac{\partial}{\partial t}(Q_{el})$.

$$I(t) = CV_0\delta(t) + \frac{\partial}{\partial t}\left((S\int_0^d \rho\, x dx)/d\right) \tag{2.1}$$

Here $\delta(t)$ is the Dirac delta function representing the charging of the capacitor at t = 0 s. The first term of Eq. 2.1 will not be considered further in this work.

From the shape of the measured currents shown in Fig. 2.4 (c), the current can be roughly divided in two phases. In the first phase, decreasing currents are measured. These currents are due to the movement of an initially present, fixed amount of CIMs which is initially homogeneously distributed between the electrodes at t = 0 s. Once all the initially present CIMs reach the electrodes, the final phase starts during which more slowly decreasing currents are measured for a long duration as shown in Fig. 2.4 (c). These currents are called quasi steady state currents (I_g). These quasi steady state currents are due to bulk disproportionation and surface generation of new charges [6,23,76].

2.5 Drift, Diffusion, Generation and Recombination of Charged Inverse Micelles

A theoretical model based on the Poisson-Nernst-Planck (PNP) equations is presented to interpret the measured currents. In this model it is assumed that bulk disproportionation is the charge generation mechanism in surfactant added non-polar liquids above the critical micelle concentration, leading to a symmetric univalent suspension [58,88]. The assumption of univalency is valid, because in a non-polar environment at room temperature (298 K), CIMs having double or larger charge are energetically not favorable [72,73].

In thermal equilibrium and in the absence of an applied field a small fraction of IMs are charged due to the disproportionation mechanism. In chapter 1 section 1.4.2, it has already been shown that the equilibrium concentration of positive and negative CIMs is given by:

$$n_+ = n_- = \bar{n} = \sqrt{K}\,\bar{n}_0 \tag{2.2}$$

The generation of charges according to the bulk disproportionation mechanism in the presence of an applied electric field is given by:

$$\frac{\partial n_{g\pm}}{\partial t} = \beta {n_0}^2 - \alpha n_{g+} n_{g-} \tag{2.3}$$

Here, n_{g+} = n_{g-} is the concentration of newly generated positive and negative CIMs in the presence of an electric field. For Eq. 2.3, it is assumed that the CIMs that are generated in the presence of an electric field are different than the initially present CIMs, this assumption will be verified in

chapter 5. The generation of new CIMs in the presence of a field is determined by the generation rate constant β ($\approx 10^{-24}$ m^3/s [23,58]) and the reverse process in which two oppositely charged inverse micelles recombine forming two neutral micelles is determined by the recombination rate constant α ($\approx 10^{-22}$ m^3/s [23,58]). Thus, the change in the concentration of neutral micelles is given by:

$$\frac{\partial n_0}{\partial t} = -2(\beta {n_0}^2 - \alpha n_{g+} n_{g-}) \tag{2.4}$$

When a voltage is applied across the electrodes of the device, the flux of initially present positively and negatively charged inverse micelles in the *x*-direction (see Fig. 2.5) due to drift and diffusion is given by:

$$\Psi_{\pm} = \pm \mu_{\pm} n_{\pm} E - D_{\pm} \frac{\partial n_{\pm}}{\partial x} \tag{2.5}$$

Here, $\Psi_{\pm}$ is the flux ($m^{-2}s^{-1}$), $\mu_+ = \mu_-$is the mobility ($m^2V^{-1}s^{-1}$) and always takes a positive value, $n_{\pm}$ is the concentration (m-3), $D_{\pm}$ is the diffusion constant (m^2s^{-1}) of positive/ negative CIMs and *E* is the electric field (Vm^{-1}). Assuming that the size of positive, negative and neutral inverse micelles is the same $D_0 = D_+ = D_- = D$. The diffusion constant and the mobility are linked by Einstein's relation $D/\mu = k_B T/e$.

Similarly, the flux due to the newly generated CIMs in the presence of an electric field is given by:

$$\Psi_{g\pm} = \pm \mu_{g\pm} n_{g\pm} E - D_{g\pm} \frac{\partial n_{g\pm}}{\partial x} \tag{2.6}$$

Here, $\Psi_{g\pm}$ is the flux due to newly generated CIMs, $\mu_{g+} = \mu_{g-} = \mu_g$, is the mobility of the newly generated CIMs and $D_{g\pm}$ is the diffusion constant (m^2s^{-1}) of newly generated CIMs. In chapter 4, it will be shown that the mobility and the size of newly generated CIMs is the same as that of the CIMs present in equilibrium.

The change in the concentrations of charged and neutral inverse micelles due to drift, diffusion, generation and recombination is given by the continuity equations:

$$\frac{\partial n_{\pm}}{\partial t} = -\frac{\partial \Psi_{\pm}}{\partial x} \tag{2.7}$$

$$\left(\frac{\partial n_{g\pm}}{\partial t}\right) = -\left(\frac{\partial \Psi_{g\pm}}{\partial x}\right) + \beta {n_0}^2 - \alpha n_{g+} n_{g-} \tag{2.8}$$

$$\frac{\partial n_0}{\partial t} = D\frac{\partial n_0}{\partial x^2} - 2\left(\beta {n_0}^2 - \alpha n_{g+} n_{g-}\right) \tag{2.9}$$

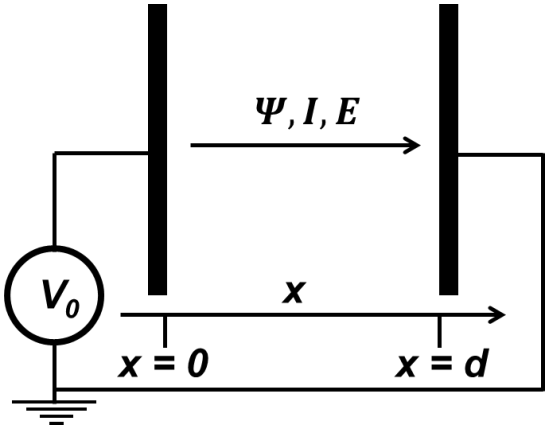

Figure 2.5: All the measurements that are shown in this dissertation are performed on devices which have an area of S = 1 cm^2 while the distance between the electrodes d varies from 4 to 50 μm from experiment to experiment. Since the size of the electrodes is much larger than the distance between them, the device can be considered to be a one-dimensional structure in which all quantities vary only along the x axis.

The change in the electric field between the electrodes due to space charge is given by the Gauss equation:

$$\frac{\partial E}{\partial x} = \frac{\rho}{\varepsilon_0 \varepsilon_r} \tag{2.10}$$

The measured currents are simulated by numerically solving Eq. 2.5-2.10, with an initial homogeneous distribution of CIMs in the device and with blocking boundary conditions so that no charge can come in or go out of the device. The resulting electric current due to drift and diffusion of charged inverse micelles in the external circuit is calculated using [58,72].

$$I(t) = \frac{eS}{d}\int_0^d (\Psi_+ - \Psi_-)dx \tag{2.11}$$

or similarly by:

$$I(t) = \varepsilon_r \varepsilon_o S \left.\frac{\partial E}{\partial t}\right|_{(0,t)} \tag{2.12}$$

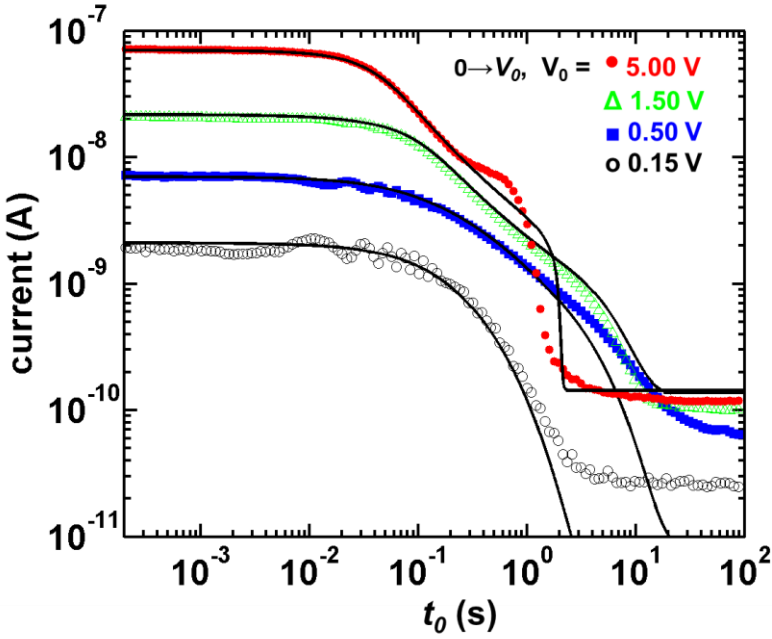

Figure 2.6: The match between measured transient polarization current measurements (colored dots) (for the device with d = 48.36 μm and filled with ϕ_m = 0.003 of OLOA 11K in dodecane) and the simulations (black lines) validating the model based on drift, diffusion with generation/recombination of charged inverse micelles. The simulation parameters are $\bar{n}$ = 10 μm^{-3} and μ = 1320 μm^2/Vs. The mismatch for the quasi steady state currents (between measurements and simulations) for low voltages is due to charge injection from the electrodes which is not included in the model. It has been reported that for low voltages, the quasi steady state current is proportional to the electric field near the electrodes [89].

A comparison between measurements and simulations is shown in Fig. 2.6. In the presented model, it is assumed that all newly generated CIMs are identical. However, in chapter 6, it will be shown that three different types of CIMs are generated in different proportions in the presence of an electric

field that behave differently at the interfaces. Therefore, the presented model is modified accordingly in chapter 6.

2.5.1 Estimation of the Mobility and the Concentration of the CIMs

The average concentration and the mobility of positive/negative CIMs that are present between the electrodes in the equilibrium situation can be calculated from measured transient currents with the assumption that the concentration of positive and negative charges is the same and that they are univalent [72,73].

The average concentration of the CIMs present in equilibrium can be estimated by integrating the measured transient current, from which the quasi steady state current or generation current (I_g) is subtracted (filled area in Fig. 2.7). The polarizing voltage duration and magnitude should be long ($t >> d^2/(\mu V_0)$) and high enough (V_0 >1 V) so the CIMs get completely separated and the concentration of charges becomes very low in the bulk. The concentration can be calculated as [23]:

$$\bar{n} = n_+ = n_- = \frac{\left(\int_0^{t_{tr}} (I - I_g)dt\right)}{edS} \tag{2.13}$$

In Eq. 2.13, t_{tr} is the time by which the current reaches quasi steady state.

Knowing $\bar{n}$, the mobility of the CIMs can be estimated from the initial current for which the field between the electrodes in the absence of space charge is V_0/d [6,90]. The mobility of CIMs is:

$$\mu = \frac{I_{(t=0\ \mathrm{s})} d}{2e\bar{n}SV_0} \tag{2.14}$$

From Eq. 2.13-2.14, rough values of the concentration and mobility are obtained. More accurate values are obtained by matching the measurements with simulations, as shown in Fig. 2.6. The obtained value of the mobility which yields a good match is 1320 $\mu m^2 V^{-1} s^{-1}$ and is found to be approximately independent of the mass fraction of OLOA 11K in dodecane and of the thickness of the device. From this value of the mobility, using Stokes equation, the hydrodynamic radius of CIMs is calculated. The

obtained value of the hydrodynamic radius is 5.5 nm, which is consistent with previously reported values [4,15,23,62,74].

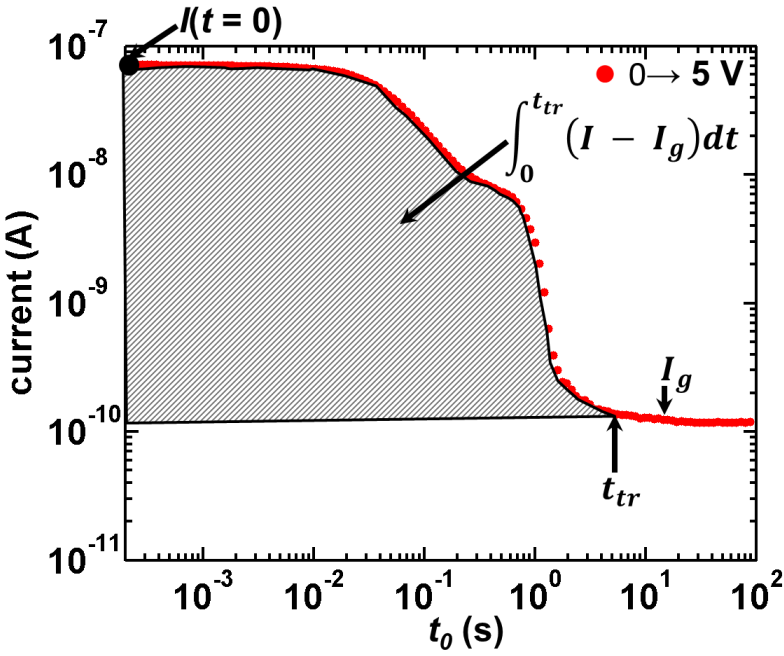

Figure 2.7: A transient current measurement for a polarizing voltage step 0→V0 (V0 = 5 V) on the device with d = 48.36 μm and filled with ϕ_m = 0.003 of OLOA 11K in dodecane. The voltage is applied at t = 0 s, when the charge distribution in the device was uniform. By integrating the current (shown by the filled pattern) and using Eq. 2.13 the value of the equilibrium concentration is obtained. The value of the mobility is obtained from the initial current using Eq. 2.14.

2.5.2 Electrodynamical Regimes

The presence and the movement of the charges affect the field in the device due to the formation of space charge in the device. The effects of the charge on the field in the device are often described by the normalized charge content of the device $\lambda = \frac{2e^2\bar{n}d^2}{\varepsilon_0\varepsilon_r k_B T}$ and the applied normalized voltage $\varphi = V_0/(k_BT/e)$ [6,72,73]. Depending on λ and φ, four electrodynamic regimes with analytical expressions which are approximate solutions of the Poisson-Nernst-Planck (PNP) equations have been identified, i.e., the geometry limited, diffusion limited, diffuse double layer limited, and space charge

limited regimes [72]. Here a brief description of the identified eletrodynamic regimes is given with analytical expressions for the transient currents in the corresponding regimes.

In the geometry limited regime, applicable for a low charge content ($\lambda < 500$) and large voltages (~V_0 > 1 V), the charges have no influence on the electric field and diffusion can be neglected, resulting in a uniform movement of charges towards the counter electrodes where they end up in double layers. The uniform movement of charges results in a linearly decreasing current: $I(t) = \frac{2\bar{n}e\mu V_0 S}{d}\left(1 - \frac{t}{t_{tr}}\right)$, until the transit time $t_{tr} = \frac{d^2}{\mu V_0}$. The diffusion limited regime is valid for a low charge content and low voltages. In this regime, charges have negligible influence on the field and diffusion prevents them from separating. Thus, the distribution of charges in the device remains approximately in a homogeneous state at all times and the current decreases exponentially as: $I(t) = \frac{16\bar{n}e\mu VS}{d\pi^2} e^{-(\pi^2 D/d^2 t)}$. In the space charge limited regime, applicable for a large charge content (λ > 5000) and large applied voltages (V_0 > 1 V), transient space charge layers are formed which screen the field in the bulk, resulting in a power law decay of the transient current $I(t) = I_c t^{-3/4}$, with I_c a constant which depends on λ, φ and t_{tr}. In the steady-state all initially present charges do get separated and end up in thin double layers at the electrodes [15,91], while there is a high field in the bulk. In the double layer limited regime, valid for large charge contents and low applied voltages, the field is screened at a characteristic time $\tau_{DL} = \lambda_{DL} d/2D$ (with $\lambda_{DL} = \sqrt{(\varepsilon_0 \varepsilon_r k_B T/2e^2\bar{n})}$ the Debye length) and becomes zero in the bulk, resulting in an incomplete charge separation. The resulting current can be modeled as: $I(t) = \frac{2\bar{n}e\mu V_0 S}{d} e^{-t/\tau_{DL}}$.The steady-state consists of thin, double layers at the electrodes over which the field drops, and a bulk region with charge concentrations close to the equilibrium concentration [72].

2.6 Conclusions

Transient current measurements in response to a voltage step provide details of the electrical behavior, of properties such as the concentration and mobility of charge carriers and of the generation mechanism in surfactant added non-polar systems. The measured transient currents are dominated by drift, diffusion and generation/recombination of charged inverse micelles. The polarization currents have been investigated in detail and the electrical behavior of the initially present CIMs has been understood well on the basis of the drift, diffusion model in combination with surface adsorption. For the case of the surfactant systems such as OLOA 11K in dodecane, various electrodynamic regimes have been identified. However, there is no reported study about the interfacial behavior, the release of CIMs from interfaces and the electrodynamics of CIMs in the presence of colloidal particles. In the following chapters, this gap is filled by performing various measurements. In general, to study the interfacial behavior, release mechanism and electrodynamics, firstly a polarizing voltage step is applied and then the voltage is reversed or switched off abruptly and the corresponding currents are measured. The measured currents are interpreted by drift and diffusion of the CIMs/particles (PNP model), together with space charge limited release of the newly generated CIMs and charging of the particles at the electrodes.

Chapter 3

Transport of Charged Inverse Micelles for the Reversal Voltages

The electrodynamics of charges in non-polar liquids in response to a polarizing or relaxation voltage are understood well and the measured currents can be modeled using the Poisson-Nernst-Planck equations with appropriate boundary conditions and generation/recombination of the charges. Understanding the electrodynamics of charges in response to a reverse voltage step applied after a polarizing voltage is also relevant for displays and other applications. The present study of reversal currents provides important details about the behavior of charges at the interfaces and their adsorption/desorption properties.

3.1 Introduction

A surfactant is added in a non-polar dispersion in order to charge and stabilize the particles in the dispersion [12,17,20,26]. However, not all added surfactant ends up on the particles or other interfaces: an excess remains free in the dispersion in the form of charged and neutral inverse micelles. The presence of free charged inverse micelles (CIMs) in the dispersion results in an increase of the conductivity of the dispersion. Controlling the trajectories

of the particles in highly conductive media is challenging because of screening of the electric field and electro-hydrodynamic flow [92–94]. This causes particle clustering and pattern formation at the electrodes [93,95,96]. Such effects in EPDs result in image degradation, increased power consumption and a reduced life span of electrophoretic devices [14]. Therefore, understanding the electrokinetics in such conductive dispersions is relevant. Many properties of the dispersion can be studied without the presence of colloidal particles. The electrical behavior of non-polar dispersions with added surfactant is governed by drift, diffusion, bulk/surface generation, recombination and adsorption/desorption of CIMs.

Transient current measurements in response to a polarizing voltage step ($0 \rightarrow V_0$) have provided a deep insight about the dynamics and the generation mechanism of CIMs [58,72]. For surfactant systems such as OLOA 11K, Solsperse and Span 80, in which the generation rate is so low that the bulk can be almost depleted of charges, depending on the magnitude of the applied voltage and the charge content of the device various electrodynamical regimes with analytical formulas have been identified [72,73]. When analyzing the steady-state currents, information is obtained on the generation of new CIMs in the bulk [23,73,97]. When the polarizing voltage is increased stepwise to a voltage of the same polarity, even more detailed information about the properties of these newly generated charged inverse micelles is obtained [58]. Similarly, the relaxation currents when the voltage is switched back to zero ($V_0 \rightarrow 0$) are useful to examine the diffusion properties of CIMs [79]. However, transient reversal currents that occur when the voltage is switched to a voltage of opposite polarity are rarely studied and the observed non-monotonic behavior of the transient currents is poorly understood.

This chapter presents a detailed study of the transport characteristics of CIMs in response to a reverse voltage applied abruptly after either a small or a large polarizing voltage, and explore the various electrodynamic regimes for the reversal voltages by varying the normalized charge content of the device and the magnitude of the applied reverse voltage. Transient current measurements are carried out for thin layers of suspensions containing OLOA 11K surfactant in dodecane and the shape of the transient reversal currents is compared with simulation results based on the Poisson-Nernst-Planck equations.

3.2 Experimental Methods

3.2.1 Transient Currents Measurements

The same type of device is used for transient current measurements that has been described in chapter 2. The space between the electrodes of the device is filled with a mixture of high-purity dodecane and the surfactant OLOA 11K. Before each measurement, the electrodes are short-circuited for a duration of 1000 s to ensure homogeneous initial conditions. Then, a polarizing voltage step V_0 is applied ($0 \rightarrow V_0$) across the electrodes that results in the movement of CIMs from the bulk towards the opposite polarity electrodes, as illustrated in Fig. 3.1 (a), and the transient polarization currents are measured. At a particular time $t_0 >> d^2/(\mu V_0)$, the voltage is switched to the voltage of opposite polarity ($V_0 \rightarrow -V_1$) and the corresponding transient reversal currents are measured. The reversal currents are due to the transport of CIMs from one electrode to the other, as depicted in Fig. 3.1 (b).

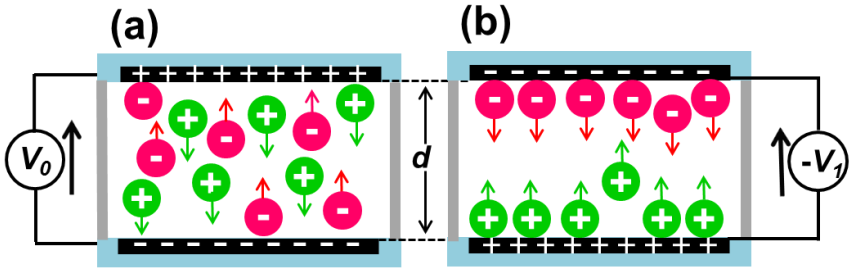

Figure 3.1: Schematic representation of a measurement device with two parallel electrodes separated at a distance d with overlapping area S = 1 cm^2. In (a), starting from the homogeneous equilibrium situation, a voltage step V_0 is applied and the CIMs travel towards the electrodes of opposite polarity resulting in a current in the external circuit. Eventually they end up in the diffuse double layers at the electrodes. In (b) the voltage is reversed to V_1 and the transient reversal current is measured.

3.2.2 Transient Particle Trajectories

To visualize electro-hydrodynamic (EHD) flow in the liquid, tracer particles are tracked optically using a setup consisting of a CCD camera (Pulnix TM-6740L) mounted on an optical microscope with a 40 times objective as shown in Fig. 3.2. A colloidal dispersion is prepared with poly (methyl methacrylate) (PMMA) particles with radius 1.0 μm at a mass fraction ϕ_m below 0.0001 in a solution containing a mass fraction ϕ_m= 0.003 of OLOA 11K in dodecane. The used PMMA particles have poly-12 hydroxystearic acid (PHSA) brushes grafted on their surface for steric stabilization. Using optical tracking electrophoresis as described elsewhere [88], it is found that the mobility of the PMMA particles is in the order of 100 $\mu m^2V^{-1}s^{-1}$.

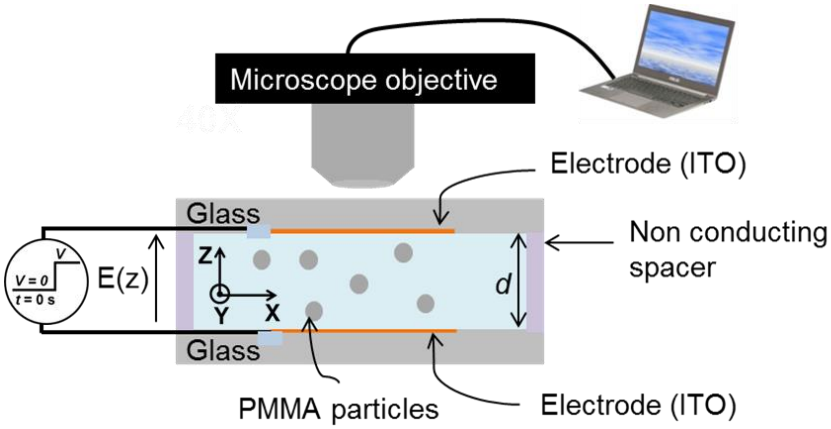

Figure 3.2: Schematic of the particle tracking setup. The particles are tracked in the x-y plane. In the absence of EHD flow, the particle motion will be along the z axis and no significant change in the x-y position of the particle is expected while in the presence of EHD flow the motion of the particle will be multidimensional.

A similar device as described previously (see Fig.3.2) is used, with d = 50 μm, and the transient experiment is repeated. First a polarizing voltage ($0 \rightarrow V_0$) is applied for a long duration ($t_0 >> d^2/(\mu V_0)$) to ensure that all tracer particles and CIMs are transported towards the electrode with opposite polarity. Then a reverse voltage step is applied ($V_0 \rightarrow -V_1$) for a duration of 30 s. The particle trajectories are obtained by standard image analysis [98]. Only the particle motion in the *xy*-plane, perpendicular to the optical axis is

obtained, which is sufficient to detect EHD flow. In the absence of EHD flow particles travel mainly along the *z*-axis, showing only Brownian motion in the *xy*-plane. In the presence of EHD flow, particles can follow complex trajectories in the *xy*-plane before reaching the electrode.

3.3 Results and Discussion

Depending on the charge content of the device and the applied voltage, four electrodynamic regimes with analytical solutions have been identified for the polarizing voltages [6,73]. These regimes are discussed below in the context of transient reversal currents. The transient reversal current measurements and the simulations for device 1 with a small charge content and device 2 with a large charge content are shown in Fig. 3.3 and Figs. 3.4-3.5 respectively. For the transient current simulations, the same model which has been described in chapter 2 is used. Here, for simplicity the generation/recombination of new charges in the bulk or at the interfaces is not included.

From the described model, just after reversing the voltage $V_0 \rightarrow -V_1$ the current can be estimated as follows. Just before reversing the polarity of the voltage the CIMs are in the diffuse double layers and the system is in a steady state during which the fluxes are zero everywhere. Immediately after the voltage is reversed, the CIM concentrations at t = 0 s remain the same, but the field is decreased by a term $(V_0 + V_1)/d$ everywhere in the bulk. From the flux Eq. 2.5 it can be seen that the flux at t = 0 s only has a contribution from the change in field: $\Psi_{\pm} = \mp \mu n_{\pm} (V_0 + V_1)/d$, which yields the current after integration over the device thickness:

$$I_{(V_0 \rightarrow -V_1, t=0)} = -\frac{2\mu e \bar{n} S (V_0 + V_1)}{d} \tag{3.1}$$

In the following, the results for different charge contents and different magnitudes of both the polarizing and the reverse voltage are presented.

3.3.1 Low Charge Content: Geometry and Diffusion Limited Currents

The measurements and simulations of transient reversal currents for device 1 with $\bar{n}$ = 1 µm^{-3} and d = 4 µm, resulting in $\lambda \approx 13$ are shown in Fig. 3.3. The used values of simulations parameters for Fig. 3.3 are: $\bar{n}$ = 1 µm^{-3} and μ = 1320 µm^{2}V^{-1}s^{-1} .Since the value of λ is very low, the presence of charge does

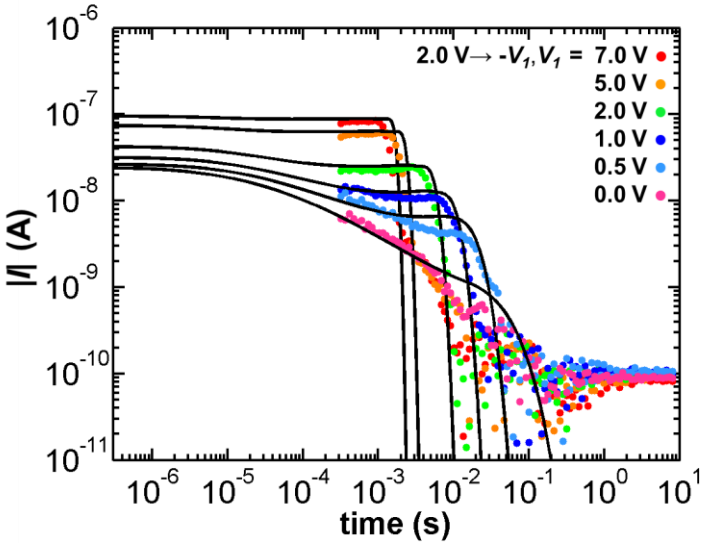

Figure 3.3: The measured reverse currents (colored dots) are compared with the simulated reverse currents (black lines) for device 1 (ϕ_m=0.0003 OLOA 11K, d = 4.0 µm, S = 1 cm^2 and λ =13) for 2 V→ -V_1, with V_1 = 0, 0.5, 1, 2, 5 and 7 V. For $V_1 \geq$1 V, after a short initial phase the currents are approximately constant until the transit time, after which they rapidly decrease and become very small.

not influence the field in the device and depending on the magnitude of the applied reversal voltage the current can be diffusion or geometry limited. Fig. 3.3 shows the transient reversal current when the applied voltage is reversed from a steady state situation at $V_0 = 2$ V to -V_1 with V_1 = 0, 0.5, 1, 2, 5 or 7 V. At t = 0 s, all CIMs are located close to the electrodes forming a double layer and the current is given by Eq. 3.1. After the CIMs have moved away from the electrodes, the contribution of the diffusion term decreases (for V_1 > 1 V) because of a large field $E = V_1/d$ in the bulk. An approximately constant current $I = -2\mu e\bar{n}SV_1/d$ is observed until the transit time $t_{tr} = d^2/(\mu V_1)$ [72]. The latter behavior corresponds to the

geometry limited regime, in which the current is not influenced by space-charge effects on the electric field related to the presence of CIMs [72,73]. For the case when V_0 >1 V & V_1 < 1 V , due to the weak field the CIMs diffuse from the double layer into the bulk, and the resulting currents decrease as $I(t)\ \alpha \frac{1}{\sqrt{t}}$. Such behavior of CIMs corresponds to the diffusion limited regime [99].

When the applied polarizing voltage V_0<< 1 V, the concentration of charges in the bulk approximately remains equal to that of the equilibrium concentration. Then, for small reverse voltages (V_1 << 1 V) exponentially decreasing currents correspond to the diffusion limited regime while for the voltage V_1 >>1 V linearly decreasing currents as: $I(t) \approx \frac{2\mu e\bar{n}SV_1}{d}(1 - \frac{t}{t_{tr}})$ correspond to the geometry limited regime (Not shown) [72,73]. Thus, for a device with low charge content, depending on the magnitude of the polarizing and reversal voltage four electrodynamic regimes can be identified.

3.3.2 High Charge Content: Space Charge and Diffuse Double Layer Limited Currents

Now let us consider the case of device 2 with high charge concentration: $n_{\pm}$= 10 μm^{-3}, d = 48.4 μm resulting in λ ≈17000. For a large value of λ, depending on the magnitude of the polarizing and the reverse voltage step, the current could be either diffuse double layer limited or space charge limited. For this case, the used values of the concentration and the mobility of CIMs for which the simulations match with the measurements are: 10 μm^{-3} and 1320 μm^{2}V^{-1}s^{-1} respectively.

3.3.2.1 Small Polarizing Voltage (V_0 < 1 V)

Let us first consider the case of transient reversal currents after a small polarizing voltage (V_0 << 1 V) is applied to device 2, shown in Fig. 3.4. In the initial state the field is screened in the bulk and there is a diffuse double layer near the electrodes. When a small reverse voltage is applied (V_1 << 1 V), the current can be modeled analytically by an exponential decrease $I(t) = -(2\mu e\bar{n}S(V_0+V_1)/d)e^{-t/\tau_{DL}}$, with $\tau_{DL} = \frac{\lambda_{DL}d}{2D}$ the time constant by which the diffuse double layer is formed and $\lambda_{DL} = \sqrt{(\varepsilon_0\varepsilon_r k_B T/2e^2\bar{n})}$ the

Debye length [72,91]. For a large reverse voltage step (V_1 > 1 V), the transient reversal currents are similar to the polarization currents (V_0 > 1 V), because the initial condition is similar to the equilibrium condition in which the concentration of CIMs remains homogeneous. The good match between measurements and simulations indicates that the behavior of the CIMs is in accordance with the drift and diffusion model.

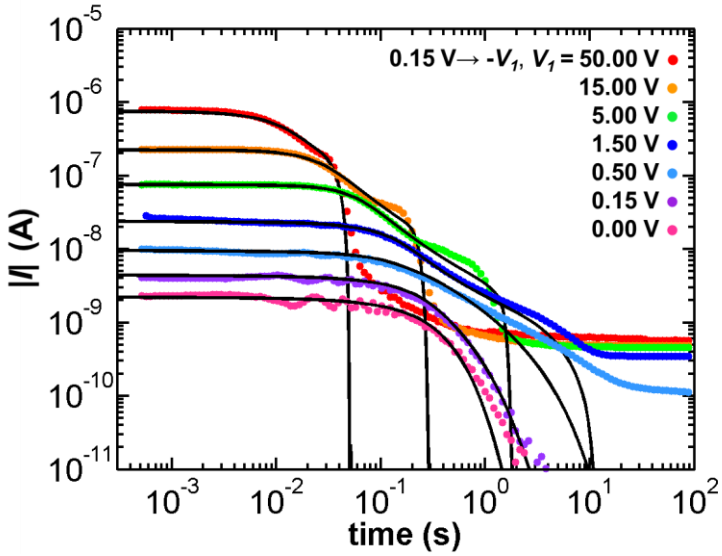

Figure 3.4: Measured (colored dots) and simulated (black lines) transient reversal currents for device 2 (ϕ_m = 0.003 of OLOA 11K in dodecane, d = 48.4 μm and S = 1 cm^2 and λ =17000) for 0.15 V→-V_1, with V_1 = 0, 0.15, 0.5, 1.5, 5, 15 and 50 V. The match between the measurements and the simulation validates the model. The simulation parameters are $\bar{n}$ = 10 μm^{-3} and μ = 1320 μm^2/Vs.

3.3.2.2 Large Polarizing Voltage (V_0 > 1 V)

When the applied polarizing voltage is large, all the CIMs present in the bulk liquid travel towards the opposite polarity electrode where they end up in thin double layers [58]. The transient reversal currents after the steady state at V_0 = 15 V are measured for V_1 = 0, 0.15, 0.5, 1.5, 5, 15 and 50 V and shown in Fig. 3.5. For small reverse voltages (V_1 < 10 V) the currents in Fig. 3.5 match well with the simulations until after the first current peak. After this, the simulated current rapidly decays to zero while in the measurements an additional peak is observed. This additional peak will be discussed in chapter 5. For large reverse voltages (V_1 >10 V) there is also another

difference in the first part of the current: the first peak in the measurements is observed earlier than in the simulations.

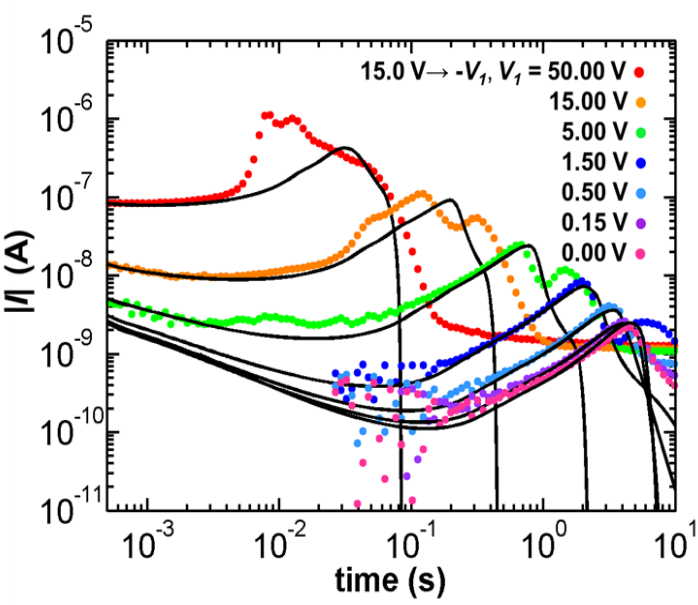

Figure 3.5: A comparison between measured (colored dots) and simulated (black lines) transient reversal currents for device 2 (ϕ_m = 0.003 of OLOA 11K in dodecane, d = 48.4 μm, S = 1 cm^2 and λ =17000) for 15 V→-V_1, with V_1 = 0, 0.15, 0.5, 1.5, 5, 15 and 50 V. The match between measured and simulated currents for smaller voltages validates the model. For larger voltages the peak in the measured currents occurs earlier than that of the simulations. Also, a second peak is observed in the measurements which does not match with the simulations. A detailed study about the origin and the properties of CIMs relating to this peak is presented in chapters 5 and 6. The simulation parameters are $\bar{n}$ = 10 μm^{-3} and μ = 1320 μm^2/Vs.

The decreasing/increasing (non-monotonic) shape of the transient reversal currents which is observed in Fig. 3.5 can be explained on the basis of the simulated electric field and the concentration profile of the CIMs between electrodes when switching the voltage from 15 V to –5 V (see Fig. 3.6). The values of the simulation parameters are $\bar{n}$ = 10 μm^{-3} and μ = 1320 μm^2/Vs. Before t = 0 s, the field in the bulk is approximately V_0/d and the electric field next to the electrodes is approximated by the sum of the applied field and field induced by the CIMs that are in the double layer [23,72]. Thus, the total field next to the electrodes is given by $E = \frac{V_0}{d} + \frac{\bar{n}ed}{\varepsilon_o \varepsilon_r}$. When the voltage is reversed from the steady state situation, the field near the

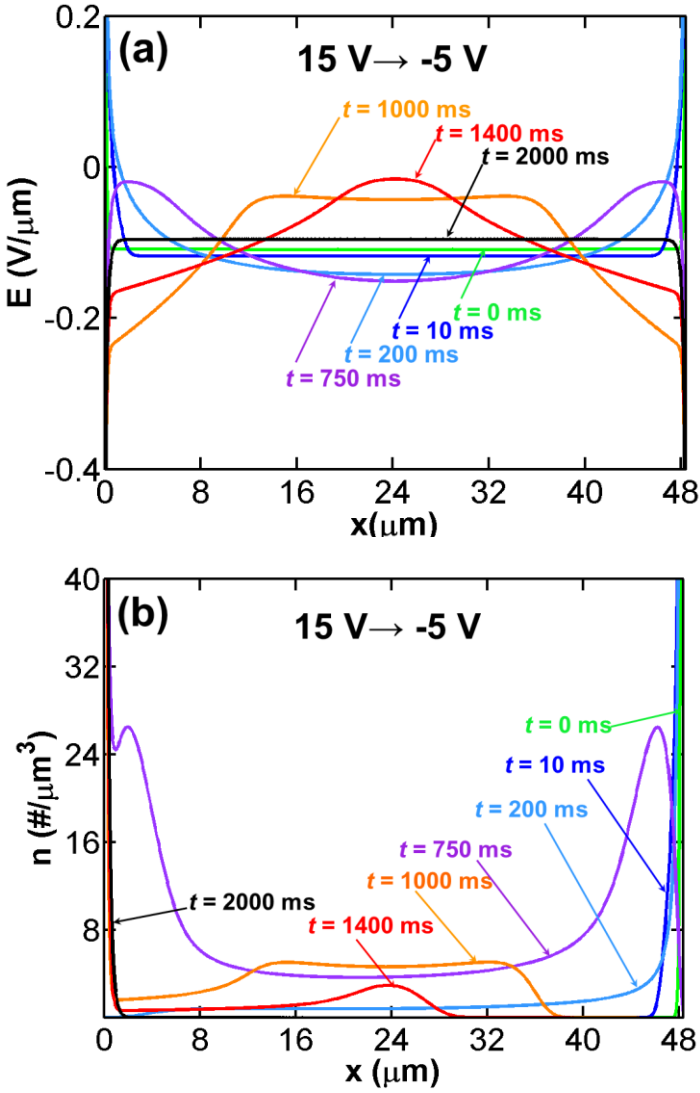

Figure 3.6: Simulated variation in (a) the electric field and (b) concentration of positive CIMs as a function of time in device 2 (ϕ_m = 0.003 of OLOA 11K in dodecane, d = 48.4 μm, S = 1 cm^2 and λ =17000) for the reverse voltage step 15 V→-5 V. The corresponding measured reverse current is shown by green dots with the simulation in black line in Fig. 3.5. Positive CIMs travel from near the positive electrode (x = 48.4 μm) towards the negative electrode (x = 0). In (b) for the purpose of visibility, the limit of y axis is set to 40 μm^{-3}, nevertheless, the area under each curve is equal to $\bar{n} \times d$. The simulation parameters are $\bar{n}$ = 10 μm^{-3} and μ = 1320 μm^2/Vs.

electrodes does not reverse in the case of large values of λ (as one would expect in the case of low values of λ) but becomes approximately $E = -\frac{V_1}{d} + \frac{\bar{n}ed}{\varepsilon_o \varepsilon_r}$, which remains positive when the concentration of CIMs $\bar{n}$ is sufficiently high.

The initial current at t = 0 s, is given by Eq. 3.1. This current corresponds to the change in the field (V_0 + V_1)/d by reversing the polarity of the applied voltage. Up to 10 ms the current in Fig. 3.5 for 15 V→- 5V (green dots) decreases because most CIMs are in the region near the electrodes where the field still has the same sign as before the voltage reverse (see Fig. 3.6 (a)). The current during this time is limited to diffusion of CIMs from the double layers and scales with time as $1/\sqrt{t}$. For larger times, more and more CIMs diffuse into the bulk where the field is determined by the applied voltage, and their contribution to the field near the electrodes is reduced. As a result more and more CIMs experience the field related to the applied voltage and start moving to the other side of the cell. This explains the increase of the current until 750 ms. At this time, the current starts decreasing because more and more CIMs reach the counter electrode and stop contributing to the current. Eventually, the bulk is completely depleted of CIMs and the current becomes approximately zero around 2000 ms in the simulation. However, in the measurement shown in Fig. 3.5, there is a constant current for t > 2 s which is due to the generation of new CIMs in the bulk due to the disproportionation mechanism. During this, the field becomes $-V_1/d$ (see Fig. 3.6 (a) when t = 200 ms) in the bulk because the initially present CIMs are in the double layer and the generation rate of new CIMs is low.

For the case when V_1<< 1 V, the initial, decreasing and increasing currents can be explained the same way. However, because the magnitude of the applied reverse voltage is low, diffuse double layers are formed after a certain time τ_{DL} and the field is screened completely in the bulk and becomes zero [100]. As a result the CIMs do not separate completely from the bulk towards the opposite electrodes and most of them remain in the bulk.

For the polarizing voltages with amplitude larger than 1 V and with a duration t_0 > 20 s ($d \geq 45$ μm), a second peak is observed in the transient reversal currents for $V_1 \leq$ 10 V in Fig. 3.5, t_0 = 200 s, which is not predicted by the simulations. The origin of this peak is studied in detail in chapter 5.

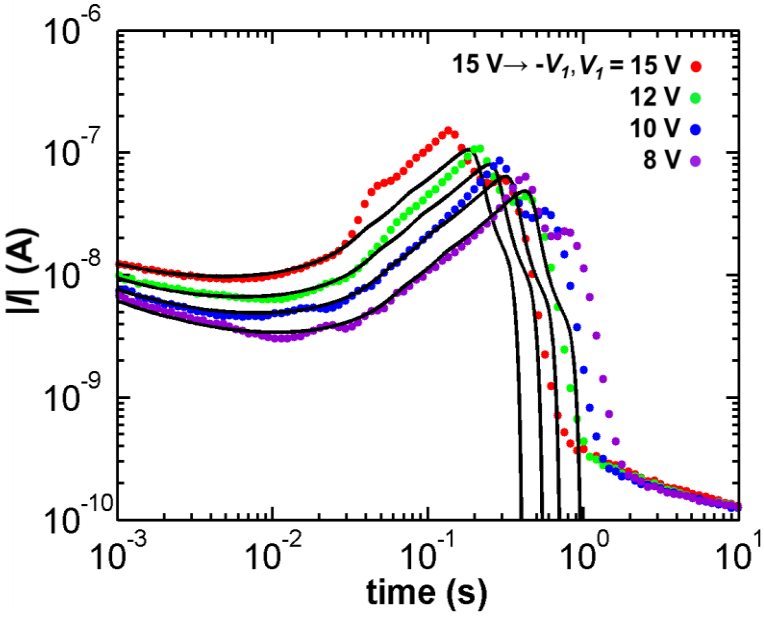

Figure 3.7: Measured (colored dots) and simulated (black lines) transient reversal currents in device 2 (d = 48.4 μm and S = 1 cm^2 with ϕ_m = 0.003 of OLOA 11K in dodecane) for reverse voltage steps 15 V→-V_1 (8,10,12,15 V). The deviations before reaching the maximum current are ascribed to the occurrence of EHD instabilities. The simulation parameters are $\bar{n}$ = 10 μm^{-3} and μ = 1320 μm^2/Vs.

3.3.2.3 Electrohydrodynamic Flow

The agreement between simulations and measurements for the transient reversal current becomes worse when the voltage amplitude increases above 10 V (see Fig. 3.5). More precisely, the peak in the current occurs earlier than expected from the simulations, while the integral of the current remains the same. This discrepancy is attributed to EHD flow in the liquid. In [101,102], a theoretical study is presented on the instabilities that can occur when charge is injected into a dielectric liquid. It was found that the force that the charge exerts on the liquid leads to convection above a threshold voltage $V \geq 99\mu\eta/(\varepsilon_r\varepsilon_o)$. The validity of the equation has been verified experimentally [101]. The calculated value of the threshold voltage is 11V in our experiment which matches with the observations in Fig. 3.5 and Fig. 3.7. Above this threshold voltage, sufficient electrical energy is released by reversing space charge layers, to make the hydrodynamic system unstable [14]. Consequently, the transport is not one-dimensional anymore and domains with liquid flow appear in which the CIMs can move faster and arrive earlier than expected.

Transient current measurements were performed for a wide range of polarization and reverse voltage steps. The measurements are always in good agreement with the simulations for the polarizing voltage steps (not shown) and for the reverse voltage steps applied just after a polarizing voltage step with magnitude V_0 < 1 V (see Fig. 3.5). A discrepancy is observed for reverse voltages above 10 V when the polarizing voltage is higher than 11 V (see Fig. 3.7). This indicates that EHD instabilities occur when space charge layers are inverted very quickly, which happens above a threshold voltage. When a large reverse voltage is applied after a small polarizing voltage, the distribution of the charges remains approximately homogeneous in the device. Therefore, there is no possibility of inversion in space charge layers, hence no EHD effect is observed as indicated by the agreement in the measurements and simulations.

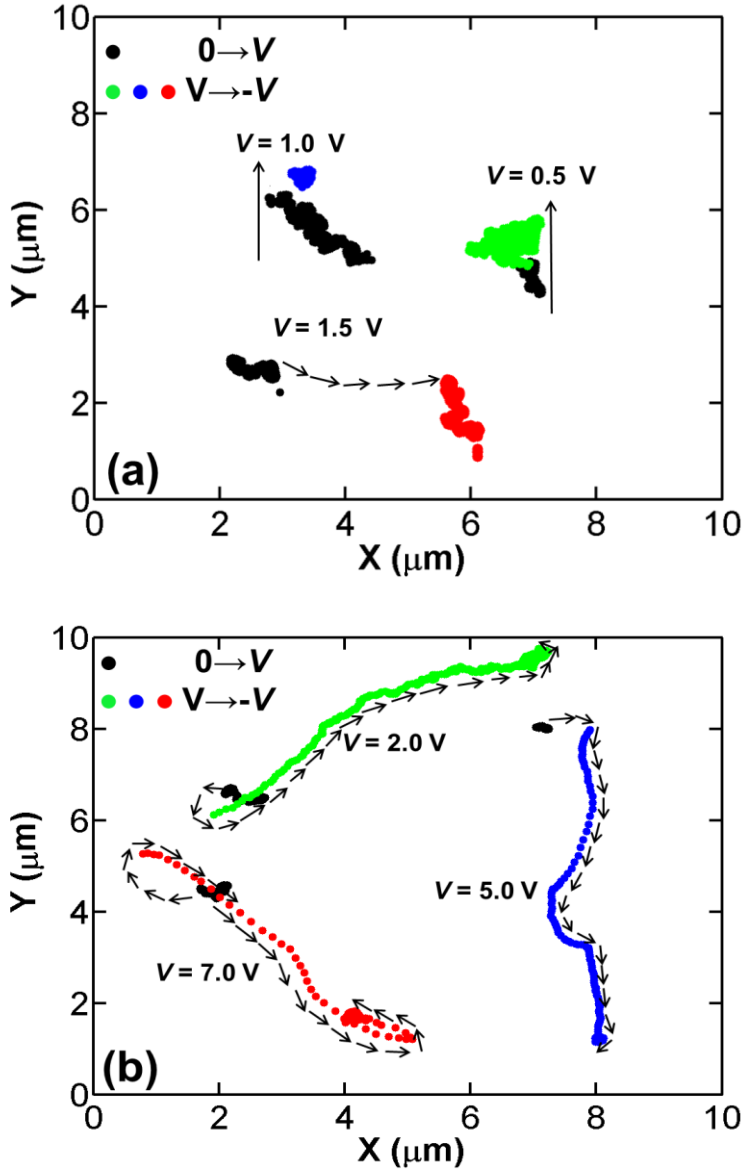

Figure 3.8: Transient trajectories in the *xy*-plane of positively charged PMMA tracer particles in device 2 (ϕ_m = 0.003 of OLOA 11K in dodecane) for polarizing voltages 0→*V* (black dots) and reverse voltages *V*→ -*V* (colored dots). The direction of motion is indicated by arrows. (a) For small voltages (*V* < 1.5 V) the lateral motion is small indicating the absence of EHD flow. (b) For large voltages (*V* > 1.5 V), the lateral motion is small for the polarizing voltage and large for the reverse voltage verifying the occurrence of EHD flow.

3.3.3 Verification of EHD Flow: Transient Trajectories of the Tracer Particles

The occurrence of EHD flow in the liquid is verified with the help of tracer particles. Fig. 3.8 shows microscopic particle trajectories for polarization and reverse voltages. For small voltages (0.5 and 1.0 V), the particle trajectories are mainly orthogonal to the electrodes, which is expected in the absence of EHD flow. However, for reverse voltages with amplitude above 1 V, the tracer particles in Fig. 3.8 (b) indicate important lateral motion (in the *xy*-plane), which does not fit with the drift and diffusion model. From this it is concluded that EHD flows are present in the device at these high voltages. Interestingly, since the mobility of the charged tracer particles is about ten times less than that of the CIMs, the EHD effect can be observed before the tracer particle arrives at the attracting electrode.

The discrepancy for the onset voltage of EHD flow determined by two different methods, i.e. from transient reversal currents (11 V) and from the transient trajectories of the tracer particles (1.5 V) deserves an explanation. The concentration of tracer particles in the dispersion is very small ($\phi_m <$ 0.0001), however, it is possible that the presence of a tracer particle induces EHD flow around it at a relatively low voltage. Another explanation is that EHD flow starts at 1 V, but that the increasing current only becomes visible for voltages above 10 V.

3.4 Conclusions

In this chapter, the transport of charged inverse micelles (CIMs) has been investigated in various situations where the applied voltage is switched to the opposite polarity. For a device with large charge content, two peaks are observed in the reversal current when the duration of the polarizing voltage step ($0 \rightarrow V_0$, $V_0 > 1$V) is long enough.

The experimental results (until the first current peak) up to 10 V are in good agreement with a model of drift and diffusion based on the Poisson-Nernst-Planck (PNP) equations. This indicates that the first peak is due to release of a fixed amount of CIMs from the diffuse double layers formed during the polarizing voltage step ($V_0 > 1$ V) but does not explain the origin of the second peak. However, for larger voltages this simple model does not

describe the measurements well. This discrepancy is attributed to electrohydrodynamic flow, due to which the CIMs are transported faster than predicted by the 1-dimensional PNP equations. Measurements with tracer particles confirm this hypothesis. The obtained value of the threshold voltage (11 V) to cause EHD flow in the liquid matches with theoretical values from literature [101,102].

This study is relevant for electrophoretic displays in which the switching of colloidal particles is influenced electrically and electrohydrodynamically by the presence of CIMs. The performance and appearance of the display is degraded due to particle agglomeration and particle clustering [14,96]. This study reveals that excess presence of free CIMs in such dispersions can trigger EHD flow in the liquid when the voltage is reversed from the steady state of the polarizing voltage, which is a dominant mechanism of particles aggregation [93,95,96].

Chapter 4

Investigation on Newly Generated Charged Inverse Micelles

The second peak in the reversal transient current that is growing with increasing duration of the polarizing voltage, suggests that the peak is related to the CIMs that are generated during the polarizing voltage step. So far little is known about the properties and the electrodynamics of the newly generated CIMs. A detailed study of the generated CIMs provides valuable information for the interpretation and understanding the origin of the second peak.

4.1 Introduction

Transient electrical currents measured in response to a step voltage are due to the separation of initially present CIMs and are used to obtain the concentration, mobility and hydrodynamic radius of the initially present CIMs [6,23,74,77]. The measured non-zero currents after the transient phase are related to the generation of new CIMs in the bulk [6,23,89]. The

generation currents can be used to investigate the mechanism and rate with which the charges are generated [58].

Many features of the electrodynamics and the generation mechanism of CIMs in surfactant systems such as OLOA 11K in dodecance are well-understood [13,77,79,89]. However, when the polarity of the applied voltage is reversed or switched off abruptly after a long polarizing voltage V_0, two peaks are observed in the reversal transient current [77]. The occurrence of the first peak is understood well on the basis of the Poisson-Nernst-Planck (PNP) equations and is related to the initially present amount of CIMs [77]. The second peak cannot be explained by the PNP model [58,77]. It has been observed that the integral of the second peak increases with increasing duration of the preceding polarizing voltage step and is not observed for a small duration of the polarizing voltage step [58,77]. From this, it has been concluded that the peak is a result of the newly generated CIMs. Furthermore, the peak appears just after the first peak which means that the CIMs related to the second peak are released slowly in comparison to the initially present CIMs [77]. This indicates that the newly generated CIMs behave differently at the interfaces. Such a difference in the interfacial behavior could possibly originate from a difference in mobility/size of the inverse micelles [75,77,99].

In this chapter, a thorough investigation is carried out on newly generated CIMs using transient current measurements with an increasing stepwise voltage $V_0 \rightarrow V_1$ (V_0 & $V_1 >> 1$ V and $t_0 >> d^2/(\mu V_0)$). From the measurements the values of the mobility, size and concentration of the newly generated CIMs are extracted. Such information cannot be obtained from the polarization current. From the amplitude and shape of the measured currents, information about the charge generation mechanism can be obtained.

4.2 Analytical Approximations

In this section analytical formulas are derived for the quasi steady state current and for the transient current when the applied voltage is increased stepwise to a voltage of the same polarity $V_0 \rightarrow V_1$, as depicted in Fig. 4.1 (a). For the purpose of clarity, the same model and equations that were discussed in chapter 2 (section 2.5) are re-written here. It is assumed that all the generated CIMs in the presence of an electric field are identical and have the same generation/recombination rate constant and valency. However, it is

assumed that the size and the mobility of the generated CIMs are different than those of the initially present CIMs (but the valency is still z = 1).

In chapter 6, on the basis of the interfacial behavior of generated CIMs, it will be shown that three types of CIMs with different generation rate constants are generated in the bulk in the presence of an applied electric field. Here, the aim is to understand the bulk electrodynamics of the generated CIMs.

The flux due to initially present CIMs is: $\Psi_{\pm} = \pm n_{\pm}\mu E - D\frac{\partial n_{\pm}}{\partial x}$. Similarly the flux due to newly generated CIMs in the presence of an electric field can be written as: $\Psi_{g\pm} = \pm n_{g\pm}\mu_g E - D_g\frac{\partial n_{g\pm}}{\partial x}$. Here, $n_{g\pm}$ is the concentration of the generated positive and negative CIMs, $\mu_g = \mu_{+g} = -\mu_{-g}$ is the mobility and D_g is the diffusion constant, equal to $D_g = (\mu_g k_B T)/e$. The continuity equations for all types of IMs present in the bulk in the presence of an electric field can be written as:

$$\frac{\partial n_{\pm}}{\partial t} = -\frac{\partial \Psi_{\pm}}{\partial x} \tag{4.1}$$

$$\frac{\partial n_{g\pm}}{\partial t} = -\frac{\partial \Psi_{g\pm}}{\partial x} + \beta n_0^2 - \alpha n_{tot+} n_{tot-} \tag{4.2}$$

$$\frac{\partial n_0}{\partial t} = D\frac{\partial^2 n_0}{\partial x^2} - 2(\beta n_0^2 - \alpha n_{tot+} n_{tot-}) \tag{4.3}$$

In Eq. 4.2 and 4.3, it is assumed that the generated CIMs can also recombine with the initially present CIMs, so the recombination term scales with the total concentration of CIMs in the bulk liquid $n_{tot\pm} = n_{\pm} + n_{g\pm}$. In Eq. 4.3, it is assumed that the size and the diffusion constant of the neutral micelles is the same as that of the initially present CIMs. The electric field between the electrodes is determined by Gauss's equation:

$$\varepsilon_0 \varepsilon_r \frac{\partial E}{\partial x} = \rho \tag{4.4}$$

In Eq. 4.1, it is assumed that the concentration of regular CIMs does not change with time (this will be verified in chapter 5 section 5.3.6). Therefore, the generation/recombination rate constant for the initially present CIMs is discarded in the presence of an electric field. The current measured in the external circuit can be expressed as [58,73,91]:

$$I(t) = \frac{eS}{d}\int_0^d \left(\Psi_+ - \Psi_- + \Psi_{g+} - \Psi_{g-}\right) dx \qquad (4.5)$$

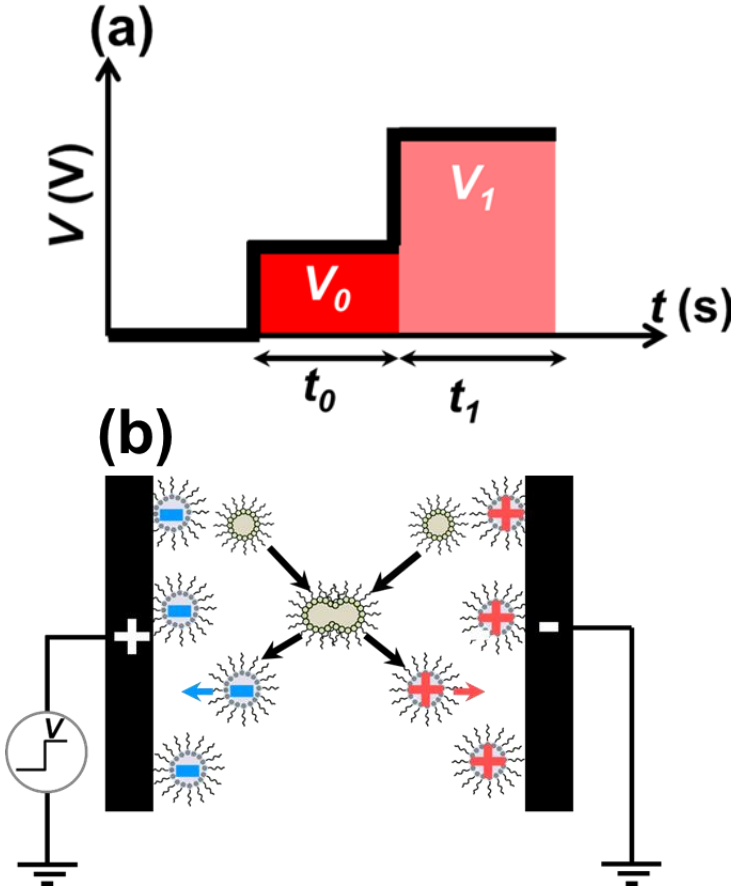

Figure 4.1: Schematic illustration of (a) a stepwise increasing voltage $0 \rightarrow V_0 \rightarrow V_1$ (b) the charge generation process as a result of a disproportionation mechanism.

Analytical formulas that provide insight about the measured and simulated transient currents can be derived for a simple situation in which the generation of new charges in the presence of an electric field is limited to bulk generation and the generation rate is very low. The transit time of the generated CIMs during the voltage step V_0 is given by $t_{gtr,0} = d^2/(\mu_g V_0)$. Knowing the fact that the generation currents for the surfactant system with OLOA 1200 (which is similar to OLOA 11K) can be understood well on the basis of the bulk generation mechanism for voltages larger than 1

V [6,23,89]. The analysis is restricted to the case $\varphi_0 \gg 1$ ($\varphi_0 = V_0/(k_B T/e)$), for which bulk diffusion can be ignored [73]. This also means that the CIMs are transported much faster to the opposite polarity electrode than their generation rate. Therefore, the concentration of CIMs for the situation $\varphi_0 \gg 1$ becomes very low in the bulk. Thus in Eq. 4.2 and 4.3, the term $\alpha n_{tot+} n_{tot-}$ can be ignored. This leads to the conclusion that the concentration of neutral IMs does not change significantly in the bulk and approximately always remains equal to equilibrium value $\bar{n}_0$.

4.2.1 Generation Limited Currents

Let us consider the case in which the CIMs are uniformly distributed in the bulk of the device in the absence of a voltage and then a polarizing voltage step V_0 ($V_0 > 1$ V) is applied at $t = 0$ s. If the duration of the voltage V_o is larger than $t_{gtr,0} = d^2/(\mu V_0)$, then all the CIMs present in the bulk move to the electrodes where they end up in thin diffuse double layers of thicknesses $\delta_0 = 2d/\varphi_0$ [15,73]. Subsequently, the quasi steady state begins during which a very slowly decreasing current is measured due to the generation of new charges [23,89]. During the depletion phase the electric field ($E_0 = V_0/d$) in the device changes significantly due to space charge formation [72]. Since the generation rate of new CIMs in the bulk for a surfactant system such as OLOA 11K in dodecane is very low, after the separation of the initially present CIMs the field in the bulk of the device again becomes equal to $E_0 \approx V_0/d$ [77]. During the quasi steady state, the variation in the concentration of the generated CIMs is given by (ignoring recombination and diffusion):

$$\pm \mu_g E_0 \frac{\partial n_{g\pm}}{\partial x} = \beta n_0^2 \tag{4.6}$$

Since in the model, it is assumed that the generation of new CIMs is a result of bulk disproportionation and surface generation does not play any role, the boundary conditions are:

$$\mu_g E_0 n_{g+}(x = 0) = \mu_g E_0 n_{g-}(x = d) = 0 \tag{4.7}$$

Integrating Eq. 4.6 with boundary conditions yields:

$$n_{g+} = \left(\frac{\beta n_0^2}{\mu_g V_0}\right) x d \tag{4.8}$$

$$n_{g-} = \left(\frac{\beta n_0^2}{\mu_g V_0}\right) d(d - x) \tag{4.9}$$

From Eq. 4.8-4.9, the total number of newly generated CIMs in the bulk can be calculated as: $N_{g\pm} = S\int_0^d n_{g\pm}\, dx$:

$$N_{g\pm} = \frac{S\beta n_0^2 d^3}{2\mu_g V_0} = \left(\frac{S\beta n_0^2 d}{2}\right) \times t_{gtr,0} \tag{4.10}$$

The average concentration of generated CIMs is then: $n_{g\pm} = N_{g\pm}/(dS) = \frac{\beta n_0^2 d^2}{2\mu_g V_0} = \left(\frac{\beta n_0^2}{2}\right) \times t_{gtr,0}$.The fact that the average concentration of generated CIMs scales inversely with the applied voltage can be understood by the fact that the larger the voltage the quicker the depletion of generated CIMs from the bulk. The quasi steady state current due to generated CIMs can be calculated using Eq. 4.11:

$$I_g = \frac{2e\left(\frac{S\beta n_0^2 d}{2}\right) \times t_{gtr,0}}{t_{gtr,0}} = \beta n_0^2 edS \tag{4.11}$$

The quadratic scaling of the quasi steady state current with the concentration of neutral micelles is the direct consequence of the bulk disproportionation generation mechanism.

4.2.2 Transient Generation Current for Voltage Step $V_0 \rightarrow V_1$

Now, let us consider the case when the voltage is increased stepwise to a voltage of the same polarity (let us say at t = 0 s), i.e. $V_0 \rightarrow V_1$, from the quasi steady state of the polarizing voltage step. The measured resulting current has two contributions, the first one is due to readjustment of the double layers (I_{DL}) at the electrodes and the second one is related to the movement of the generated CIMs (I_{gtrs}) which were present in the bulk at t = 0 s and the newly generated CIMs during the transient. The total current can be written as:

$$I_{(V_0 \rightarrow V_1)}(t) = I_{DL}(t) + I_{gtrs}(t) \tag{4.12}$$

In the following sections, both parts of the currents that contribute to the overall transient current will be discussed.

4.2.2.1 The Double Layer Rearrangement Current

The double layer rearrangement current is measured during a very short time t < 100 μs when the voltage is increased from V_0 to V_1 at t = 0 s. Consequently, the electric field in the device increases by $(V_1 - V_0)/d$. Due to this increase in the field, the charges situated in the double layers ($\bar{n}Sd$) move towards the electrodes with a velocity: $v = \mu(V_1 - V_0)/d$. This movement of charges result in an initial flux which can be calculated using: $\Psi_{\pm} = \pm\mu n_{\pm}(V_1 - V_0)/d$. Because of this flux of charges at t = 0 s, the current is:

$$I_{DL}(t = 0) = 2e\bar{n}S\mu\frac{(V_1 - V_0)}{d} \tag{4.13}$$

The time needed for the double layer to attain a new equilibrium (of thickness $\delta_1 = 2d/\varphi_1$ [73]) will be $t < \delta_1/v$. This gives $t < 2d^2/(\mu(V_1 - V_0)\varphi_1)$ ($\varphi_1 = V_1/(k_BT/e)$), during this time the current decreases rapidly. Afterwards the remaining currents are due to readjustment of the linear part of the double layers.

4.2.2.2 Transient Generation Current

Let us now consider the transient generation current, which also has two contributions. The first one is due to the fixed amount of generated charge ($N_{g\pm}$) present in the bulk at t = 0 s, which moves faster in response to the increased field ($E_1 = V_1/d$), while the second contribution is the result of newly generated CIMs. The first contribution can be modeled using Eq.4.2 without taking into account the generation/recombination and diffusion (since $E_1 >> 1/d$) as:

$$\frac{\partial n_{g\pm}}{\partial t} = \mp\mu_g E_1 \frac{\partial n_{g\pm}}{\partial x} \tag{4.14}$$

Using Eq. 4.6, Eq. 4.14 can be written as:

$$\frac{\partial n_{g\pm}}{\partial t} = -\frac{V_1}{V_0}\beta n_0^2 \tag{4.15}$$

From Eq. 4.15, the concentration of generated CIMs at each position in the device decreases linearly until it reaches a new equilibrium value. The concentrations of the generated CIMs in the device in the new equilibrium are:

$$n_{g+} = (\beta n_0^2 x d)/(\mu_g V_1) \tag{4.16}$$

$$n_{g-} = (\beta n_0^2 d(d-x))/(\mu_g V_1) \tag{4.17}$$

With increasing duration of the voltage step V_1 and because of the spatial variation in the concentration of the generated CIMs, two regions are formed in the device. In the first region the concentration has already reached a new equilibrium while in the second the concentration of the generated CIMs varies according to:

$$\frac{\partial n_{g\pm}}{\partial x} = \mp \frac{\beta n_0^2 d}{\mu_g V_0} \tag{4.18}$$

The time dependent concentration $n_{g+}(x,t)$ of the generated CIMs during the voltage step V_1 is given by:

$$n_{g+} = \begin{cases} \dfrac{\beta n_0^2 d}{\mu_g V_1} x, \quad 0 < x < \dfrac{\mu_g V_1 t}{d} \\ \dfrac{\beta n_0^2 d}{\mu_g V_0} x - \beta n_0^2 t \left(\dfrac{V_1}{V_0} - 1\right), x < \dfrac{\mu_g V_1 t}{d} < d \end{cases} \tag{4.19}$$

From symmetry it can be seen that:

$$n_{g-}(x,t) = n_{g+}(d-x,t) \tag{4.20}$$

The time taken by the generated CIMs to reach the opposite polarity electrode in a field with magnitude V_1/d is: $t_{gtr,1} = d^2/(\mu_g V_1)$. Using Eq. 4.5 and ignoring the diffusion term, the currents during the transient phase are given by:

$$I_{gtrs}(t) = \begin{cases} I_g \left\{ \frac{V_1}{V_0} - \frac{2t}{t_{gtr,1}} \left(\frac{V_1}{V_0} - 1 \right) + \frac{t^2}{{t_{gtr,1}}^2} \left(\frac{V_1}{V_0} - 1 \right) \right\}, 0 \le t \le t_{gtr,1} \\ I_g \quad , t_{gtr,1} < t, \end{cases} \tag{4.21}$$

The initial current is given by $I_{gtrs}(t = 0) = I_g(V_1/V_0)$, afterwards the current decreases quadratically and reaches the quasi steady state at time $t_{gtr,1}$. The total transported charge during the transient can be calculated by integrating Eq. 4.21 from $t = 0$ to $t_{gtr,1}$ and is equal to:

$$Q_{gtrs} = \frac{I_g}{3}\left(t_{gtr,0} + 2t_{gtr,1}\right) \tag{4.22}$$

In Eq.4.22, the total transported charge to the electrodes at time $t_{gtr,1}$, has two contributions: the first contribution is due to the initially present charge in the bulk at t = 0 when the voltage is increased to V1 and the second contribution is due to the newly generated charges in the bulk during the transit time $t_{gtr,1}$. For the case when $V_1 >> V_0$, then $t_{gtr,1} \ll t_{gtr,0}$ (since $t_{gtr,1} \propto 1/V_1$), which means the contribution due to newly generated CIMs during the time $t_{gtr,1}$ will be negligible. Thus, the total transported charge to the electrodes for the case when $t_{gtr,1} << t_{gtr,0}$ is:

$$Q_{gtrs} \approx \frac{I_g\, t_{gtr,0}}{3} = \frac{2eN_{g\pm}}{3} \tag{4.23}$$

4.3 Materials and Methods

A device similar to the device that has been used in chapter 3 is employed to perform current measurements, with d =19.5 μm and S = 1 cm^2. Solutions of OLOA 11K with ϕ_m = 0.01, 0.03 and 0.1 are prepared in dodecane. The device is filled with the prepared solution and the electrodes of the device are connected to the measurement set-up. The initial homogenous situation is ensured by short-circuiting the electrodes for 1000 s. Then, a polarizing voltage step $0 \rightarrow V_0$ is applied for a duration of t_0 = 40 s ($t_0 >> d^2/(\mu V_0)$) and subsequently, the magnitude of the applied voltage is increased to $V_0 \rightarrow V_1$, such that $V_1 > V_0$.

4.4 Results and Discussion

4.4.1 Comparison Between the Measurements and the Simulations

Fig. 4.2 (a, b) shows a comparison between the measured (dashed blue line), simulated (black line) and analytically calculated (red line) current. For the simulations Eqs. 4.2 to 4.5 are solved with an initially homogeneous distribution of initially present CIMs and with blocking boundary conditions. The values of $\bar{n}, \mu$ and α are obtained by matching simulations with the measurements. The used values of the parameters in Fig. 4.2 (a, c) for which the measurement matches with the simulation are: $\mu = \mu_g = 1000$ μm^{2}V^{-1}s^{-1}, $\bar{n}$ = 439 μm^{-3} and $\alpha = 5.1 \times 10^{-22}$ m^{3}s^{-1}. Similarly, for Fig. 4.2 (b & d) the used values are $\mu = \mu_g = 1150$ μm^{2}V^{-1}s^{-1}, $\bar{n}$ = 70 μm^{-3} and $\alpha = 2.05 \times 10^{-22}$ m^{3}s^{-1} respectively. Using the estimated value $\sqrt{\alpha/\beta} \cong 51$ of surfactant OLOA 1200 and knowing the fact that OLOA 1200 is very similar to OLOA 11K, the values of β and $\bar{n}_0$ for OLOA 11K in dodecane are obtained [6,23,58]. The obtained values are β =1.96×10^{-25} m^{3}s^{-1} and $\bar{n}_0 \approx$ 3.57×10^{21} m^{-3} (ϕ_m = 0.1) respectively.

In Fig. 4.2 (a, b), the initial current $I_{V_0 \rightarrow V_1}(t = 0\ \mathrm{s})$ in the simulation matches quite well with the current that is calculated using Eq. 4.13. The times during which the current due to the non-linear part of the double layer decreases rapidly ($t < 2d^2/(\mu(V_1 - V_0)\varphi_1)$) are t < 21 μs for Fig. 4.2 (a) and 0.9 ms for Fig. 4.2 (b). Then, the double layer current decreases exponentially [58].

However, the exponentially decaying currents are not visible in Fig. 4.2 (a, b) because of a large contribution of the transient current. The time scale of the exponential current in Fig. 4.2 (a) is $t > 40$ µs, while that in Fig. 4.2 (b) is $t > 1$ ms. Afterwards, the simulated currents (black line) match with the currents (red line) that are calculated using Eq. 4.21 and with the measured current (dashed blue line).

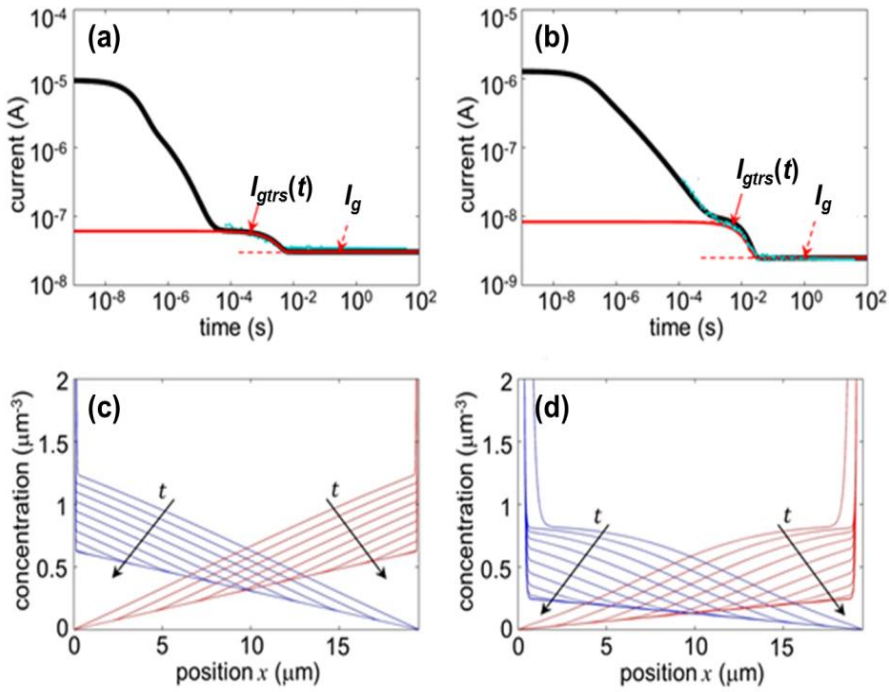

Figure 4.2: A comparison between the simulated (black line), analytically calculated (red line) and measured transient current (blue dots) for the device with $d = 19.5$ µm filled with ϕ_m of OLOA 11K in dodecane for a stepwise increasing voltage $V_0 \rightarrow V_1$. In (a) for $\phi_m = 0.1$, $\bar{n} = 439$ µm^{-3}, $V_0 = 30$ V and $V_1 = 60$ V. In (b) for $\phi_m = 0.03$, $\bar{n} = 70$ µm^{-3}, $V_0 = 3$ V and $V_1 = 10$ V. The level of the generation limited current (I_g) is shown by red color dots. In (c & d), the corresponding transient concentration variation of the generated positive (red color lines) and negative (blue lines) CIMs are shown at linearly spaced times, i.e. $t = j \times t_{gtr,1}$ with $j = 1, 2, \ldots, 10$.

In Fig. 4.2 (c & d), the transient concentration of the generated positive (red lines) and negative (blue lines) CIMs between the electrodes are shown at times $t = j \times t_{gtr,1}$ with $j = 1, 2, \ldots, 10$. The linearly decreasing concentration profile with $t_{gtr,1}$ is given by Eq. 4.19. For the case when the applied voltage

is not large enough, the space charge due to the generated CIMs leads to a spatially inhomogeneous and smaller electric field ($E_0 < V_0/d$) during the quasi steady state. A direct consequence of the space charge due to the generated CIMs is shown in Fig. 4.2 (d), in which the transient concentration profile of the generated CIMs shows a deviation from the linearly decreasing profile as predicted by Eq. 4.19. As a result of the space charge effect, the calculated current shown in Fig. 4.2 (b) is slightly smaller than the simulated current.

Fig. 4.3 shows the measured transient currents with the simulations as a function of increasing ϕ_m, V_0 and V_1. A good match between the measurements and simulations, at least for $V_1 < 30$ V, validates the drift and diffusion model. From the polarization currents (0 V$\rightarrow V_0$) (not shown) the concentration and the mobility of the initially present CIMs is estimated using the same method that has been described in chapter 2, section 2.5.1. The obtained concentrations are $\bar{n}$ =70, 165 and 439 μm^{-3} for ϕ_m = 0.01, 0.03 and 0.1 respectively, following the linear relation $\bar{n} \cong 4500\ \mu m^{-3} \times \phi_m$ (Fig. 4.4, red trend line). The observed linear relation between $\bar{n}$ and ϕ_m validates the assumption of the disproportionation mechanism for charge generation. The obtained values of the mobility for ϕ_m = 0.01, 0.03 and 0.1 are μ = 1150, 1250 and 1000 μm²V^{-1}s^{-1} respectively. This leads to the value of the mobility: μ = (1100 ±100) μm²V^{-1}s^{-1}.

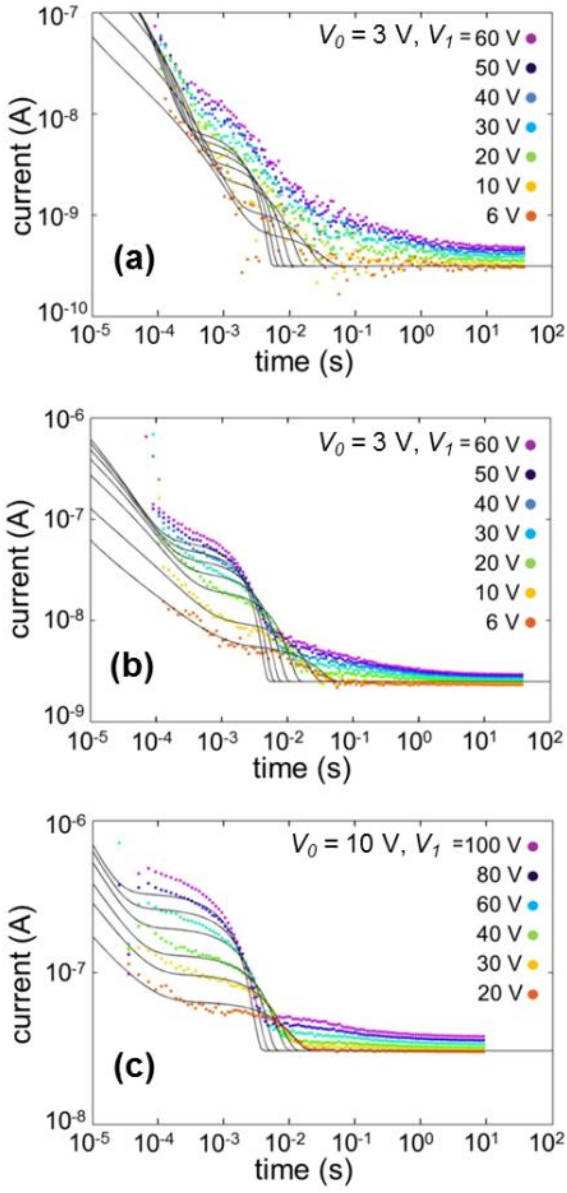

Figure 4.3: Measured transient currents (colored dots) due to bulk generation of new charges are compared with the simulations (black lines) for $V_0 \rightarrow V_1$ performed on the device with d =19.5 μm and S = 1 cm^2. The device is filled with (a) ϕ_m = 0.01 (b) ϕ_m = 0.03 and (c) ϕ_m = 0.1.

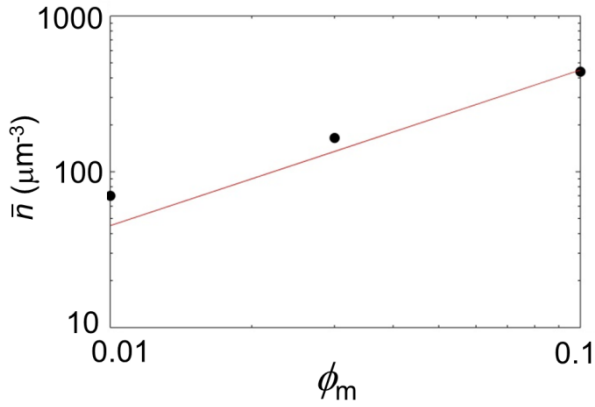

Figure 4.4: Linearly increasing equilibrium concentration of the initially present CIMs ($\bar{n}$) with increasing surfactant mass fraction verifies the disproportionation mechanism, as shown by the linear trend line (red line): $\bar{n} \cong 4500\ \mu\ \mathrm{m}^{-3} \times \phi_m$.

According to the bulk disproportionation mechanism, the quasi steady state currents should be independent of the magnitude of the applied voltage. However, the experimental results shown in Fig. 4.3, show that the quasi-steady-state current increases slightly (less than a factor 1.5) when the applied voltage increases by a factor of 10 (from 6 V to 60 V) or a factor of 5 (from 20 V to 100 V). This increase in the current can be attributed to additional effects such as surface-generation/Faradaic reactions that are not considered in the model. Fig. 4.5 shows the quadratically increasing quasi steady state current with increasing ϕ_m in the solution. The current follows the trend line $I_g = 305 \times \phi_m^2$ nA, showing that $I_g \propto \bar{n}^2$, which is expected from the bulk disproportionation mechanism.

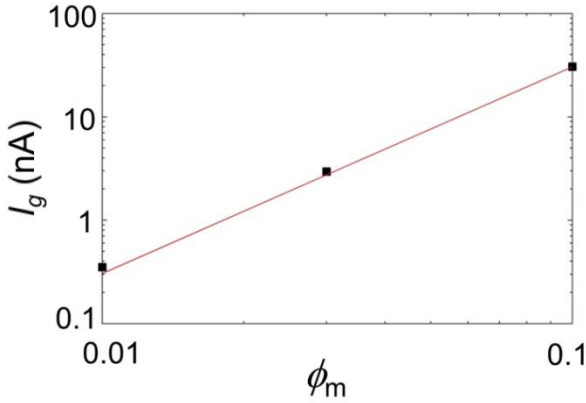

Figure 4.5: The quasi steady-state current scales quadratically with ϕ_m (ϕ_m= 0.01, 0.03 & 0.1). The trend line (red line) shows $I_g = 3050 \times \phi_m^2$ nA.

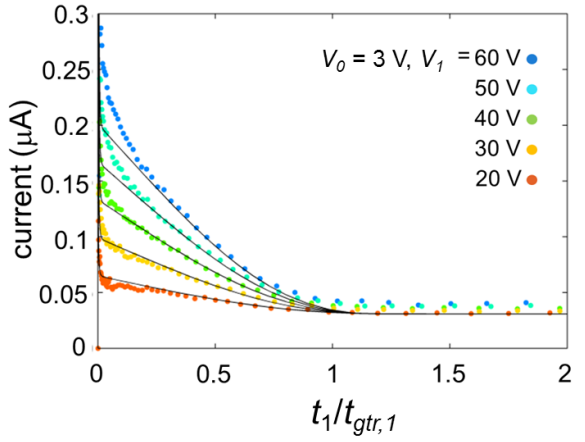

Figure 4.6: The transient generation currents (color dots) are compared with the simulations (black lines) for ϕ_m = 0.1 and V_0=10 V and V_1= 20 V to 60 V from Fig. 2 (c) on linear and normalized axes.

Fig. 4.6 shows the quadratically decreasing transient generation current which is the consequence of the bulk generation mechanism, Eq. 4.21. For the purpose of clarity the time axis in Fig 4.6 has been normalized to the transit-time $t_{gtr,1} = d^2/(\mu_g V_1)$, assuming $\mu_g = \mu$, which will be verified in the next section. For a surface generation mechanism, a uniform concentration of charges in the steady state would be expected, resulting in a

linearly decreasing transient generation current. To fit a linearly decreasing current to the experimental data shown in Fig. 4.6, a two times larger value of the mobility is required in comparison to the case of bulk generation. Nevertheless, the linear proportionality of the generation-limited current with d indicates that the generation is occurring in the bulk which has been already verified by the experimental observations of Figs. 4.4 & 4.5. The simulations match with the measurements when V_1 < 30 V, see Figs. 4.3 (b & c) and for V_1 > 30 V an additional linearly decreasing current appears in the measurements which cannot be explained by the drift and diffusion of the CIMs of the mobility μ_g. One explanation for this mismatch is that weak EHD instabilities may exist during the quasi steady state of the voltage step 0→V0 and when the voltage is increased stepwise to a large voltage ($V_0 \rightarrow V_1$, $V_1 > 3V_0$) the instabilities are amplified and EHD flow occurs in the liquid. As a result of EHD flows the CIMs can be transported quickly to the electrodes, resulting in a larger current. An alternative explanation is that a small fraction of the generated CIMs may be doubly charged and can move twice faster than the CIMs with an univalent charge. The movement of CIMs with double charge could result in an additional linearly decreasing current. Here it is important to note that the effect of the doubly charged generated CIMs can be seen only at the large voltages because at the low voltages they will recombine due to strong electrostatic attraction.

4.4.2 The Concentration and the Mobility of the Newly Generated CIMs

Using the analytical formulas and simulations, the concentration and mobility of newly generated CIMs can be extracted from the transient generation currents ($V_0 \rightarrow V_1$) shown in Fig. 4.3 (a-c). The total generated charge present in the bulk at t = 0 s ($V_0 \rightarrow V_1$) can be calculated by integrating the transient current and correcting for the exponential part of the double layer current and the quasi steady state level of the current. For the measurement shown in Fig. 4.3 (b) with ϕ_m = 0.03, $V_0 = 3$ V and $V_1 = 60$ V, Q_{gtra} = 1.51×10^{-10} C. Then, using Eq. 4.23 which is valid for $V_1 >> V_0$, the concentration of the charge present in the bulk at t = 0 s is $N_{g\pm} = 1.41\times10^{9}$. From this value the average concentration of the generated CIMs at t = 0 s in the bulk is $\langle n_{g\pm} \rangle = 0.72$ μm^{-3}. This value is 230 times smaller than that of the equilibrium concentration of the CIMs $\bar{n}$ = 165μm^{-3}. Similarly, the transit

time $t_{gtr,1}$ = 5.1 ms can be used to estimate the mobility of the newly generated CIMs: $\mu_g = d^2/(V_1 t_{gtr,1})$=1240μm²V^{-1}s^{-1}. The obtained values of the mobility match well with the mobility value of the regular CIMs: μ = 1250 μm²V^{-1}s^{-1} obtained for the same ϕ_m , i.e. ϕ_m = 0.03. Similarly for ϕ_m = 0.1, $V_0 = 10$ V and $V_1 = 60$ V, Q_{gtra} = 4.16×10^{-10} C, which corresponds to the average concentration of the generated CIMs in the bulk of 2 μm^{-3}. The transit time $t_{gtr,1}$ = 5.3 ms results in μ_g =1200 μm²V^{-1}s^{-1}, which is very close to the value μ = 1000 μm²V^{-1}s^{-1} of the regular CIMs obtained for ϕ_m = 0.1. Also, the simulated currents, measured currents and analytically calculated currents shown in Figs. 4.2, 4.3 & 4.6 match well with values of μ_g that are equal to μ. From this, it can be concluded that both regular and newly generated CIMs have the same size and the same mobility.

4.5 Conclusions

The mobility of newly generated CIMs is found to be the same as the mobility of the CIMs that were present in equilibrium. Also, the analysis of the steady state current shows that the CIMs are generated in the bulk and the generation of new CIMs is according to the disproportionation mechanism. Despite of the same size, the delayed release of the generated CIMs for reversal/relaxation voltages, compared to that of initially present CIMs indicates that there are other physical differences in the generated CIMs. Consequently, the generated CIMs behave differently at the interfaces and are released with a delay, when the applied voltage is reversed or switched off.

Chapter 5

Adsorption and Release of Newly Generated Charged Inverse Micelles

The mobility and the corresponding hydrodynamic size of newly generated CIMs are the same as for CIMs present in equilibrium, as demonstrated in chapter 4. However, the occurrence of the second peak in the reversal current indicates that there is a difference in the electrical behavior of CIMs at the interfaces. The investigation of such physical differences in the CIMs causing them to behave differently at the interfaces and the mechanism of the second current peak sheds light on new electrodynamic phenomena in non-polar liquids.

5.1 Introduction

On the basis of transient electrical behavior, surfactant systems can be categorized in two broad categories. The first category corresponds to surfactant systems in which the generation rate of new charges is so high that when a voltage is applied the concentration of CIMs in the bulk remains approximately equal to the equilibrium concentration. Surfactant systems with small micelle sizes (r < 3 nm) such as AOT and Span 85 fall in this category [74]. Due to the small size of the CIMs, they are attracted very

strongly by their image charge in the electrodes, where they end up in interface layers [13,74]. The overall electrical behavior of these surfactant systems can therefore be modeled as a resistor in series with an interface capacitor [13,76]. The second category corresponds to surfactant systems in which the generation rate is low enough so that the bulk can get completely depleted when a voltage larger than 1 V is applied [6,58]. The CIMs formed by these types of surfactant form a diffuse double layer at the interfaces [6,15] as indicated by an exponential decrease in the transient polarization current with a time constant $\tau_{DL} = \frac{\lambda_{DL} d}{2D}$ for a polarizing voltage with $V_0 << 1$ V [91,100]. Surfactant systems with large micelle sizes ($r > 3$ nm) fall in this category, such as OLOA 11 K, Span 80, and Solsperse 13940 [58,73,74].

In the second category of surfactant systems with large micelles such as OLOA 11K, when the voltage is reversed abruptly ($V_0 \rightarrow -V_1$) after a sufficiently long polarizing voltage step ($0 \rightarrow V_0$, $V_0 > 1$ V), a second peak is observed in the transient current, which is not explained by drift and diffusion [58,77]. No such current peak is observed in the first category of surfactant systems, which can be understood from the fact that the newly generated CIMs end up in the interface layers from which they are never released because of strong attractive forces from counter charges situated in the electrodes.

The measurements in this chapter indicate that the second peak in the second category of surfactant systems is related to the release of newly generated CIMs which accumulate at the electrodes during the long polarizing voltage step [58,77]. By increasing the polarizing voltage stepwise to a higher voltage of the same polarity, the mobility of the newly generated CIMs has been measured and found to be the same as that of the regular CIMs present in equilibrium [58]. From this, it follows that the charge ($+e$ or $-e$) and the radius of the charges are probably also the same. However, if the newly generated CIMs would be physically identical to the regular CIMs they would also end up in the diffuse double layers at the electrodes when a voltage step is applied. However, the analysis of the second peak during the reverse voltages ($V_0 \rightarrow -V_1$) indicates that the newly generated CIMs are released later than the regular CIMs that were originally present. This means that the electrical behavior at the interfaces and

consequently also the release mechanism for the newly generated CIMs is different than for regular CIMs.

In this chapter, using transient current measurements, firstly the effect of the polarizing voltage step duration/magnitude, cell thickness and weight fraction of the surfactant in the suspensions on the second peak is investigated. Secondly, the release mechanism of the generated CIMs is investigated by performing different types of experiments. These experiments confirm that the second peak is a consequence of newly generated CIMs, that do not populate the diffuse double layer, but instead adsorb at the interfaces and end up in the interfacial layers. When the voltage is reversed or switched off, a small fraction of generated CIMs is released from the interfaces. Importantly, it is found that only negative charges are released, whereas no signal is obtained from positive adsorbed charges.

5.2 Materials and Methods

The same measurement devices and methods are used as described in chapter 2. The space between the electrodes of the devices is filled with a mixture of OLOA 11K in dodecane. Then, six types of experiments are performed as shown in Fig. 5.1 to investigate the origin of the second peak in the reversal current.

In the first type of experiment (Type A) the effects of the polarizing voltage (V_0) step duration (t_0), cell thickness (d) and mass fraction (ϕ_m) on the integral of the second peak in the reversal current are investigated. The experiment sequence is as follows. Firstly a polarizing voltage step $0 \rightarrow V_0$ ($V_0 > 1$ V) of duration t_0 is applied, then the polarity of the voltage is reversed ($V_0 \rightarrow -V_1$) for a duration t_1 ($t_1 = 100$ s) and finally the device is short circuited ($V_1 \rightarrow 0$) for $t_{s0} = 10000$ s. For the next polarizing voltage step, the same cycle is repeated again which can be summarized as: $0 \rightarrow V_0$ (t_0)$\rightarrow -V_1$(t_1)$\rightarrow 0$ ($t_{s0} = 10000$ s). The same sequence is repeated for another cell thickness and for different values of ϕ_m. In the second type of experiment (Type B), the effect on the second peak is investigated for repeated switching of the voltage after a long polarizing voltage. The experimental sequence is as follows: $0 \rightarrow V_0$ (200 s)$\rightarrow -V_1$ (100 s)$\rightarrow V_1$ (100 s)$\rightarrow -V_1$(100 s) and so on.

In the third type of experiment (type C) the effect of the short-circuit time on the reversal current is studied. In the experiment firstly a polarizing voltage step 0→V_0 (V_0 > 1 V) of t_0 = 10000 s is applied, after which the electrodes are short-circuited for a time t_{s1} (t_{s1} = 1 to 30 s). Subsequently, a voltage step 0→V_2 (V_2 = 5 V) is applied for t_2 = 10 s and the current is measured. The following cycle is repeated for different values of V_2 and t_{s1}: 0 (5000 s) → V_0 (t_0 = 10000 s)→ 0 (t_{s1})→ V_2 (t_2 = 10 s)→ 0 (t_{s0} = 10000 s).

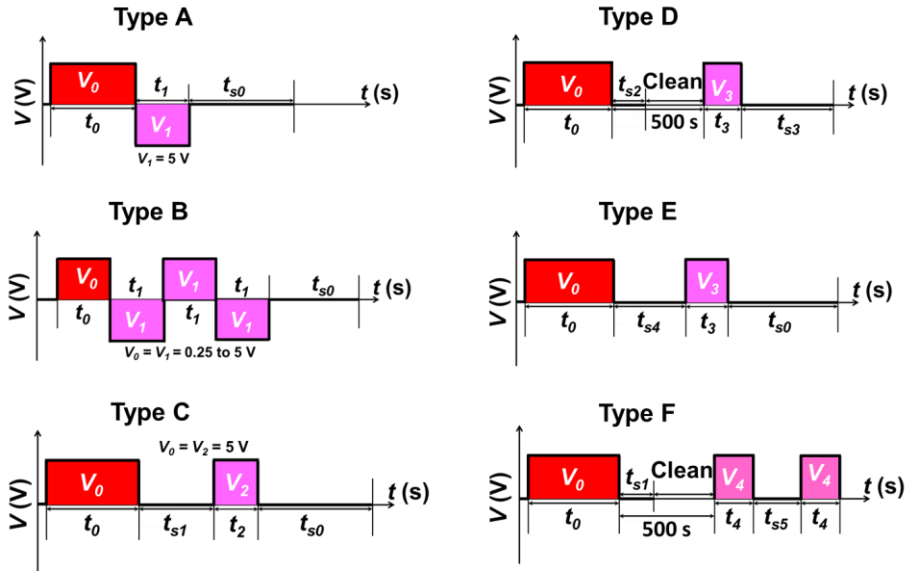

Figure 5.1: Schematic illustration of the voltage versus time sequences for various types of transient current experiments. Type A: the duration t_0 is varied. Type B: repeated switching of the voltage. Type C: the short-circuit time t_{s1} is varied from 1 to 30 s. Type D: the bulk liquid is replaced by dodecane (clean) and V_3 is varied. Type E: t_{s4} is varied from 100 s to 5000 s. Type F: t_{s5} is varied from 500 s to 50000 s.

In the fourth type of experiments (type D), the electrodes are short-circuited for t_{s2} = 30 s after the polarizing voltage step and then are disconnected. Subsequently, the space between the electrodes is replaced by air by sucking out the liquid with a suction pump and then refilled with pure dodecane. This procedure is repeated at least 10 times to ensure complete cleaning of the device, so the bulk of the device is free of any trace of IMs/CIMs or surfactant. Finally, the electrodes are re-connected to the measurement setup. Then a voltage step 0→V_3 is applied, the resulting current is measured and finally the device is short-circuited for a duration of t_{s3} = 50000 s. The

following cycle of experiments is repeated for different values of V_3: 0 (5000 s) → V_0 (t_0 = 10000 s) → 0 (t_{s2} = 30 s) → cleaning procedure → V_3 (t_3 = 300 s).

In the fifth type experiment (type E), the same procedure is repeated that is used in the experiment type C, the only difference being the duration of the short circuit time t_{s4} which goes from 10 s to 10000 s. The sixth type of experiment (type F) is, up to the cleaning procedure, similar to that of the experiment type D. Afterwards, a voltage step 0→V_4 is applied and then the device is short-circuited for a duration of t_{s5} and a voltage step 0→V_4 is applied again.

5.3 Results

5.3.1 Origin of the Second Peak

The results of the reversal transient current measurements as a function of the polarizing voltage step duration (t_0), cell thickness (d) and mass fraction (ϕ_m) of OLOA 11K for the experiment type A are shown in Fig. 5.2. Fig. 5.2 (a) shows that, for a short duration of the polarizing voltage step (t_0 = 10 s), there is a single peak in the reversal current, which is well-understood on the basis of the Poisson-Nernst-Planck (PNP) equations [77]. For longer durations of the polarizing voltage step (t_0 > 100 s for $d \leq 20$ μm) there is an additional peak in the current, starting at t = 0.15 s, growing with increasing duration of the polarizing voltage step t_0, and saturating for t_0 > 3000 s. The effect of the cell thickness and the duration of the polarizing voltage is evaluated by integrating the current of the second peak over the interval t = [0.15 to 1 s] to obtain Q_{sp}. Fig. 5.2 (b) indicates that the saturation level of Q_{sp} scales roughly linearly with the cell thickness (for d >10 μm) as $\left(8.8 \times 10^{-4} \frac{\mathrm{C}}{m}\right) \times d$. Fig. 5.2 (c) shows that an increase in the mass fraction ϕ_m of the surfactant leads to an increase in Q_{sp}. The saturation level of Q_{sp} (for large values of t_0) is approximately proportional to ϕ_m (for $\phi_m \leq 0.012$), see Fig. 5.2(c).

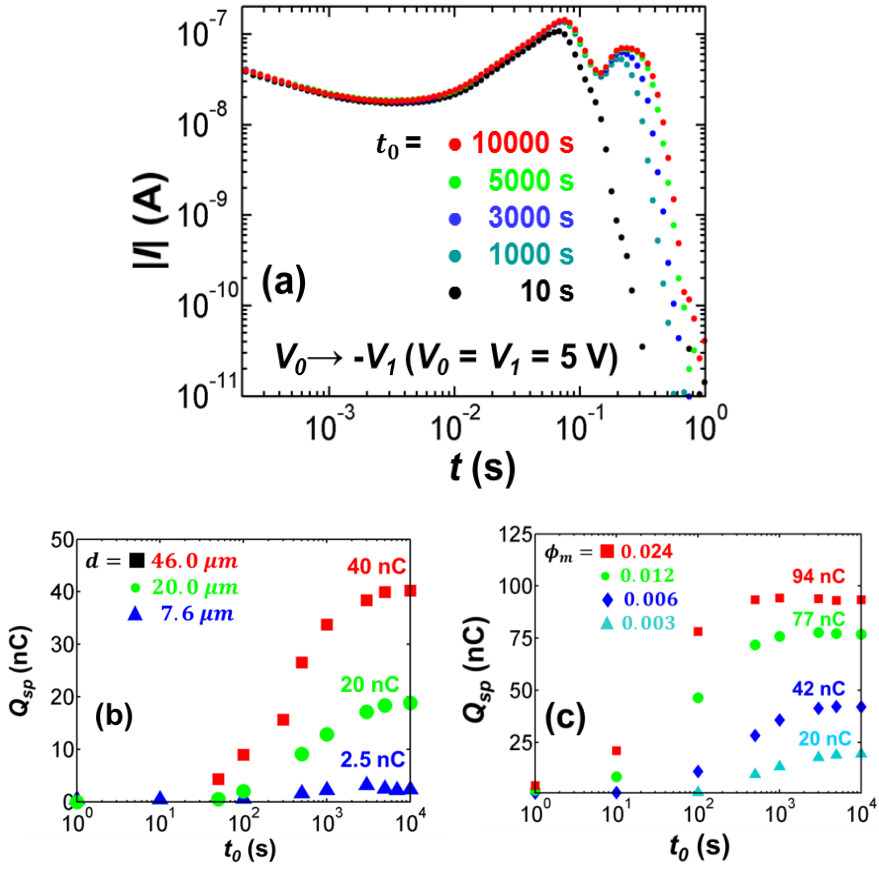

Figure 5.2: Reversal current measurement of type A for OLOA 11K in dodecane. (a) Reverse transient current for different durations t_0 of the polarization pulse for a device with d = 20 μm and ϕ_m = 0.003. (b) Integral of the second peak Q_{sp} on a semilogarithmic scale as a function of the duration of the polarizing voltage pulse, for different cell thicknesses d, with ϕ_m = 0.003. (c) Integral of the second peak Q_{sp} on a semilogarithmic scale as a function of the duration of the polarizing voltage pulse for different mass fraction ϕ_m for a device with d = 20 μm. The black lines show a linear fit with the experimental data.

The effect of repeatedly switching the voltage V_1 (type B) on the reversal current and on the second peak is shown in Fig. 5.3 (a , b & c) with $t_0 = t_1$ = 100 s. The peak is observed for voltages larger than 0.5 V (Fig. 5.3 (a)) and the integral of the peak increases approximately linearly with increasing number of voltage cycles until reaching a saturation level as shown in Fig. 5.3 (c). For the voltages larger than 1 V, the integral of the peak is independent of the magnitude of the voltage steps.

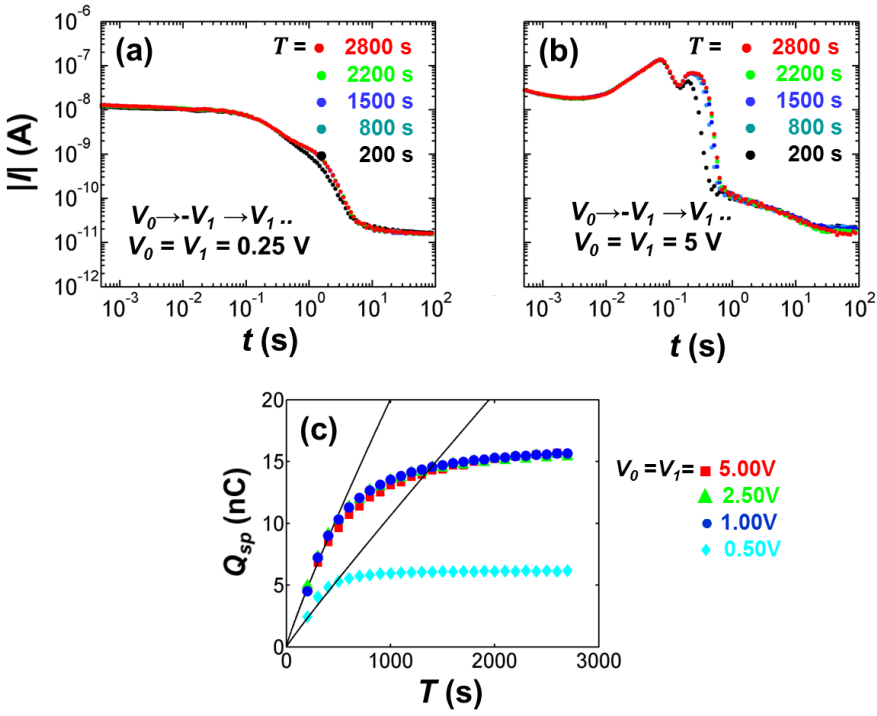

Figure 5.3: Results of experiment type B showing the effects of the magnitude and duration of the oscillating voltage on the integral of the second peak. The experiments are performed in a device with d = 21 µm filled with ϕ_m = 0.003 of OLOA 11K in dodecane. In (a), for small voltages (V_0 & V_1 < 1V), the peak does not appear. In (b), for large voltages (V_0 & V_1 > 1 V) the contribution due to generated charges increases with increasing number of voltage cycles, therefore an increasing peak is observed until it reaches a saturation level. In (c), the integral of the second peak increases linearly (black lines) with increasing number of voltage cycles and the saturation level/linear trend line of the integral is independent of the magnitude of the applied voltage (V_0 & V_1 > 1 V). T is the total duration for which the oscillating voltage is applied.

In chapter 4, it has been shown that the generated charge during the quasi steady state of a polarizing voltage step (V_0 > 1 V) due to the disproportionation mechanism scales as $Q_g = \beta n_o^2 edSt_0$ [23]. Fig. 5.2 (b) shows that the integral of the second peak Q_{sp} is also roughly linear with the duration of the polarizing voltage step t_0, as shown by the black lines in Fig. 5.2 (a) & (b). The saturated integral of the second peak also scales proportionally with the cell thickness d (for d > 10 µm) as $\left(8.8 \times 10^{-4} \frac{\mathrm{C}}{m}\right) \times d$. The increase in the saturated integral of the second peak with

increasing device thickness indicates that the second current peak is directly related to the generation of new charges in the bulk. Fig. 5.2 (c) shows that the saturation level Q_{sp} scales linearly with ϕ_m with trend line: 6540 nC $\times \phi_m$, for $\phi_m \leq 0.012$ (and not quadratically like Q_g, as will be discussed in section 5.4.1). Therefore, overall the saturation level of the integral of the second peak scales proportionally with the cell thickness and with ϕ_m (for $\phi_m \leq 0.012$) as $\left(0.34 \frac{\mathrm{C}}{m}\right) \times \phi_m d$. For the concentration ϕ_m= 0.003, the maximum integral of the second peak Q_{sp} = 20 nC is approximately 6.7 % of the charge Q_g = 300 nC generated during a polarizing voltage step of 10000 s.

Since at low voltages screening of the electric field limits the amount of charges that reach the electrodes, the interface layer is not getting filled with newly generated charges and the second peak is absent in Fig. 5.3 (a). While for V_0 > 1 V & $|V_1|$ > 1 V, the electric field does not become screened. Therefore, all the generated charges during the quasi steady state reach the electrodes and the interface layer is filled completely Since the generation of new CIMs is due to the Brownian collision (depend only on temperature and independent of the voltage) of neutral IMs, the saturated integral (Q_{sp}) of the second peak in Fig. 5.3 (c) is independent of the magnitude of the applied voltage when V_0 & $|V_1|$ >1 V. For low ϕ_m and small cell thicknesses a longer polarization duration (t_0) is required to obtain a similar magnitude of the second current peak. In chapter 4, section 4.4.1, it has already been shown that the quasi steady state currents are limited by the bulk generation mechanism and the surface generation does not play any significant role [58]. This leads to the conclusion that the second peak is related to the generation of new charges in the bulk. Note that the integral of the saturated second peak is less than 7 % of the total charge which is generated during a polarizing voltage step of 10000 s. This will be further discussed in section 5.4.1.

From the above presented results and discussion, it can be safely concluded that the second peak is due to the CIMs that are generated in the bulk during a long duration polarizing voltage step. Now the question arises, why does the release of generated CIMs result in the second peak? In order to find an answer this question and to understand the physical nature of the generated CIMs, two additional experiments were performed named as type C & D. In the type C, the effect of the short circuit duration on the second peak is

investigated while in the type D, the effect of replacing the bulk by pure dodecane just after a long duration polarizing voltage step is studied. The results of the type C & D experiments are shown in the next section.

5.3.2 Comparison Between the Results of Type C and D Experiments

A comparison of the transient current $|I|$ for the voltage step $0 \rightarrow V_2$ in the experiments of type C (for V_2 = 5 V or -5 V, t_{s1} = 3 s or 30 s and V_0 = 5 V, t_0 = 10000 s) and type D (for V_0 = 5 V, t_0 = 10 s to 10000 s and V_3 = 5 V, t_3 = 20 s) is shown in Fig. 5.4 (a & b).

The first part of the type C currents up to t = 0.1 s in Fig. 5.4 (a) is roughly the same for all t_0 and corresponds to drift and diffusion of positive and negative CIMs that diffused back to the bulk when the device was short circuited for a duration ts1 after the polarizing voltage step [77]. The current peak between 0.1 s and 1 s has a different nature. This peak is apparently linked to the previous generation of new charges, because its amplitude increases with increasing duration t_0 of the polarizing voltage step (it is absent for t_0 < 100 s and saturates for t_0 > 3000 s) and increasing thickness of the device (see Fig. 5.2 (c)). The peak in Fig. 5.4 (a) also depends on the duration of the relaxation time ts1 and on the sign of the applied voltage: for short values of the relaxation time (t_{s1} = 3 s) the peak appears only for V_2 = -5 V (Q = 20 nC,) i.e. when the polarity of V_2 is opposite to that of V_0. When the device is short circuited for a longer time t_{s1} = 30 s the peaks are similar for both polarities of the voltage, i.e, V_2 = 5 or –5 V. This phenomenon will be explained in section 5.3.5.

The currents in the type D experiment are shown in Fig. 5.4 (b). The initial current is much lower and instead of a second peak, a more or less constant current between 0.03 s and 0.5 s with a magnitude of about 10 nA (much higher than the current in pure dodecane of 1 pA) is observed. The typical drift and diffusion current observed for regular CIMs has disappeared because the cleaning procedure has taken away all the regular CIMs in the bulk of the device. Since the duration of the plateau in the current increases with increasing duration of the polarizing voltage step and the level of the constant currents is very low when the duration of the polarizing voltage step was very small. From this it can be concluded that the plateau current is a

consequence of the newly generated charges. The CIMs which result in the second peak (in the type A & B experiments) or the peak (in the type C experiment) and the constant current (in the type D experiment) are in the next referred to as "special CIMs" or SCIMs. Further discussion of the results of the experiments type C & D is provided in section 5.3.5.

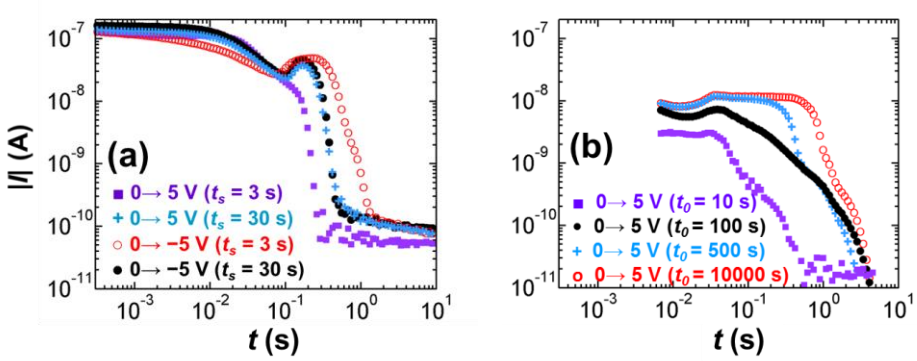

Figure 5.4: Transient current measurements ($|I|$) in response to a voltage step $0 \rightarrow \pm V_{2,3}$ ($V_{2,3}$ = 5 V) performed in the device with d = 20 µm filled with a surfactant mixture of ϕ_m = 0.003. In (a) the results of the experiment of type C show the effect of the relaxation time (t_{s1}) on the current peak while in (b) the results of the experiment of type D show the effect of the polarizing voltage step duration (t_0) on the duration of the plateau current between 0.03 and 1s for $t_0 \geq$ 500s.

5.3.3 Release of SCIMs

In order to study the behavior of the SCIMs in more detail, the type D experiment is repeated for different applied voltages and voltage sequences. The results are shown in Fig. 5.5. For voltages V_3 between 0.5 V and 15 V the current in Fig. 5.5 remains approximately constant for a certain duration and then quickly drops to zero. The amplitude of this approximately constant part of the current fits well with the Mott-Gurney equation $I = 9\varepsilon_0\varepsilon_r\mu S V_3^2 / (8d^3)$ [103–106]. This equation, which will be discussed in more detail in chapter 6, describes a space charge limited current in which charge carriers are released from only one interface where the field is clamped to zero [103,106]. The field stays zero at the electrode because when charges are released, the resulting space-charge reduces the field at the electrode, which in turn reduces the release of charges. In this feedback-mechanism, the charges themselves are limiting the rate at which they are released [99].

The calculated currents fit with the measured currents when the same value of the mobility is used as for regular CIMs of OLOA 11K in dodecane, *i.e.*, μ = 1320 μm^2/Vs. In chapter 4 section 4.4.2, it has already been shown that the mobility of generated CIMs is equal to that of regular CIMs [58]. Now it can also be concluded that the size of SCIMs and regular CIMs is the same. The good fit of the measurements with the Mott-Gurney equation indicates that only one polarity of charge carriers (positive or negative) is contributing to the current, and that the SCIMs are present in an interface layer at the electrode (and not in the bulk) before the voltage step is applied.

The total amount of charge that is transferred during the voltage step 0→V_3 or 0→-V_3 in Fig. 5.5 (a-b) (the integral of the current) is more or less the same for all applied voltages, namely Q^*= 8 nC (or a charge density of 8×10^{-5} C/m² over S = 10^{-4} m^2) and 16 nC for V_3→-V_3. The total charge (16 nC on both electrodes) is a fraction of about 5 % of the integral of the generation current during the polarizing voltage $Q_{gen} \approx$ 300 nC. From the Mott-Gurney expression for the current and the total charge, the time t* after which the current drops to zero is $t^* = 8d^3Q^*/(9\varepsilon_0\varepsilon\mu SV^2)$ (indicated by the vertical lines in Fig. 5.5).

The type D experiment has been repeated but with the application of a negative voltage step (0→-V_3) instead of a positive voltage step (currents shown in Fig. 5.5 (b)) after the cleaning procedure. The measured currents have the opposite polarity, but are otherwise the same as in Fig. 5.5 (a). This indicates that after the cleaning procedure, both electrodes can release the same amount of charged SCIMs. This is in agreement with the fact that the peaks in Fig. 5.4 (a) for the experiment type C (0→V_3 and 0→-V_3) have the same amplitude when the short circuit time is 30 s.

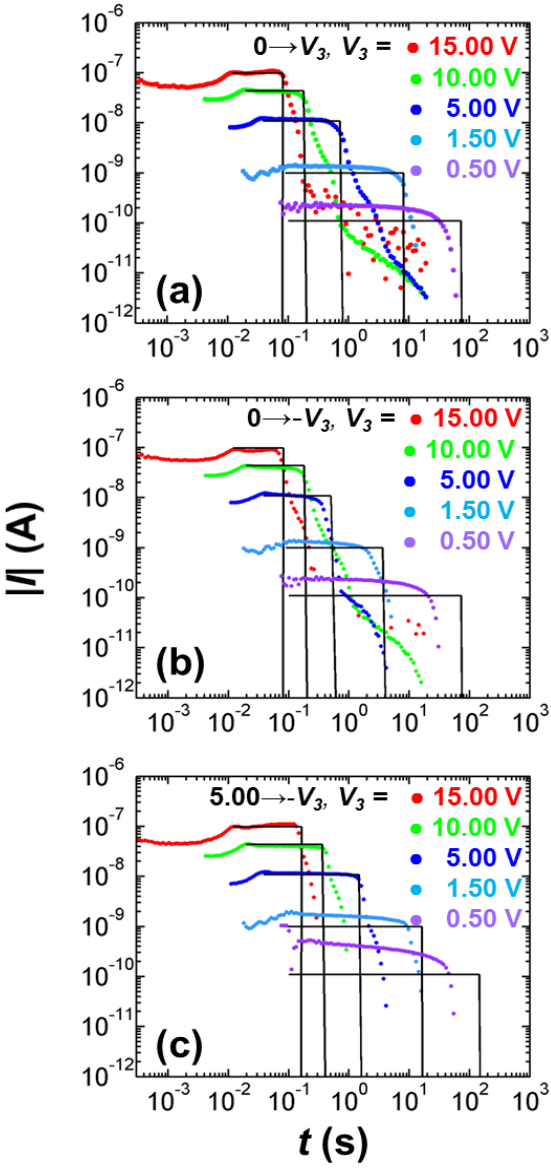

Figure 5.5: A comparison between transient current measurements (color dots) and the currents calculated from the Mott-Gurney equation (black lines) for the type D experiment (d = 20 μm filled with ϕ_m = 0.003 for 0→V_0). (a) In response to the voltage step 0→V_3. (b) For 0→-V_3 and (c) for 5 V→-V_3. The measured currents are in agreement with the Mott-Gurney equation up to the time t^* and then decrease rapidly. The fitting parameters are: μ = 1320 μm^2/Vs and N_{SCIMs} = 500 μm^{-2} (Q^*= 8 nC) respectively

To study the behavior of the SCIMs in more detail, a reverse step $V_3 \rightarrow -V_3$ is applied after the $0 \rightarrow V_3$ step in the type D experiment. The measured currents are again a Mott-Gurney type of current as shown in Fig. 5.5 (c), but the time t^* and the total charge transfer are a factor two larger. This indicates that the SCIMs, which contribute to the current in the type D experiment, are again participating in the interface layer and contribute to the current during the next step. In Fig. 5.5 (c), for smaller voltages the measured currents are larger than those predicted by the Mott-Gurney equation. This could be due to incomplete adsorption of the SCIMs in the interface layer during the voltage step $0 \rightarrow V_3$.

5.3.4 The Polarity of the Released SCIMs

To investigate the polarity of the SCIMs that contribute to the current in Fig. 5.5 and to the second current peak in Fig. 5.4 (a), experiment type D is performed with the following additional step: after the extraction/refilling procedure of the type D experiment, one substrate is replaced by a clean substrate (in this case the two substrates were not glued together). In the following, the electrode that was replaced is always considered the reference electrode, and the voltages refer to the potential at the electrode that was not replaced. Fig. 5.6 shows the measured currents $|I|$ for a voltage step $0 \rightarrow V_3$ with V_3 = +5 V or V_3 = -5 V for a duration of 5 s. When the voltage is positive ($0 \rightarrow 5$ V) no significant current is measured in Fig. 5.6. Even for a very large positive voltage (V_3 =100 V) the current remains low. This indicates that there are no positive SCIMs at the electrode of the unchanged substrate, and, as expected, no negative SCIMs at the electrode of the replaced substrate. When a negative voltage V_3 is applied ($0 \rightarrow -5$ V), a significantly higher current is observed. The current in Fig 5.6 is slightly lower than the current in Fig. 5.5 for the same voltage and does not have a constant level. This difference is ascribed to the release of some SCIMs from the unchanged substrate during the replacement of the other substrate. Fig. 5.6 indicates that only the negative generated CIMS or SCIMs are released from the interface layer when a voltage is applied and are responsible for the Mott-Gurney space charge limited current observed in Fig. 5.5.

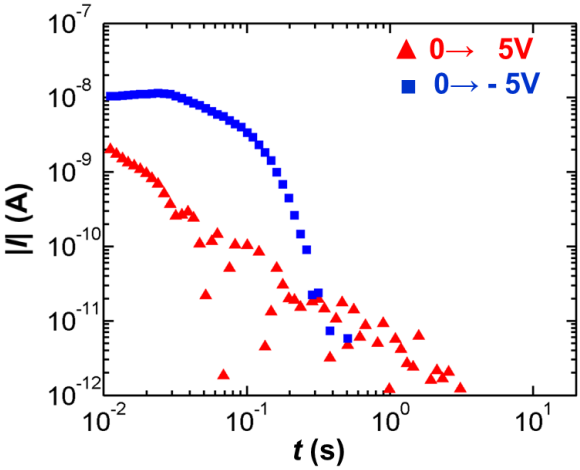

Figure 5.6: Measured currents of the polarizing voltage step $0 \rightarrow V_0$ in the case that one substrate has been replaced, for a cell with d = 20 µm filled with ϕ_m = 0.003. There is only a significant current when the applied voltage step is negative.

5.3.5 Different Types of CIMs

Fig. 5.7 (A) depicts the various steps of an experiment which is the combination of experiment types C and D. Fig. 5.7 (B) illustrates the outcome during each step of the experiment and shows how the different types of CIMs contribute to the current. Initially there are only uncharged inverse micelles (not shown) and regular CIMs (Fig. 5.7 (B (a))) in the mixture. During the 10000 s polarizing voltage step (Fig. 5.7 (B ((b))) new CIMs are generated and they travel to the electrodes with the opposite polarity. Most of them (300 nC positive CIMs and -284 nC negative CIMs: not shown in the interface layers in Fig. 5.7 (B (c-d))) join the interface layer and are never released. A small fraction of the negative charges (-16 nC) are SCIMs that get adsorbed in the interface layer and are released again when

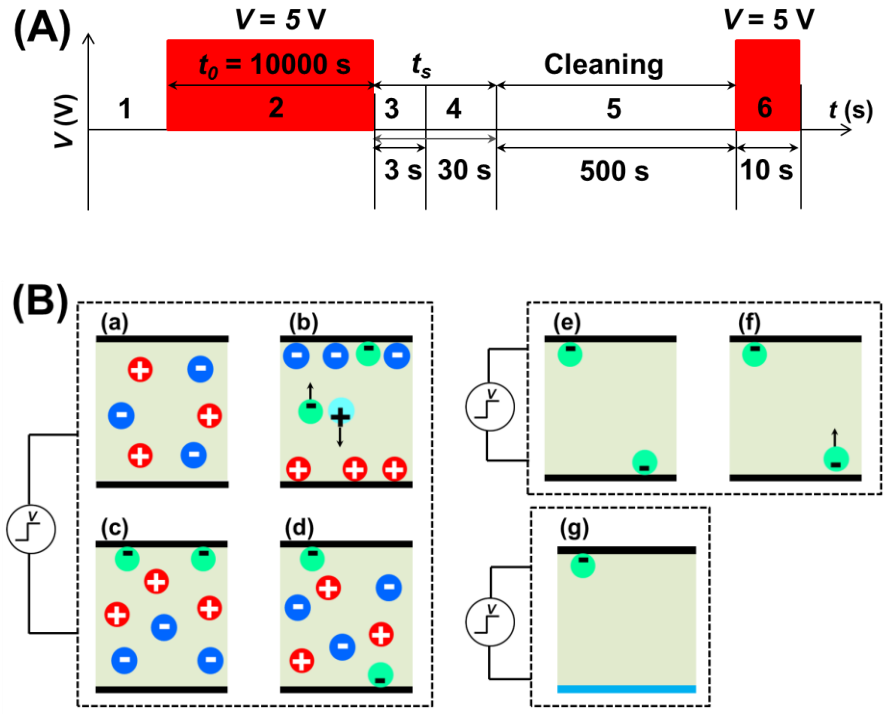

Figure 5.7: In (A) various steps (1-6) of the experiment are depicted. In (B) the outcome of each step (a-g) of the experiment is illustrated with the location and motion of regular CIMs (blue and red circles) and generated CIMs (green and cyan circles) (a): initial situation (only regular CIMs), (b): polarizing step, (c): after short circuit of t_s = 3 s, (d): after short circuit of t_s = 30 s, (e): after removing the regular and neutral CIMs (type B), (f): voltage step after cleaning, (g): after replacing the bottom substrate. In (B (b-g)), the generated positive SCIMs are not shown because they never release from the electrode.

the field near the negative electrode changes sign. When the device is short circuited (Fig. 5.7 (B (c))) the regular CIMs move immediately into the bulk due to drift and diffusion, but the negative SCIMs only gradually release from the electrode. For a small short circuit time t_{s1} = 3 s, most of them are still in the interface layer. After 30 s of short-circuit duration, the negative SCIMs have redistributed in such a way that equal amounts are present at both electrodes (Fig. 5.7 (B (d))). This explains why the peak that is observed in Fig. 5.4 (a) in the experiment type C and for which the SCIMs are responsible, depends on the short circuit time. After the cleaning procedure is carried out, all regular CIMs and uncharged inverse micelles

have disappeared (Fig. 5.6 B (e))). When a positive voltage step is applied as in Fig. 5.5 (B (f)), the SCIMs move to the other side. When the bottom surface is replaced, only one surface contains SCIMs (Fig. 5.6 (g)), which explains the asymmetry in Fig. 5.5.

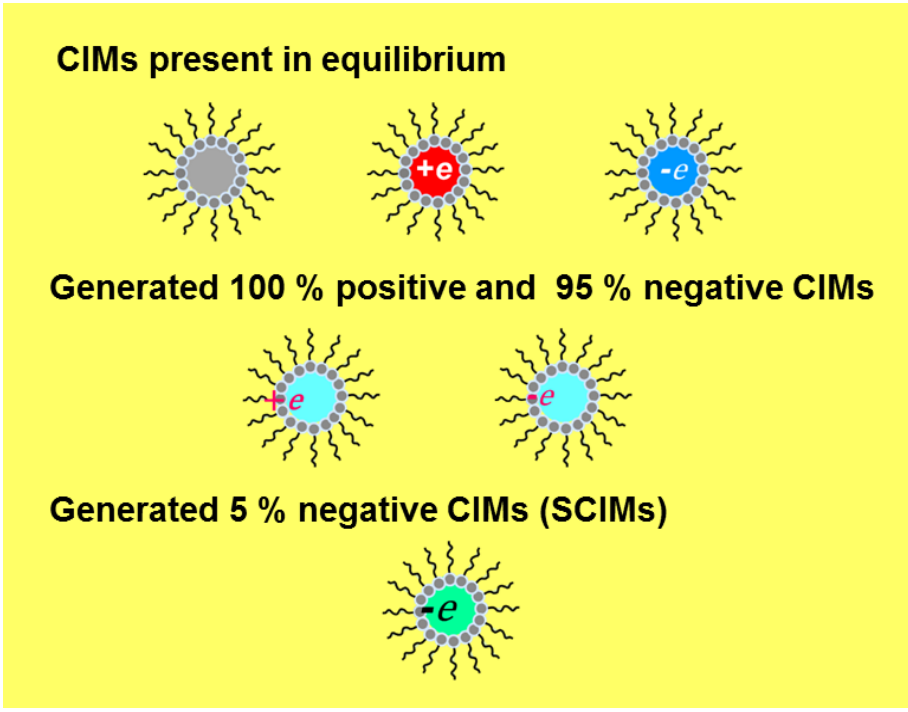

Figure 5.8: Schematic illustration of the six different types of charged and neutral IMs. The main physical difference between CIMs is the location of the charge. The generated CIM in which the charge is very close to the outside (100 % of the positive and 95 % of the negative generated CIMs) are attracted strongly by the electrodes and are never released. The CIMs in which the charge is more towards the center (5 % of the generated negative CIMS) or in the center (regular CIMs) are released when the voltage is reversed or switched off.

The experiments indicate that the newly generated CIMs stick at the electrodes in the interface layers whereas the regular CIMs form a diffuse double layer. Let us discuss the origin of this different behavior at the interfaces. It was already known that both kinds of CIMs have the same mobility and (as their charge is $+e$ or $-e$ [72,73]) are therefore equal in size. However, the difference in behavior might be explained by the location of the charge in the charged inverse micelle. If the charge is positioned in the center of the inverse micelle (with r = 5.5 nm for PIBS [15,62,74]), the

electrostatic force between the charged inverse micelle and its image charge in the electrode is low which could explain why the regular CIMs do not stick electrostatically to the surface. If on the other hand the electrical charge is positioned closer to the edge of the CIMs as depicted in Fig. 5.8, the electrostatic attraction to the image charge in the electrode can be much stronger and the CIMs can be adsorbed strongly at the electrode interface. This phenomenon is also observed in the case of small micelles like AOT in dodecane (r = 1.6 nm [12,17]) which always form a permanently sticking layer at the interface when a voltage is applied [13,74,76]. Therefore, it can be hypothesized that most newly generated CIMs have their charge near the surface of the micelle. When they reach the electrode, the attractive force is so strong that they are never released. Only for a small fraction of generated negative CIMs (SCIMs) the charge is at some intermediate position between the edge and the center of the micelle, so that these SCIMs can be released when the sign of the field is reversed. The view emerges that different types of CIMs can be generated, with their charge at various positions in the interior or at the outside of the micelle. In the absence of a field, CIMs with a charge at the outside either quickly recombine or the charge gets stabilized internally so that they become regular CIMs. Therefore, in equilibrium in good approximation only regular CIMs are present. In the presence of a field, the situation is different. When positive and negative CIMs are formed in the presence of a field, they are immediately separated, preventing recombination, and their charges can remain at the periphery of the micelle because of the continuous force acting on the charge which prevents stabilization inside the micelle.

The experiments indicate that most of the newly generated CIMs (all of the positive ones and 95 % of the negative ones) travel to the electrode with opposite polarity and are never released. It is not clear whether they remain charged at the interfaces or transfer their charge to the electrode and become neutral. From the experimental results, six different types of inverse micelles can be distinguished in the system: the uncharged inverse micelles, the regular CIMs (positive and negative) that form a diffuse double layer when a field is present, the SCIMs, which are negative, participate in the interface layer and are released when the field changes sign and finally the positive and negative CIMs which are created by generation, contribute to the interface layer but are never released from the electrodes.

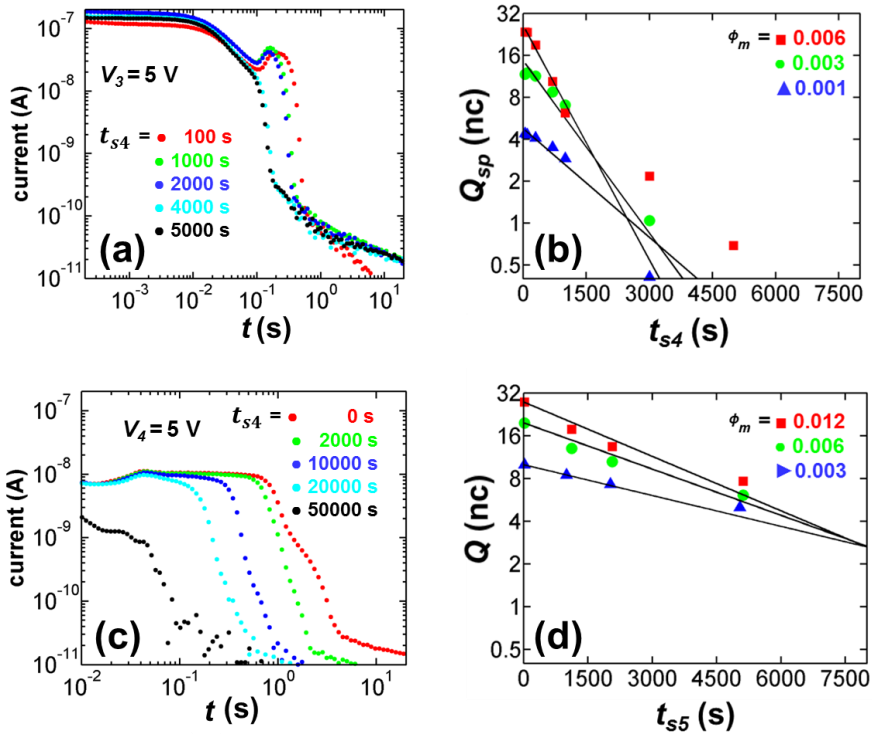

Figure 5.9: Results of the experiment types E (a & b) and F (c & d), which show the decay of SCIMs generated during a polarizing voltage step ($0 \rightarrow V_0$) of 10000 s in a device with d = 20 µm and filled with OLOA 11K in dodecane. In (a), the decreasing peak as a function of the short circuit duration t_{s4} shows the decrease of SCIMs over time in the presence of regular CIMs and neutral inverse micelles for $\phi_m = 0.003$. In (b), the integral of the peak is plotted on a semilogorithmic scale (color symbols) as a function of the short circuit duration t_{s4} and fitted with an exponent (black lines). In (c), the decreasing currents with increasing short circuit time t_{s5} represent how the number of SCIMs decreases over time for the experiment type F. In (d), the decreasing integral of the currents from (c) (color symbols) are shown on a semilogorithimic scale, and fitted with an exponential (black lines), revealing a slower decrease in numbers of SCIMs.

5.3.6 Effect of the Short Circuit Duration on the Concentration of SCIMs

In the following section, the long term decrease of of SCIMs which are generated during a polarizing voltage step ($0 \rightarrow V_0$, V_0 = 5 V) of duration t_0 = 10000 s is studied. Two types of experiments were performed. In the first experiment (Type E), the influence of a long short circuit time t_{s4} on the transient current is investigated. Fig. 5.9 (a) shows the transient currents for a device with d = 20 μm filled with ϕ_m= 0.003 OLOA 11K in dodecane for five different short circuit times. It is clear that the current peak due to the release of SCIMs strongly decreases when the short circuit time is extended over several 1000 s. The current (until the peak) due to regular CIMs is unaffected by the short circuit time. To obtain a value for the decay time of the SCIMs in the interface layer, the integral of second peak Q_{sp} is plotted as a function of the short circuit time t_{s4} in Fig. 5.9 (b) on a semilogarithmic scale. The decay is roughly exponential with an average decay time of 1000 s. The experiment has been repeated for ϕ_m= 0.001, 0.003 and 0.006 and the values of Q_{sp} have also been plotted in Fig. 5.8 (b). The decay times are 1700 s, 1000 s and 700 s respectively.

By using the cleaning procedure before applying the long short circuit time, it can be investigated if the uncharged inverse micelles or CIMs in the bulk play a role in the decrease of the SCIMs in the interface layer (Type F). This means that the experiment of type F is carried out with variable duration of the short circuit time. The transient currents are shown in Fig. 5.9 (c). First of all, the transient currents behave as in the case of field clamping: the current increases to a stationary value and then decreases abruptly to zero (as in Fig. 5.5). This indicates that after cleaning and the long short circuit time there are SCIMs in the interface layer and no CIMs in the bulk of the layer. It can be noticed that the total charge of SCIMs that is released decreases with increasing short circuit time. The integral is shown in Fig. 5.9 (d). The average decay time is about 7000 s. The fact that this decay time is much longer than in Fig. 5.9 (c) indicates that either the CIMs or the neutral inverse micelles play a role in the decrease of the SCIMs in the interface layer.

5.4 Further Discussion

5.4.1 Why does the Integral of the Second Peak Saturate?

From the results shown in Fig. 5.2 and 5.3, it is clear that the second peak in the reversal currents is a result of the new charges generated in the bulk during a continuous polarizing voltage step ($0 \rightarrow V_0$). However, only a small fraction (5 %) of the generated negative CIMs (SCIMs) is released when the voltage is reversed and the integral of the second peak saturates after a certain duration of the polarizing voltage step. The maximum charge which can be accommodated on the electrode's surface (1 cm^2) in the form of a monolayer of the generated CIMs is: $f_c eS/(\pi r^2)$ = 153 nC (r = 5.5 nm is the radius of SCIMs), f_c = 0.91 is the maximum possible circular packing density in a 2D plane [107]. From this, the time by which the area of the electrode is covered completely by the generated CIMs can be calculated as: t_{fm} = (153 nC)/I_g, with I_g the level of the generation current. For a device with ϕ_m = 0.003, d = 20 μm and S = 1 cm^2, the level of the generation current is I_g = 0.03 nA, resulting in t_{fm} = 5100 s which is close to the time of 7000 s by which the integral of the peak saturates (see Fig 5.2 (c)). Since the generation current scales as $I_g \propto {\phi_m}^2$ [23,58], the duration of the polarizing voltage step required to saturate the integral of the second peak should scale as: $t_{fm} \propto \frac{153\ \text{nC}}{\phi_m^2}$. However, for increasing ϕ_m, the relative difference between the calculated values of t_{fm} and those obtained from the experiments (Fig. 5.2 (c)) is increasing, e.g., for ϕ_m = 0.006, the calculated and experimental values of t_{fm} are 1400 s and 3000 s respectively, similarly, for $\phi_m = 0.012$, the values are 300 s and 1000 s. This difference in the values of t_{fm} can be a consequence of faradaic reaction (due to which some generated CIMs lose their charge at the electrode) or due to other phenomena, which are not taken into account while calculating the values of t_{fm}. Another possibility is that the integral of the peak saturates when a dynamic equilibrium is reached between the generation and faradaic reactions occurring at the electrode. The existence of multiple layers of generated CIMs at the interface can also not be ruled out.

5.4.2 Reduced Decay Constant of SCIMs in the Absence of Regular CIMs and Neutral IMs

The reduced decay constant of the SCIMs for the case when the bulk was replaced with pure dodecane (Type F) indicates that the presence of regular CIMs and neutral IMs is assisting in the decrease of SCIMs in some way. For example, the SCIMs which are in the interface layer could be "knocked out" and released into the bulk due to collisions with regular CIMs and neutral IMs. Because of these processes, there are a number of possibilities: the SCIMs can leave their charge at the surface and can be released into the bulk as neutral IMs or they can be released as a SCIM and in the bulk recombine with a positive regular CIM. Since the concentration of the regular CIMs always remains constant in the system, the latter possibility is less likely.

Another possibility is that after releasing from one of the electrodes, they can travel all the distance between the electrodes and reach the other electrode where they can recombine with the generated positive CIMs that are situated in a very thin interface layer. According to this hypothesis, a quicker decrease of the SCIMs which are in the interface layer with the generated positive CIMs (situated at the other electrode which was negatively polarized during the voltage step $0 \rightarrow V_0$) is expected. However, the decrease of the SCIMs is found to be independent of the polarity of the voltages ($0 \rightarrow V_0$ and $0 \rightarrow \pm V_3$ or $0 \rightarrow \pm V_4$), which rules out this hypothesis. The most likely possibility is that due to the collisions of regular CIMs, neutral IMs or due to self-energy, the SCIMs are knocked out of the interface layer leaving their charges at the electrodes. For the case when the bulk was not replaced with dodecane (Type E), the presence of the regular CIMs and neutral IMs increases the chance of SCIMs being knocked out from the interface layer as neutral micelles. Therefore, a quicker decrease of SCIMs is observed. However, for the case in which the bulk was replaced with pure dodecane (Type F), the chance of SCIMs being knocked out is reduced and is limited by the thermal energy of SCIMs, resulting in a comparatively slow decrease of SCIMs.

5.5 Conclusions

The second peak in the reverse transient currents is a consequence of new charges that are generated during a continuous long polarizing voltage step. These generated CIMs do not populate the diffuse double layer but instead end up in interface layers. When the applied voltage is reversed or switched off, a small fraction of the generated negative CIMs is released from the interface layer, which results in a second peak in the current. The formation of the interface layers indicates that different variants of charge exist in the system. From the analysis of the differences in the electrical behavior of CIMs at the interfaces six different types of inverse micelles have been identified. During the release of special CIMs (SCIMs) the field at the electrodes is clamped to zero and the currents match with the Mott-Gurney equation. The presence of the regular and neutral IMs speed up the long term decrease of the SCIMs.

Chapter 6

Release of the Adsorbed Generated Charged Inverse Micelles

Charged inverse micelles generated during a continuous voltage step end up in the interface layers and a small fraction is released when the applied voltage is reversed or switched off. In this chapter the release mechanism of these generated CIMs is modeled. The detailed analysis of the release of generated CIMs with simulations forms an important step in the understanding of the electrodynamics of CIMs in non-polar liquids.

6.1 Introduction

The dominant transport and generation mechanisms of charges in various non-polar surfactant systems have been studied in great detail over the last decades [6,20,76,79]. Transient currents can be explained well on the basis of the Poisson-Nernst-Planck equations in combination with bulk and/or surface generation mechanisms [23,58]. However, the occurrence of an observed so-called ‘second peak’ in surfactant systems such as OLOA 11K in dodecane is a long-standing problem [58,77].

A number of studies have been carried out to understand the origin and mechanism of this second peak (see Chapters 4 and 5). Chapter 5 demonstrates that newly generated CIMs during a long polarizing voltage are building up interface layers, from which some negative charges can be released when the voltage is reversed or switched off [75]. More precisely, in the case where after a polarizing voltage the bulk liquid is replaced by pure dodecane, the agreement of subsequent measured polarization currents with the Mott-Gurney model for space-charge-limited release of one type of charge already gives a good indication of the physical release mechanism [75]. Chapter 4 shows that the mobility and hence the hydrodynamic size of these newly generated CIMs is identical to the regular CIMs, leading to the conclusion that the geometrical position of the charge and the presence of an electric field may play an important role in the behavior of a charged inverse micelle [58].

On the basis of these insights, in this chapter, a full 1D simulation model is developed to calculate the release of SCIMs in detail and to compare the results of the model with experiments performed in various situations. The presented model explains the measured currents well, with some additional effects such as electrohydrodynamic flows.

6.2 Theoretical Model

In this section, the model that was presented in chapter 5 is extended to a full simulation, including the bulk generation of various types of CIMs having different behavior when they reach the electrodes and different release conditions when the field is reversed. Then, analytical formulas are derived for the case that the bulk is deprived of regular CIMs and neutral inverse micelles (IMs) and implement space charge limited release of SCIMs from the interface layer.

6.2.1 Simulation Model

Let us consider the case in which the space between two parallel electrodes, separated at a distance *d*, is filled with a mixture of nonpolar liquid and surfactant. In thermal equilibrium and in the absence of an electric field, a small fraction of inverse micelles is charged with an equilibrium concentration: $\bar{n} = n_+ = n_- = \sqrt{K}\,\bar{n}_0$ [23,58]. When a voltage difference is applied across the electrodes, drift and diffusion of these regular CIMs

results in a flux: $\Psi_{\pm} = \pm n_{\pm}\mu E - D\frac{\partial n_{\pm}}{\partial x}$. Since z = 1, it is assumed that positively and negatively charged inverse micelles have the same size and the same mobility (but opposite charge) [72,73].

Three types of additional CIMs are generated in the bulk in the presence of an electric field as the result of bulk disproportionation. For each generation event on average the following CIMs are generated out of the collision between two uncharged inverse micelles: 1 positive and 0.95 negative CIMs that will stick to the interface layer and are never released again, and 0.05 special negative CIMs or SCIMs that can be released from the interface layer. The concentrations of these three types of CIMs are described by n_{s+}, n_{s-} and n_{SCIMs}. The mobility, valency (z = 1) and diffusion constant of these CIMs are the same as that of the regular CIMs. For each of them a flux can be defined in the bulk: Ψ_{s+}, Ψ_{s-} and Ψ_{SCIMs} containing similar drift and diffusion terms as $\Psi_{\pm}$. The low generation rate constant β (order 10^{-24} m^3/s [23,58]) for OLOA 11K in dodecane leads to the conclusion that the concentration of the neutral inverse micelles n_0 remains approximately equal to the original value $\bar{n}_0$.

In this model any field dependency of the generation/ recombination rate constants of CIMs is ignored and the above-mentioned proportions 100 %, 95 % and 5 % in which the various CIMs are generated in the presence of an electric field [75]. The continuity equations for the different types of CIMs can be written as:

$$\frac{\partial n_{\pm}}{\partial t} = -\frac{\partial}{\partial x}(\Psi_{\pm}) \tag{6.1}$$

$$\frac{\partial n_{s+}}{\partial t} = -\frac{\partial}{\partial x}(\Psi_{s+}) + \beta n_0^2 \tag{6.2}$$

$$\frac{\partial n_{s-}}{\partial t} = -\frac{\partial}{\partial x}(\Psi_{s-}) + 0.95\beta n_0^2 \tag{6.3}$$

$$\frac{\partial n_{SCIMs}}{\partial t} = -\frac{\partial}{\partial x}(\Psi_{SCIMs}) + 0.05\beta n_0^2 \tag{6.4}$$

The electric field between the electrodes is governed by Gauss's equation:

$$\varepsilon_o \varepsilon_r \frac{\partial E}{\partial x} = \rho \tag{6.5}$$

In this equation, $\rho = e(n_+ - n_- + n_{s+} - n_{s-} - n_{SCIMs})$ is the charge density. The current is calculated as [6,58,72]:

$$I(t) = (eS/d) \int_0^d (\Psi_+ - \Psi_- + \Psi_{s+} - \Psi_{s-} - \Psi_{SCIMs})\, dx \tag{6.6}$$

6.2.1.1 Initial Conditions

Initially, at t = 0 s, when the device is in equilibrium, the regular CIMs are uniformly distributed and it is assumed that the concentration of generated CIMs is zero. Thus, the initial conditions at t = 0 s are given by:

$$n_+ = n_- = \bar{n} \tag{6.7}$$

$$n_{s+} = n_{s-} = n_{SCIMs} = 0 \tag{6.8}$$

6.2.1.2 Boundary Conditions

Let us now discuss the boundaries conditions. Regular CIMs form a double layer in the bulk. For the regular CIMs there is no flux into the interface layer and blocking boundaries conditions are used:

$$\Psi_\pm (x = \Delta) = \Psi_\pm (x = d - \Delta) = 0 \tag{6.9}$$

The different types of generated CIMs ($n_{s\pm}$ and n_{SCIMs}) are adsorbed at the surface in the interface layer with thickness Δ. Previous studies [77] show that the distance between the charges in the interface layer and the interface ($\alpha.\Delta$ with $\alpha < 1$ a constant which determines the distance of the SCIMs from the electrode) is so small, that the charges do not affect the electric field in the bulk significantly, and therefore it is set $\Delta << 1$ nm. The majority of generated CIMs stick to the boundary when they reach the interface layer at $x = \Delta$ or $x = d - \Delta$, therefore their concentration is zero (here, surface charge density is considered as a separate variable) at the corresponding locations:

$$n_{s\pm}(x = \Delta) = n_{s\pm}(x = d - \Delta) = 0 \tag{6.10}$$

For the negative SCIMs two cases are considered. The first case when the electric field in the bulk near the interface layer is pointing away from the interface. In this case the SCIMs are adsorbed in the interface layer, just like the other generated CIMs (100 % generated positive and 95 % generated negative CIMs), as shown in Fig. 6.1 (a).

$$n_{SCIMs}(x = \Delta) = 0, \text{when } E(x = \Delta) > 0 \tag{6.11}$$

$$n_{SCIMs}(x = d - \Delta) = 0, , \text{when } E(x = \Delta) < 0 \tag{6.12}$$

The flux of SCIMs going into and out of the interface layer is linked to the surface density of SCIMs in the interface layer N_{SCIMs} (/m^2) by the continuity equation:

$$\frac{\partial N_{SCIMs}}{\partial t} = -\Psi_{SCIMs}, (x = \Delta) \tag{6.13}$$

$$\frac{\partial N_{SCIMs}}{\partial t} = \Psi_{SCIMs}(x = d - \Delta) \tag{6.14}$$

When the field in the bulk near the interface layer becomes zero, SCIMs can be released from the interface layer, see Fig. 6.1 (b). Here it is assumed that the release of negative SCIMs is governed by field clamping, which means that as many charges are released as needed to keep the field at $x = \Delta$ (or at $x = d - \Delta$) equal to zero [104,106]. This continues until all the negative charges are released. At that moment the field in the bulk near the interface layer can start to point into the electrode.

Combining Gauss's equation with the continuity equation, it can be shown that $\nabla.(\varepsilon_0\varepsilon_r\frac{\partial E}{\partial t} + J) = 0.\left(\varepsilon_0\varepsilon_r\frac{\partial E}{\partial t} + J\right)$ is therefore independent of the position and equal to current density in the external circuit. For the case of blocking electrodes, there is no incoming or outgoing flux at the electrodes, so $(J)_{x = 0 \text{ or } x = d} = 0$ and the current density in the external circuit is given by $\varepsilon_0\varepsilon_r\left(\frac{\partial E}{\partial t}\right)_{x = 0}$. For space charge limited release of SCIMs from the electrode ($x = \Delta$), the field at that electrode is always zero and $(J)_{x=\Delta}$ is equal to the measured current density in the external circuit. From this the

outgoing flux of SCIMs from the electrode (x = Δ) to the bulk can be calculated as:

$$\Psi_{SCIMs}(x = \Delta) = -\frac{I(t)}{eS}, \text{ as long as } N_{SCIMS}\,(x = \Delta) > 0 \qquad (6.15)$$

The decrease of N_{SCIMs} is found by Eq. 6.13. When the value becomes zero, no more SCIMs can be released:

$$\Psi_{SCIMs}(x = \Delta) = 0, \text{when } N_{SCIMS}\,(x = \Delta) = 0 \qquad (6.16)$$

Similar formulas apply for the release of SCIMs near the x = d interface.

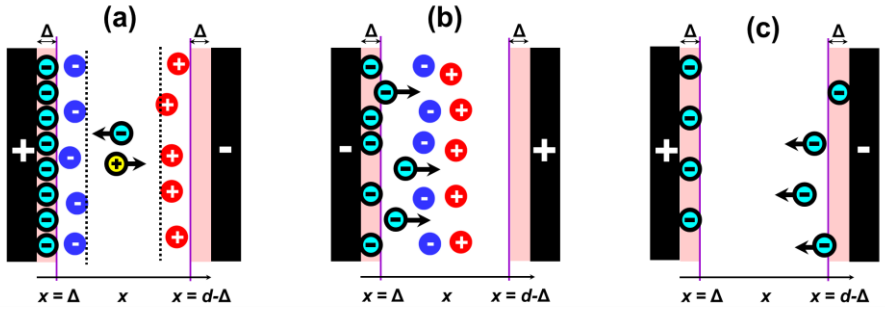

Figure 6.1: Schematic representation of the measurement device with two parallel electrodes separated at a distance d with an overlapping area S = 1 cm^2. The device is filled with a suspension of OLOA 11K in dodecane. The regular CIMs are depicted by red and blue color circles while the generated CIMs are depicted by cyan and yellow color circles. In (a), in response to a polarizing voltage step (0→V_0), the formation of diffuse double layers for the regular CIMs and interface layers for the newly generated CIMs (light magenta color) is illustrated. The SCIMs in the interface layer are shown in cyan, the other adsorbed CIMs are not shown In (b), the release of the regular CIMs and SCIMs is depicted when the voltage is reversed (V_0→-V_1) rapidly after a polarizing voltage step. In (c), intact interface layers with SCIMs are illustrated after cleaning the device.

The set of equations for the CIM fluxes are numerically solved. This involves solving the differential equations 6.1-6.5, using the initial conditions of Eqs. 6.7-6.8 and the boundary conditions of Eqs. 6.9-6.16. The electric currents that are measured in the external circuit are calculated using equation 6.6.

6.2.2 Analytical Equations

In this section analytical formulas are derived for the current for the case when the bulk is deprived of the regular CIMs and neutral IMs (experiment type A) and space-charge-limited release of charges occurs from one interface layer only, as shown in Fig. 6.1 (c). For the case of plane parallel electrodes with capacitance C (F) the charge Q at the electrode is $Q = -CV_1$, where V_1 is the applied voltage. As soon as the voltage is applied at $t = 0$ s, the charge Q is released from the electrode in order to reduce the field to zero at the electrode. Since the field near the electrode is very low, the released charge diffuses as: $X_{diff} = \sqrt{2Dt}$, with X_{diff} is the average displacement from an initial position. From this, the average diffusion speed of the released charge from the surface can be calculated as: $v_{diff} = \frac{\partial X_{diff}}{\partial t} = \sqrt{D/2t}$. The current due to diffusion of a total charge Q is given by:

$$I_s(t) = \frac{Q}{(d/v_{diff})} = \frac{\varepsilon_o \varepsilon_r S V_1}{d^2} \sqrt{\frac{\mu k_B T}{2et}} \tag{6.17}$$

This is a slowly decreasing current as is observed in the simulations during the first millisecond (see Fig. 6.2).

On a longer time scale, a stationary state is reached in which the current density J becomes independent of the position x (as we will see in section 6.4.1) [103–105]. Then, in the absence of diffusion, the current density is given by Eq.6.6:

$$J = n_{SCIMs}(x) e \mu E(x) \tag{6.18}$$

Here, $n_{SCIMs}(x)$ is the concentration of SCIMs at a position x in the bulk. Combining Eq. 6.18 with Gauss's equation (Eq. 6.5) with $\rho = -en_{SCIMs}$, gives:

$$\varepsilon_r \frac{\partial E(x)}{\partial x} = -\frac{J}{\mu E(x)} \tag{6.19}$$

Adjusting and integrating Eq. 6.19 from 0 to *x* using the boundary condition *E* (*d*-Δ) = 0 (see Fig. 6.1 (c)) gives:

$$J = \frac{\mu\varepsilon_o\varepsilon_r E(x)^2}{2(x-d-\Delta)} \tag{6.20}$$

Eq. 6.20 can be written as:

$$E(x) = \sqrt{\frac{2J(x-d-\Delta)}{\mu\varepsilon_o\varepsilon_r}} \tag{6.21}$$

Integrating Eq. 6.21 over the whole thickness yields ($d \gg \Delta$):

$$V_1 = \int_0^d E(x)dx = \int_0^d \sqrt{\frac{2Jx}{\mu\varepsilon_o\varepsilon_r}}\, dx = \sqrt{\left(\frac{8d^3J}{9\varepsilon_o\varepsilon_r\mu}\right)} \tag{6.22}$$

Re-writing Eq. 6.22 we get, for the current:

$$I_{ss} = \frac{9\varepsilon_o\varepsilon_r\mu S{V_1}^2}{8d^3} \tag{6.23}$$

Eq. 6.23 is known as the Mott-Gurney Equation and is used to calculate the plateau value of the currents in the stationary state phase (I_{ss}) of the space charge limited release of charges [103,104,106].

6.3 Experiments

Devices of thicknesses *d* = 20 and 46 µm are made using the same method which has been described in the previous chapters. Solutions are prepared with mass fraction ϕ_m = 0.001 and 0.003 of OLOA 11K in dodecane. The volume between the electrodes is filled with the prepared mixtures. Currents are measured using the same setup which has been described in chapter 2. Before starting a measurement, equilibrium conditions are ensured in the device by short-circuiting the electrodes for 10000 s. Then, two types of experiments are performed that provide some insight in the behavior of generated CIMs.

In the first type of experiment (Type A), the release of SCIMs as a function of the voltage V_1 in the absence of the regular and neutral IMs is studied

using the following experiment sequence. Firstly a polarizing voltage step $0 \rightarrow V_0$ (V_0 = 5V) of a duration t_0 =10000 s is applied and then the device is short-circuited for t_{s1} = 100 s. Subsequently, the space between the electrodes is replaced by air by sucking out the liquid with a suction pump. Then the space is refilled with pure dodecane and emptying/filling is repeated 10 times to ensure complete cleaning of the space. Afterwards, the cell is filled with pure dodecane, the electrodes are re-connected to the measurement setup and a voltage step $0 \rightarrow V_1$ is applied for t_1 = 200 s and the currents are measured. Subsequently, the device is short circuited for a time t_{s2} = 50000 s.

In the Type B experiment, the release mechanism of the SCIMs is studied in the presence of regular and neutral CIMs. The experimental sequence is the following: firstly a polarizing voltage step $0 \rightarrow V_0$ (V_0>>1 V) of t_0 = 10000 s is applied, then the polarity of the voltage is reversed abruptly from V_0 to -V_2 for a duration of t_2 = 200 s and the reversal transient current is measured. Finally the device is short-circuited for a duration of t_s = 10000 s. For another voltage V_2, the same cycle is repeated, which can be summarized as: $0 \rightarrow V_0$ (10000 s) $\rightarrow$ -V_2 (0 to 10 V) $\rightarrow$ 0 V.

6.4 Measurement and Simulation Results

The results of the experiment type A and type B including a comparison with simulations are shown in Fig. 6.2 and Fig. 6.4. The shape of the currents is explained below on the basis of transient variations of the electric field and concentrations of charged inverse micelles in the device.

6.4.1 When the Bulk is Replaced With Pure Dodecane

The results of experiment type A are shown in Fig. 6.2, for which, after a polarizing voltage step, the bulk is replaced with pure dodecane. The simulations are based on space-charge limited release of charges from the interface layer at one of the electrodes. The simulation parameters are the mobility of SCIMs (1320 μm^2/Vs) and charge density of SCIMs (N_{SCIMs}) in the interfacial layers (500 /μm^2 for ϕ_m= 0.003 (Fig. 6.2 (a)) and 1000 /μm^2 for ϕ_m= 0.006 (Fig. 6.2 (b)) at each electrode). The good agreement between the measurements and the simulations confirms that the experimental

currents are space charge limited and that charges are released from only one electrode. Fig. 6.2 (a) and (b) show results for two concentrations ϕ_m= 0.003

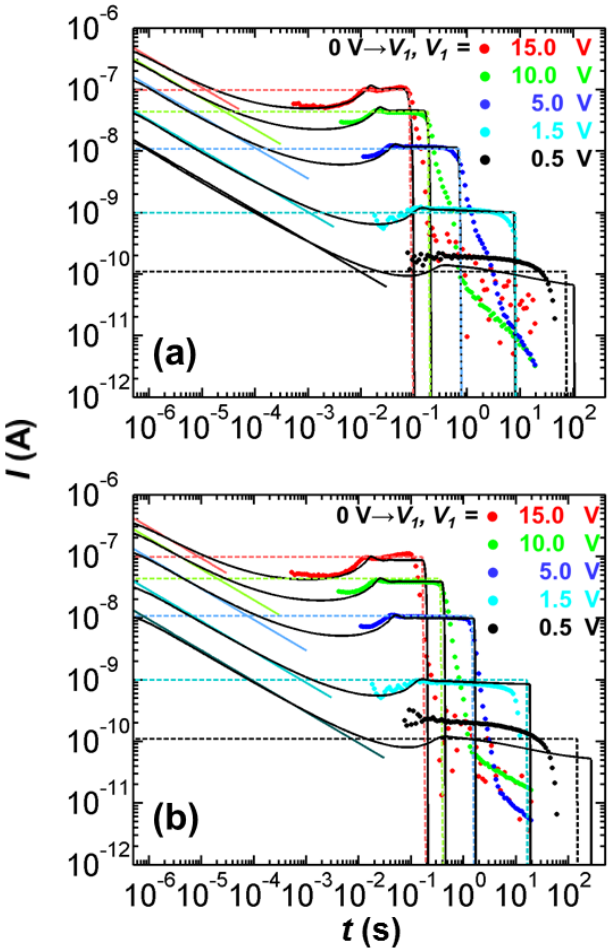

Figure 6.2: Measured currents (colored dots) for the experiment type A are compared with the simulated currents (black lines) for a device with d = 20 µm which was filled with a suspension (a) ϕ_m = 0.003 (b) ϕ_m = 0.006 of OLOA 11K in dodecane. The full colored lines show the calculated currents using Eq.6.17 : $\frac{\varepsilon_o \varepsilon_r S V_1}{d^2}\sqrt{\frac{\mu k_B T}{2et}}$. The constant currents (I_{ss}) shown by dotted color lines match with the Mott-Gurney Eq. 6.23 showing a V_1^2 dependency.

and 0.006, for which the integrals of the measured currents (Q*) for 0→V_2 are 8 nC (a) and 16 nC (b). Approximately the same duration and integral of the currents is measured for 0→-V_2, confirming that the SCIMs are redistributed equally on both electrodes during t_{s1}. From the integral of the

currents, the duration of the stationary state currents can be calculated as follows: $t_{ss} = Q^*/I_{ss}$, where I_{ss} is the stationary state current and t_{ss} is the duration up to which constant currents are measured (I_{ss}). These values of t_{ss} are indicated by the vertical lines in Fig. 6.2.

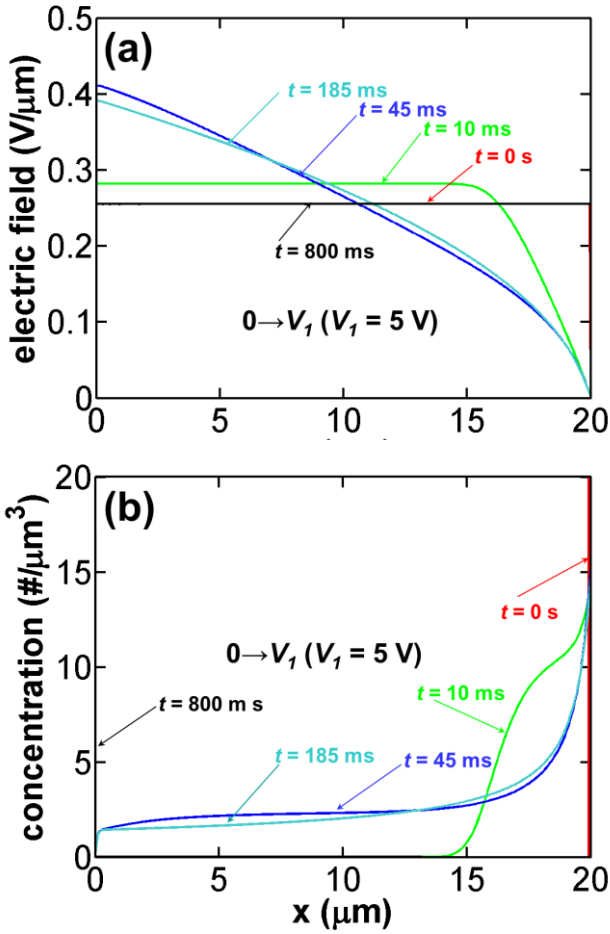

Figure 6.3: Simulated transient profile of (a) the electric field (b) the concentration of the released SCIMs for the experiment type A in a device with d = 20 μm with ϕ_m = 0.003. The SCIMs are released from the interface layer situated at the right electrode (shown by a red line) clamping the field to zero. The stationary state is reached around 45 ms and lasts up to 800 ms. The simulation parameters are: μ =1320 μm^2/Vs and N_{SCIMs}= 500 μm^{-2}.

Now the shape of the current is explained in more detail on the basis of transient variations of the electric field and the concentration of the SCIMs between the electrodes (see Fig. 6.3). Up to a few ms the currents decrease

according to $\propto \frac{1}{\sqrt{t}}$, see Eq. 6.17. This decrease in the current is observed until the released SCIMs travel deeper into the bulk, where the electric field is higher and drift dominates over diffusion. Then the current increases for a short duration (see Fig. 6.2 (a)) up to t_2 = 10 ms. Afterwards, the stationary state begins (t_2 > 10 ms for V_2 = 5 V, see Fig. 6.2 (a) and (b)) during which the flux becomes uniform everywhere in the device ($\Psi_{SCIMs} \approx -n_{SCIMs}\mu E$ is approximately constant), resulting in a constant current matching with the Mott-Gurney equation [103,104,106]. The constant currents are measured up to the time $t_{ss.}$. Eventually, the interface layer is exhausted of SCIMs and the currents start decreasing and approximately become zero. It must be noted that the SCIMs again join the interface layer when they reach the opposite polarity electrode.

6.4.2 With the Presence of Regular CIMs

A comparison between the reversal transient current measurements and the simulations for the experiment type B is shown in Fig. 6.4. The transient currents up to the first peak are due to the release of the regular CIMs from the double layer formed during the polarizing voltage step. This peak and the shape of the reverse current up to the first peak is due to drift and diffusion of the regular CIMs [77]. The second peak, which is in some cases not more than a small contribution, is due to the release of SCIMs from the interface layer. The release of SCIMs starts only when the electric field changes sign at the boundary between the interface layer and the bulk and is space-charge-limited. Since the shape and the origin of the first peak have been explained earlier in detail in chapter 3 (section 3.3.2.2), in this section only the second peak is focused. In Fig. 6.4, the simulation parameters to simulate the first peak are: μ = 1320 μm^2 , $\bar{n}$ =3.6 (Fig. 6.4 (a)), 11(Fig. 6.4 (b)), 3.9 (Fig. 6.4 (c)) and 10.3 (Fig. 6.4 (d)) μm^{-3}.

From Fig. 6.4, it can be observed that for a small value of ϕ_m = 0.001 (see Fig 6.4 (a)) the measurements are in good agreement with the simulation results (except for V_2 = 0 V, which will be explained later). For increasing values of ϕ_m and *d*, in the measurements a peak is observed for the voltage V_2 > 1 V (second peak) while the simulations rather show a plateau current. Nonetheless, the integral of the current in the second peak (Q_{sp}) does not depend on the amplitude of the voltage V_2 and is given by Q_{sp} = 8, 23, 14 and 45 nC for the experiments in Figs. 6.4 (a), (b), (c) and (d) respectively. . To

simulate the current just after the first peak in Fig. 6.4 the used mobility of the SCIMs is 1320 μm^2 and the densities of SCIMs in the interface layer for Fig. 6.4 (a), 6.4 (b), 6.4 (c) and 6.4 9 (d) consecutively are: 500, 1438, 875 and 2813μm^{-2}.

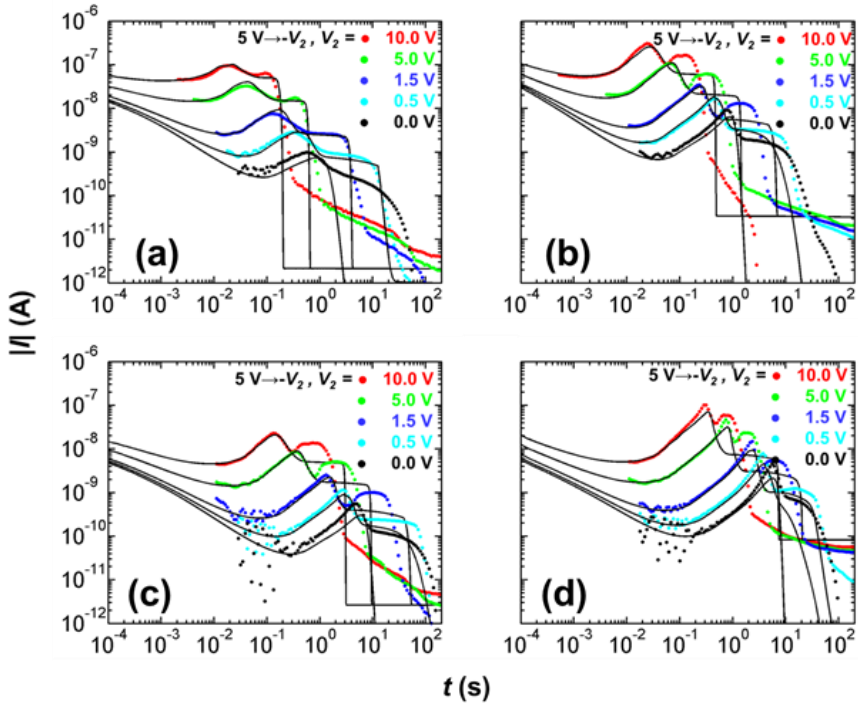

Figure 6.4: Measured transient currents $|I|$ (colored dots) for the experiment type B are compared with the simulated currents (black lines) for 5 V→-V_2. The measurements are performed on devices with thickness d filled with a suspension of OLOA 11K in dodecane (a) d = 20 μm with ϕ_m = 0.001) (b) d = 20 μm with ϕ_m = 0.003 (c) d = 46 μm with ϕ_m = 0.001 (d) d = 46 μm with ϕ_m = 0.003.

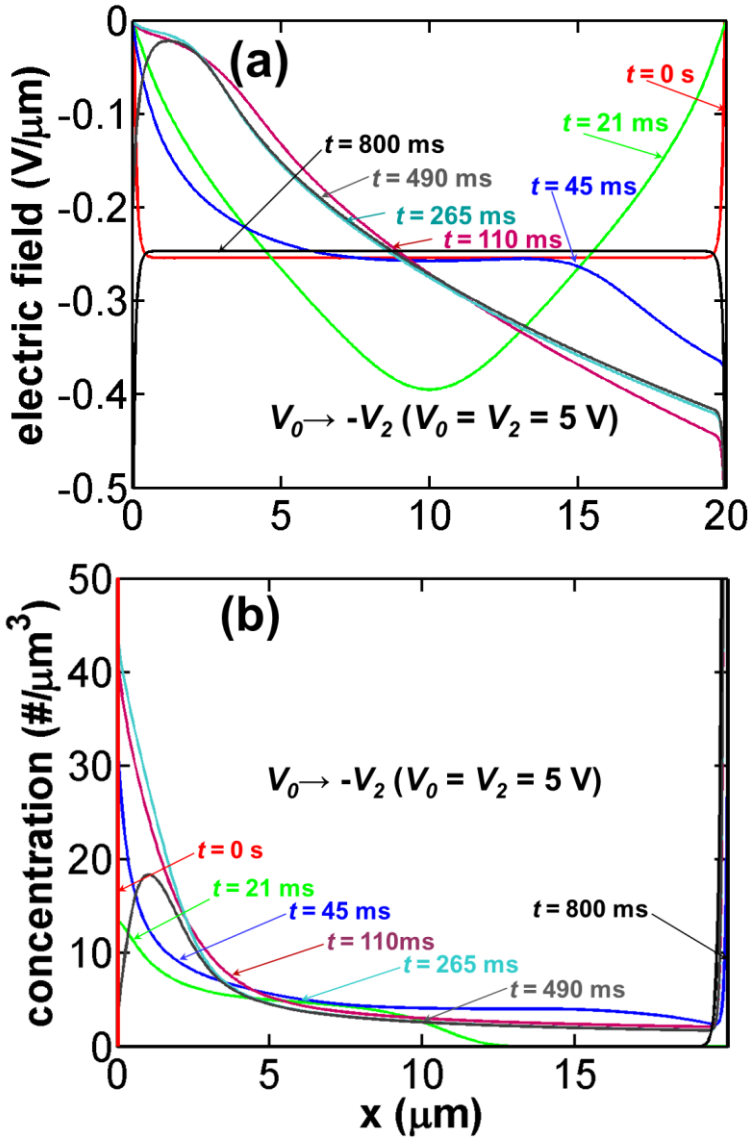

Figure 6.5: Simulated transient profile of (a) the electric field (b) the concentration of the regular CIMs and SCIMs for the experiment type B in a device with d = 20 μm filled with a suspension ϕ_m = 0.001 OLOA 11K in dodecane. The SCIMs are released from the interface layer situated at the left electrode shown by red vertical line. The SCIMs are released when the field changes sign at the boundary of the interface layer towards the bulk. The simulation parameters are: μ =1320 μm^2/Vs, $\bar{n}$ = 3.6 μm^{-3} and N_{SCIMs}= 500 μm^{-2} .

Now let us explain the occurrence of the approximately constant plateau currents in the simulations due to the release of SCIMs in a device with ϕ_m= 0.003 and d = 20 µm for which the measured currents agree with the simulations (see Fig. 6.4 (a)) on the basis of the transient electric field and the concentration profile (see Fig. 6.5). The electric field changes sign at the electrodes 21 ms after reversing the polarity of the voltage ($V_0 \rightarrow -V_2$, $V_0 = V_2$ = 5 V). Then, the release of SCIMs from the interface layer starts clamping the field to zero at the boundary of the interface layer and the bulk.

At the vicinity of the electrode (from which SCIMs are released) the field becomes very weak due to the space charge effect, see Fig. 6.5 (a) at x = 0. Therefore, the release of SCIMs is diffusion-based. The decreasing currents related to this charge diffusion are observed for a short duration (35 ms < t < 45 ms for V_2 = 5 V in Fig. 6.4 (a)), until the released SCIMs have diffused sufficiently far away from the electrode (x >> 0). Then, the stationary state starts during which the flux of SCIMs becomes uniform everywhere in the device resulting in a constant current until complete exhaustion of the charges in the interface layer. Afterwards, the concentration of SCIMs starts decreasing in the bulk, resulting in a decrease of the current. On reaching the opposite electrode, the SCIMs again end up in the interface layer, which is verified by the occurrence of the constant current or second peak for the oscillating voltages ($0 \rightarrow V_0 \rightarrow -V_2 \rightarrow V_2 \ldots, V_0$ & V_2 >1), indicated by Fig. 5.3 (b) in Chapter 5.

The discrepancies between the measurements and the simulations in the case of experiment type B (Fig. 6.4 (b, c, & d)) for increasing values of ϕ_m and d for the voltages V_2 > 1 V can be explained on the basis of electrohydrodynamic (EHD) flows. EHD flow in a device can occur during the reverse voltage due to local variations in the electric field at the vicinity of electrodes caused by variations in the concentration of CIMs. As a result of EHD flow, the released SCIMs can be transported much faster towards the opposite electrode, causing larger currents for a shorter duration and resulting in the second peak (Fig. 6.4 (b, c and d)). The charge in the interface layer is then exhausted faster and the current decreases earlier than if there would be no EHD effects, but the total transported charge remains the same, e.g. 23 nC (see Fig. 6.4 (b)). The hypothesis of EHD flow is supported by the fact that in the case of smaller ϕ_m and lower voltages, where EHD effects are expected to be much weaker, the measurements and

the simulations agree well. Obviously, in the absence of regular CIMs, EHD effects are not expected at all. Therefore the measurements and the simulations for experiment type A ($0 \rightarrow V_2$ and $V_2 \rightarrow -V_2$ (not shown)) in Fig. 6.2 agree much better. For the case of Fig. 6.4 (d), EHD flows occur during the release of regular CIMs resulting in the mismatch between the measurements and the simulations for $V_2 > 1$ V before the occurrence of the first peak. In chapter 3, section 3.3.3, transient trajectories of the tracer particles for the reversal voltages $V_2 > 1$ have already demonstrated the occurrence of EHD flow.

The discrepancy between the measurements and the simulations for very low voltages in experiment type B (see Fig. 6.4) for $V_2 < 0.5$ V, can be explained as follows. In the model the SCIMs are released when the field changes sign at the electrodes (the interface layer) and the release is space charge limited. However, in reality the SCIMs can also be released due to their thermal energy. If the SCIMs are in multiple layers at the electrodes the chance of such thermal release is even higher. The fact that the measured currents up to $V_2 = \pm 0.2$ V ($d = 46$ μm) and $V_2 = \pm 0.5$ V ($d = 20$ μm) for the experiment type B were found to be independent of the polarity of the applied voltages ($V_0 \rightarrow \pm V_2$) supports this hypothesis because at low voltages the SCIMs can be released due to diffusion.

6.5 Conclusions

A model based on space-charge-limited release of SCIMs is presented and the results of the model (simulations and analytical formulas) are compared with the experimental results. For a simple situation in which the regular CIMs are removed and only SCIMs contribute to the current, the release of SCIMs from the interface layers is space charge limited and the resulting currents match with the Mott-Gurney equation. The match between the experimental results and the simulations verifies the release mechanism of SCIMs from the interface layer. In addition to this, the match between measurements and simulations also verifies that only a single polarity of charge is released from the interface layers. In the case of a complex situation in the presence of regular CIMs, the simulation results are in agreement with the experiments for small values of $\bar{n}$ while for larger values of $\bar{n}$, in the experiments a peak is observed while the simulations result in rather constant currents. This mismatch between the measurements and

simulations for a large value of $\bar{n}$ is attributed to EHD flow that could occur due to local variations in the electric field next to the electrodes.

Chapter 7

Electrokinetics of Colloidal Particles and Charged Inverse Micelles

The electrodynamics of dispersions of charged inverse micelles (CIMs) and charged colloidal particles are studied separately for alternating voltages, specifically in response to triangular voltages. Such investigations shed light on the electrodynamic, interfacial behavior and on the release of CIMs and charged particles in response to continuously switching voltages. This study is relevant for EPDs and liquid toner printing in which CIMs with charged colloidal particles are switched between two electrodes or charged surfaces.

7.1 Introduction

In the colloid literature, two types of studies have been performed on non-polar colloidal dispersions. In the first type of study, charge, charge dynamics and interfacial behavior of charges related to added surfactant, are studied in the absence of colloidal particles [25,27,52] while in the second type, the fundamental mechanism of surfactant-promoted particle charging and the stabilization of particles in the dispersion are investigated [10,17,26]. For the first type of study, conductivity measurements [24,57], transient current measurements [6,79], dynamic/static light scattering [11,15] and

small angle neutron scattering [62] are employed. From these studies, a better understanding about surfactant mediated charging, the nature of the charge carriers and their electrodynamics and interfacial behavior has been developed [6,20,26]. The second type of study is usually based on measurements of the interaction potential between pairs of particles [12,19], the electrophoretic mobility [10,78] and charge fluctuation of the particle over time. A better insight about the electrokinetics of colloidal particles in a non-polar dispersion has been obtained but there is an ongoing discussion on some issues such as the precise charging mechanism of particles and charge stabilization [2,25]. Apart from the mentioned studies, there are a few studies on the electrokinetics of colloidal particles at the vicinity of electrodes [92,93,95,96] and studies on the formation of interfacial layers and about the occurrence of electrohydrodynamic instabilities that lead to complex particle dynamics and pattern formation [96,108]. However, there is no systematic study about the effect of interfaces on the switching characteristics and on the charge of the colloidal particles in the presence of CIMs. Such studies are relevant for an EPD in which both the charged colloidal particles and the CIMs concentrate near the electrodes when a voltage is applied, and switch to the opposite electrode when the polarity of the voltage is reversed.

In this chapter, the electrodynamics and the interfacial behavior of charged colloidal particles in response to an oscillating voltage (more precisely a triangular voltage) are studied. The voltage is applied across the electrodes of a device filled with a dispersion of particles and the corresponding currents are measured in the external circuit. From the measured current, information about the electrodynamics and the interfacial behavior of the charged colloidal particles is acquired.

7.2 Material and Methods

7.2.1 Materials

In this chapter, the electrical properties of a suspension of the dispersing agent Solsperse (Lubrizol) in lytol, with and without toner particles (Xeikon: MC2361) are investigated. The dispersed toner particles are made of polystyrene. Lytol has a dynamic viscosity of 5.5 mPa. s and Solsperse is used as a charging agent. The liquid toner dispersion contains 35 wt% solid content (particles) while 65 wt% is the carrier liquid with charging agent. For this study, a number of different dispersions with and without toner particles are prepared.

7.2.2 Methods

7.2.2.1 Electrical Current Measurements

Both electrical and optical measurement techniques were used. The electrical current measurements are performed using a setup (the high field toner cell or HFTC) which is a combination of various instruments that are controlled by a pc, as shown in Fig.7.1. The HFTC setup was designed by Xeikon specifically to study the electrical behavior of dispersions with a very high concentration of particles such as typical liquid toners and at voltages of hundreds of Volts. In addition, the spacing between the steel electrodes can be adjusted easily and can be cleaned easily. The transient current measurement setup from the previous chapters is not designed for such high voltages or for samples with steel electrodes, and is therefore not used. The setup has three parts: the toner cell, a Keithley source meter 2612A and a pc. The toner cell consists of two parallel circular steel plates with surface area S= 4.93 cm^2 that are separated at a distance d. The lower plate of the cell is fixed and acts as a base while the upper plate is moveable as shown in Fig. 7.1 (a, a' & b). The two plates are placed parallel to each other in such a way that the electrodes overlap completely, and then the distance between the plates is controlled by moving the upper plate up or down. The distance between the plates is obtained from a measurement of the capacitance between the plates (with no liquid present), using the formula: $d = (\varepsilon_0 \varepsilon_r S)/C$. A temperature sensor integrated in the toner cell is used to monitor the temperature of the cell. The Keithley source meter is used to

apply a voltage across the electrodes of the toner cell and to measure the corresponding current simultaneously. A computer is used to control the electronics of the setup and to display the resulting current/voltage profile. The experimental procedure is as follows: firstly the distance between the electrodes is controlled by perfectly overlapping the two electrodes and measuring the air capacitance of the device. Then, the device is opened and the space between the electrodes is filled with a mixture as shown in Fig. 7.1 (b). Afterwards the upper electrode is placed back in its original position, ensuring complete overlapping of the electrodes at the desired distance, Fig. 7.1 (c). Subsequently, a triangular voltage (amplitude 1 V to 400 V, frequency 5 Hz) is applied across the electrodes and the corresponding current is measured.

In order to investigate the electrical behavior of liquid toner particles, four types of electrical current measurements were performed. In the first type (Type A) of experiment, the isolated electrodynamics of charged inverse micelles as a function of the amplitude of the applied triangular voltage is studied without the presence of liquid toner particles. The type A measurements are performed on a mixture of Solsperse with $\phi_m = 0.0005$ in lytol ($\eta = 5.5$ mPas). In the type B experiment, the combined electrodynamics and interfacial behavior of Solsperse ($\phi_m = 0.001$) CIMs with a low concentration of toner particles ($\phi_m = 0.07$) are studied as a function of the amplitude of the applied triangular wave voltage. For the type B experiments two dispersions, one with $\phi_m = 0.001$ Solsperse in lytol and the other with $\phi_m = 0.2$ (solid content 7 wt %) of original liquid toner (solid content 35 %) in lytol are mixed together, so that in the final dispersion mass fractions $\phi_m = 0.1$ of liquid toner (solid content 3.5 wt%) and $\phi_m = 0.0005$ of Solsperse in lytol are obtained. In the type C experiment, the electrodynamics and effects of the interfaces on 50 % diluted liquid toner in lytol are studied while in the type D experiment, the same is studied on the original liquid toner.

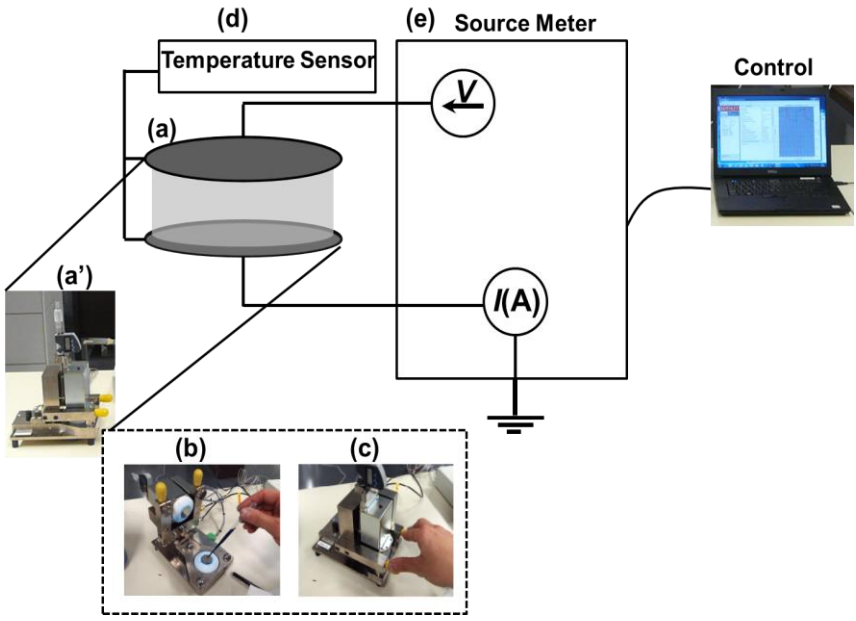

Figure 7.1: Schematic of the HFTC setup. The setup comprises (a & a') the liquid toner cell with two circular electrodes, (b, c) filling and closing of the electrodes of the toner cell. (d) A temperature sensor is used to monitor the temperature of the cell (e) The Keithley source meter is used to apply a voltage and to measure the corresponding current simultaneously. (f) A pc is used to control the electronics of the setup and to display the current-voltage profile.

7.2.2.2 Optical Setup and Measurements

Optical measurements are used to estimate the mobility, the charge and the size of the individual colloidal particles and to study the electrokinetics of the particles in the vicinity of the electrodes. In general two types of optical measurement were performed (type E and F).

The type E experiment is performed to estimate the mobility and the hydrodynamic radius of the particles. The used experimental setup was very similar to the set up that has been described in chapter 3, section 3.2.2. However, for the present case the measurement device is made of two gold coated parallel electrodes separated by d = 70 µm, as shown in Fig. 7.2 (a). The gold coated electrodes are specifically used to generate a uniform one dimensional field between the electrodes. The experimental sequence is as follows: firstly a 1:100 diluted dispersion of liquid toner in lytol is prepared.

Then, the space between the electrodes is filled and the electrodes are covered with a cover glass plate to minimize the effects of the surrounding

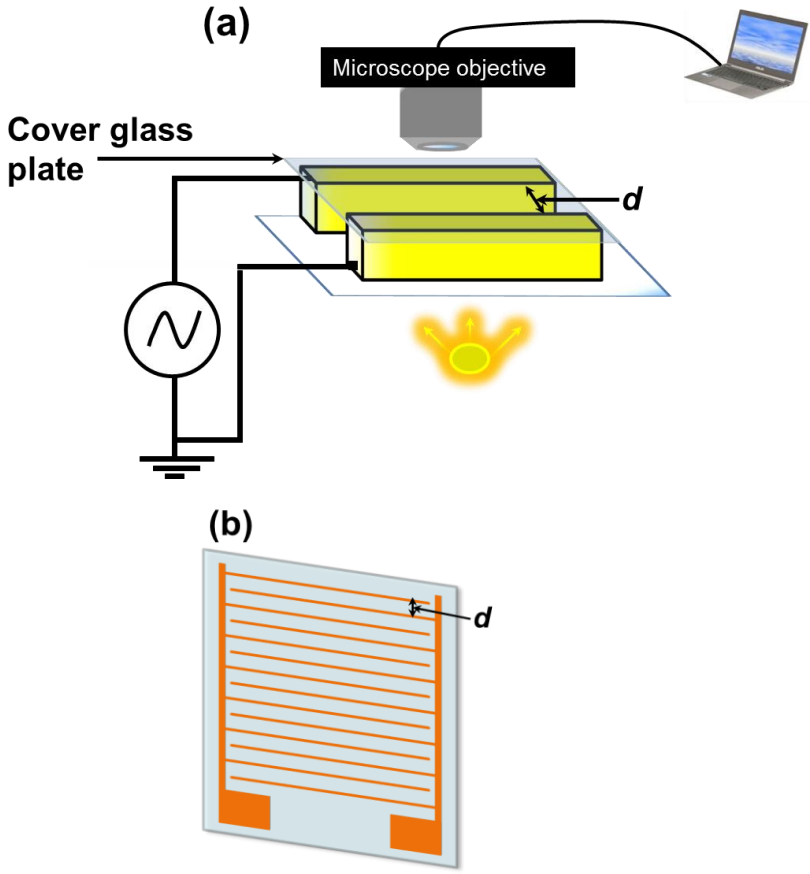

Figure 7.2: (a) The single particle tracking set up. (b) A glass substrate with ITO interdigitated electrodes. A thin layer of liquid toner is deposited on the substrate and placed underneath the microscope objective and an area is brought into focus. Then a ac/dc voltage is applied across the electrodes and images are acquired.

perturbation on the setup. Afterwards, the setup is short circuited for at least 100 s to ensure a homogeneous distribution of the charge between the electrodes. Then a particle is brought into focus and images of the particle are acquired in the absence of an electric field for 2 s. Subsequently, a sinusoidal voltage (amplitude 50 V with a frequency of 10 Hz) is applied across the electrodes and images are acquired at a frequency of 100 Hz. The whole experiment is controlled by a LabVIEW program using a graphical

user interface. By image analysis of the acquired images, the discrete positions of the particle are extracted in the *xy*-plane (*x, y*). The *x*-direction is chosen perpendicular to the electrodes and parallel to the direction of applied electric field. From the acquired position data of the particle in the absence of a field, the hydrodynamic radius of the particle is estimated. The position data obtained in the presence of an applied voltage is used to estimate the average mobility of the particle.

The type F experiment is performed to study the electrokinetics of colloidal particles in the vicinity of electrodes. The device that was used for the type E experiments is replaced by a glass substrate of thickness 1 mm with interdigitated ITO electrodes, a schematic of which is shown in Fig. 7.2 (b). The center to center distance between two consecutive electrodes is d = 200 μm with a width of 30 μm and a thickness of 30 nm. A layer of diluted liquid toner (ϕ_m = 0.25 in lytol) is deposited on the finger pattern. The thickness of the layer was measured optically and was found to vary between 20 and 30 μm from experiment to experiment. The substrate with the liquid toner layer is placed underneath the objective of the microscope (no cover glass is used in this case) and the electrodes are connected to a voltage source. A part of the substrate is focused; to achieve a maximum field of view in this case a 10X objective was used. Firstly, the electrodes are short circuited for 100 s. Then a dc voltage (100 to 400 V) is applied for 19 s and the images were acquired at 15 Hz.

7.3 Theoretical Model

7.3.1 Electrical Currents

In this section an equation for the current in nonpolar liquids in response to a triangular voltage is derived. Depending on the peak value of the applied voltage and the frequency, the measured current can be categorized in two regimes, a linear and a non-linear regime. In the linear regime, the measured conductive current due to movement of charges varies linearly with the voltage. A linear relation between the applied voltage and the measured conductive current is possible when the charges in the system do not move much from their initial positions, which is possible for large frequencies or low amplitudes of the applied voltage. In the non-linear regime, the charges move over a much larger distance from their initial positions, possibly all the

way to the electrode, resulting in the formation of space charge layers that cause a non-linear voltage-current relation. The non-linear regimes are observed for large voltages and small frequencies.

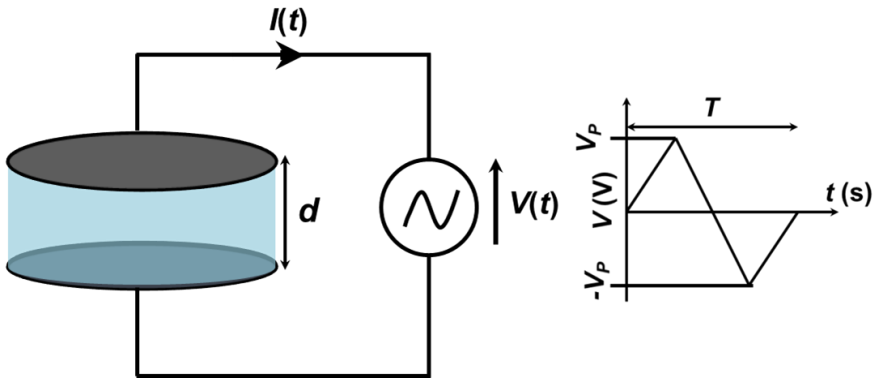

Figure 7.3: Schematic illustration of the measurement setup with two parallel circular steel plates with area *S* separated at a distance *d*. The space between the electrodes is filled with a prepared dispersion and then a triangular voltage of 5 Hz is applied across the electrodes

A period of a triangular voltage with frequency *f* and peak voltage V_p can be written as:

$$V(t) = \begin{cases} 4fV_p t, & 0 < t < 1/4f \\ -4fV_p(t - 1/2f), & 1/4f < t < 3/4f \\ 4fV_p(t - 1/f), & 3/4f < t < 1/f \end{cases} \tag{7.1}$$

The conductivity of a dispersion with CIMs and charged particles is given by:

$$\sigma = \sum_i Z_i e n_i \mu_i \tag{7.2}$$

Here, Z_i and μ_i are the values of the charge number and the mobility of the corresponding i_{th} charge carrier. The current measured in the external circuit in response to a triangular voltage can be interpreted as the superposition of a capacitive jump and the conductive current. The conductive current is due to the movement of charges in between the electrodes in response to the applied voltage. In the linear regime, when the charges do not move much and hence do not affect the field between the electrodes, the total measured current can be expressed as:

$$I(t) = \left(\frac{S\varepsilon_0\varepsilon_r}{d}\frac{\partial V(t)}{\partial t} + \frac{\sigma\, SV(t)}{d}\right) \tag{7.3}$$

Substituting the value of $V(t)$ from Eq. 7.1 to Eq. 7.3, it gives:

$$I(t) = \begin{cases} \frac{4\,S\varepsilon_0\varepsilon_r}{d} fV_p + \frac{4\sigma SfV_p}{d} t, 0 < t < \frac{1}{4f} \\ -\frac{4\,S\varepsilon_0\varepsilon_r}{d} fV_p - \frac{4\sigma SfV_p}{d}(t - 1/2f), \frac{1}{4f} < t < \frac{3}{4f} \\ \frac{4S\varepsilon_0\varepsilon_r}{d} fV_p + \frac{4\sigma SfV_p}{d}(t - 1/f), \frac{3}{4f} < t < \frac{1}{f} \end{cases} \tag{7.4}$$

In the non-linear regime, the charges move over a larger distance, depending on the magnitude of the applied voltage. The movement and separation of charges in the device affects the field in the device and the field no longer remains $V(t)/d$.

A rough estimation of the velocity and distance travelled by charges during a half cycle of a triangular voltage can be calculated by neglecting the effects of space charge. The velocity of charge carriers in response to a triangular voltage is given by:

$$v(t) = \begin{cases} (4f\mu V_p t)/d, & 0 < t < 1/4f \\ (4f\mu V_p(t - 1/2f))/d, & 1/4f < t < 1/2f \end{cases} \tag{7.5}$$

Integrating Eq. 7.5 for a half period of the voltage, the distance travelled by the charge carriers is: $l = \int_0^{1/4f} \frac{(4f\mu V_p t)}{d}\, dt + \int_{1/4f}^{1/2f} \frac{(4f\mu V_p(t-1/2f))}{d} dt$, resulting in:

$$l = \frac{\mu V_p}{4fd} \tag{7.6}$$

7.3.2 The Size and Charge of Particles

The hydrodynamic radius r of a liquid toner particle can be estimated from the diffusion constant, using $r = k_B T/(6\pi\eta D)$. The diffusion constant of a particle can be estimated from the mean square displacement of the particle in free Brownian motion:$\langle R^2 \rangle = 2Dt$. Consider a particle moving randomly

because of Brownian motion, of which the x, y-position is sampled at regular times $t_i = (i-1)\Delta t$, with $i = 1{:}\, N+1$. From the N square displacements:

$$R_i^2 = \big(x(t_{i+1}) - x(t_i)\big)^2 + \big(y(t_{i+1}) - y(t_i)\big)^2 \tag{7.7}$$

The mean square displacement can be calculated, resulting in an estimation for the diffusion constant [109]:

$$D = \frac{1}{2N\Delta t}\sum_{i=1}^{N} R_i^2 \tag{7.8}$$

The hydrodynamic radius of the particle is then:

$$r = \frac{k_B T}{6\pi\eta D} \tag{7.9}$$

To measure the mobility using the single particle tracking method, the concentration of the particles in the dispersion must be very low. For the present case, the original liquid toner dispersion was diluted 100 times in lytol. In such a highly diluted dispersion of liquid toner, the estimated concentration of free charges in the bulk is found to be less than $10^{17}/m^{3.}$ From this, the estimated Debye length in the diluted liquid toner is 6 μm, which is much larger than the average hydrodynamic radius (≈1μm) of the particles. Therefore, the Hückel limit can be used to estimate the charge on a liquid toner particle [69]. The charge and the mobility of a particle are linked by the relation:

$$\mu = \frac{Ze}{6\pi\eta r} \tag{7.10}$$

7.4 Results and Discussion

7.4.1 Comparison Between Measured and Simulated Currents

A comparison between the measurements and simulations for a triangular voltage of 5 Hz applied over a mixture of Solsperse with mass fraction $\phi_m = 0.0005$ in lytol (η = 5.5 mPa. s) in the HFTC device with d = 40 μm is

shown in Fig. 7.4. For the simulation the same model with the same initial and boundary conditions is used as in chapter 2, section 2.5. The simulation parameters such as the mobility and the concentration of CIMs are estimated by matching the simulated currents with the measured currents for a small voltage (V_p < 20 V) or for at least the first half cycle (t = 0 to 0.05 s) of a large voltage. It can be seen in Fig. 7.4, for the voltages V_p > 20 V, that there

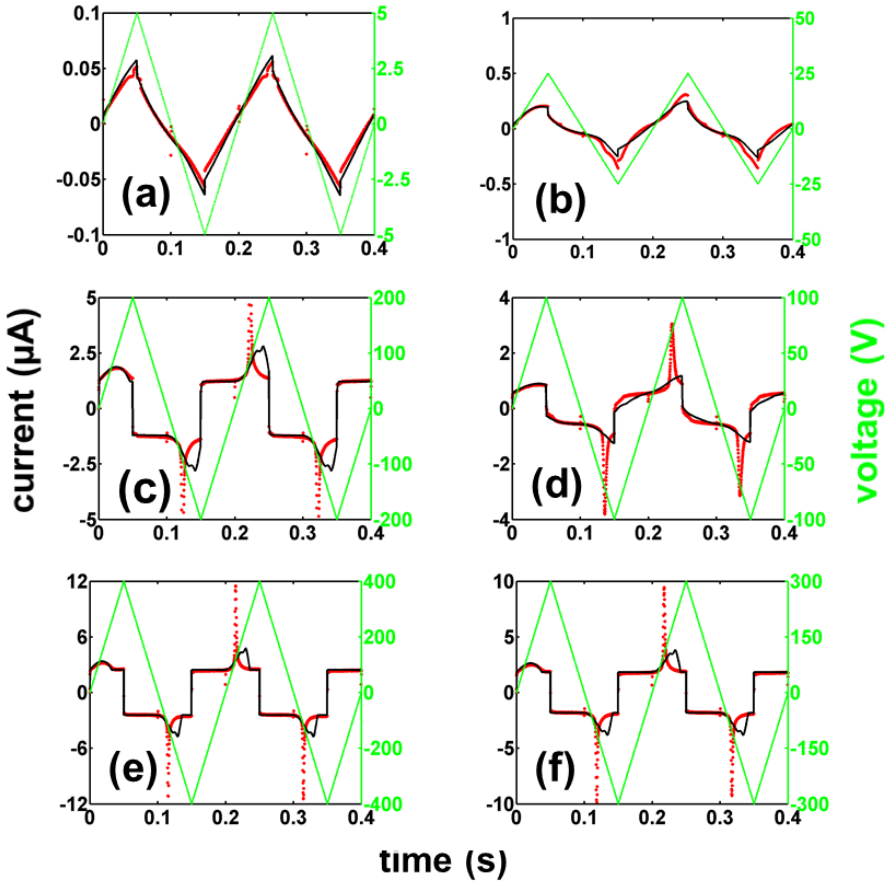

Figure 7.4: The measured currents for the experiment type A (red color dots) for a solution of Solsperse ϕ_m = 0.0005 in lytol using the HFTC setup with d = 40 μm and S = 4.93 cm^2 are compared with simulated currents (black lines) for triangular wave voltages of frequency 5 Hz. The peak values of the applied voltages are (a) V_p = 5 V (b) V_p = 50 V (c) V_p = 100 V (d) V_p = 200 V (e) V_p = 300 V (f) V_p = 400 V. The values of simulation parameters are: μ = 210 μm^2/Vs and $\bar{n}$ =7.5 μm^{-3}.

is a discrepancy between the measurements and simulations after the first half cycles, the reason for this will be explained in later in this section. The obtained values of the mobility and the concentration of CIMs for the mixture are 210 $\mu m^2/Vs$ and 7.5 μm^{-3}, respectively. The reported value of the mobility of CIMs for a solution of Solsperse with $\phi_m = 0.001$ in dodecane ($\eta = 1.38$ mPa. s) is 760 $\mu m^2/Vs$ [74]. If we assume that the mobility scales inversely proportional with the viscosity of the solvent (lytol versus dodecane), the expectation value for the mobility in lytol is 190 $\mu m^2/Vs$, which is similar to the value used in the simulations (210 $\mu m^2/Vs$). By measuring the mobility of Solsperse CIMs in lytol as a function of ϕ_m, it is found that for a large value of ϕ_m, the mass fraction does not have an influence on the size of the CIMs and the obtained value of the mobility matches with the expected value, i.e, 190 $\mu m^2/Vs$, see Fig. 7.5 (a). However, for small values of $\phi_m < 0.001$, a slightly higher mobility is found for lower mass fractions. It may be possible that the CIMs are slightly smaller at lower concentrations. The concentration of the CIMs increases linearly with ϕ_m as is expected from the disproportionation mechanism and follows the trend line: $\bar{n} = 16500 \times \phi_m\ \mu m^{-3}$, as shown in Fig. 7.5 (b).

The good match between the measurements and simulations for small voltages indicates that the currents can be described by drift and diffusion of the CIMs in response to the applied voltage. In the linear regime (V_p = 5 V, in Fig. 7.4 (a)) in which $V(t) \propto I(t)$, the currents are given by Eq.7.4. For the other voltages in Fig. 7.4, the measured currents match well with the simulations from 0 to 0.1 s. After 0.1 s there is a discrepancy in the form of a peak in the measured current. For intermediate voltages up to V_p = 100 V, the integral of the measured current peak after the first half cycle of the voltage is larger than the integral of the simulated current peak. This can be explained since the charges from the measurements are completely separated while the charges in the simulation are not completely separated. For very large voltages V_p = 100 V to 400 V, the integrals of the peaks are the same: 20 nC. However, the peak in the measured current occurs much earlier than the peak in the simulated current, see Fig. 7.4 (d, e and f).

The triangular voltage starts at t = 0 s, when the CIMs are distributed uniformly in the device. The measured current for the first half cycle ($0 < t \leq$ 0.1 s) of the triangular voltage can be explained as follows: during a linearly increasing and decreasing voltage and neglecting the effects of space charge,

the distance travelled by CIMs can be estimated by using Eq. 7.6.. When the frequency *f* is constant, the travelled distance varies as $l \propto V_p$.

For very low voltages ($V_p < 20$ V) $d \gg l$, so the CIMs do not move much from their initial positions. For example, the distances travelled by the CIMs when V_p = 5, 10 and 20 V are 1.3,2.6 and 5.25 μm respectively, which are much smaller than the distance between the electrodes, i.e. 40 μm. Therefore, the field in the device remains approximately *V(t)/d* and the linear approximation is valid, Fig. 7.4 (a). For intermediate voltages (~ 20 V $< V_p < 100$ V) $l > d$, the CIMs move over a larger distance (see Fig. 7.6 (b)) and the resulting space charge affects the field in the device, Fig. 7.6 (a). This results in a nonlinear current, Fig. 7.4 (b). For large voltages (V_p > 100 V),$l \approx d$ and the CIMs move all the way to the electrodes until the bulk is depleted of CIMs. The variation in the concentration of CIMs and the electric field in the device are shown in Fig. 7.6 (c & d). The separation of CIMs (up to *t* = 0.03 s for V_p = 400 V) results in an increasing current while during the depletion phase the current decreases due to the arrival of CIMs at the opposite polarity electrodes.

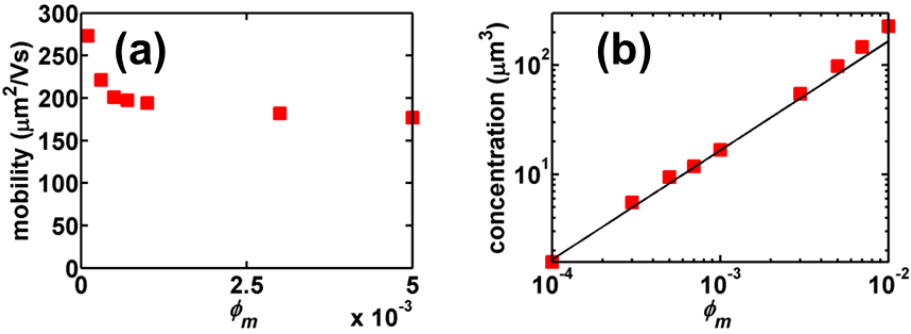

Figure 7.5: (a) The variation of the mobility of Solsperse CIMs in lytol with ϕ_m. (b) The linearly increasing concentration on logarithmic axes of the CIMs with ϕ_m verifies the bulk disproportionation mechanism and the black line shows the trend line: $\bar{n} = 16500 \times \phi_m$ μm^{-3}.

The discrepancies between the measurements and simulations for larger voltages just after first half cycle (*t* > 0.1 s, in Fig. 7.4 (b to f)) can be attributed to electrohydrodynamic (EHD) instabilities that are likely to occur for the reversal voltages with a large value of V_p [77]. Due to EHD flow,

convection channels are formed between the electrodes thorough which the CIMs are transported much faster and arrive quicker to the opposite polarity

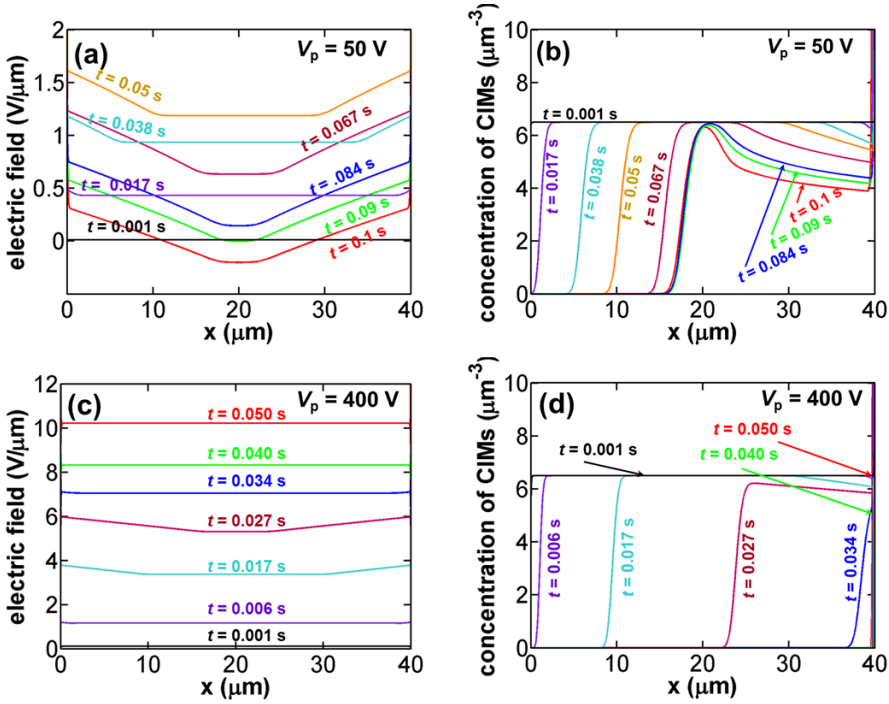

Figure 7.6: The simulated variations in the electric field (a & c) and the concentration of the positive CIMs (b & d) between the electrodes in response to a triangular voltage $0 \rightarrow V(t)$ for a duration of 0.1 s. The electrodes are separated at a distance d = 40 μm and have an overlapping area of S = 4.93 cm^2. For (a, b), the peak value of the applied voltage is 50 V while for (c, d), the peak value of the applied voltage is 400 V. The values of simulation parameters are: μ = 210 μm^2/Vs and $\bar{n}$ =7.5 μm^{-3}.

electrode. For intermediate voltages, the mismatch in the integral of the measured and that of the simulated current peak is also a consequence of the EHD flow in the bulk: due to the EHD flow, practically all charges are transported to the opposite electrode through the formed convection channels while in the simulation the voltage is not high enough for all CIMs to be transported to the electrodes, see Fig. 7.6 (b). For the largest voltages, the integral of the measured current peak matches with the simulation because the field is strong enough so that also without EHD flow all the bulk charge is transported to the electrodes before the field changes sign. However, the

measured current peak is much larger and has a shorter duration than the simulated current peak (V_p > 200 V). The reason for this is that, due to the EHD flow, the CIMs are transported faster to the opposite polarity electrode, resulting in a larger current with a shorter duration than in the simulation, where the CIMs are transported according to drift and diffusion.

7.4.2 Currents Measurements For Non-Polar Dispersions With a Low Concentration of Liquid Toner Particles in Lytol

The measured currents for a solution of Solsperse in lytol (Type A) and for a dispersion of toner particles with Solsperse in lytol (Type B) are shown in Fig. 7.7. The absolute values of the measured currents corresponding to all half cycles of the triangular voltage ($0 \rightarrow V(t)$, $V(t) \rightarrow -V(t)$ and $-V(t) \rightarrow V(t)$) are placed one over other in the same figures. The constant currents up to 0.05 s are due to capacitive charging. The current measurements corresponding to a solution of Solsperse in lytol show a single peak after 0.05 s, which becomes narrower for larger voltages, while the total integral of the peak remains the same, i.e., 34 nC for $-V(t) \rightarrow V(t)$ or $V(t) \rightarrow -V(t)$ (17 nC for $0 \rightarrow V(t)$ when $V_p \geq 100$ V), see Fig. 7.8 (a). As explained in the previous section, EHD flow occurs for larger voltages ($-V(t) \rightarrow V(t)$ or $V(t) \rightarrow -V(t)$) due to which the CIMs are transported quickly to the opposite electrodes, resulting in a narrow current peak.

The measured currents for the dispersion with particles and Solsperse are shown in Fig. 7.7 (c, d, e & f). In addition to becoming narrower with increasing voltage (V_p), an additional peak, growing each period, occurs between 0.05 s to 0.067 s. This peak is absent for the case when there are no toner particles in the solution (experiment type A), indicating that the growing peak is related to the liquid toner particles. Furthermore, the peak is observed only at large voltages and the magnitude of the peak increases with increasing magnitude of the voltage and increasing number of cycles, see insets in Fig. 7.7 (e & f). The peak starts at the moment when the voltage changes sign. From the transit time, the mobility of the particles responsible for the growing peak can be calculated as follows.

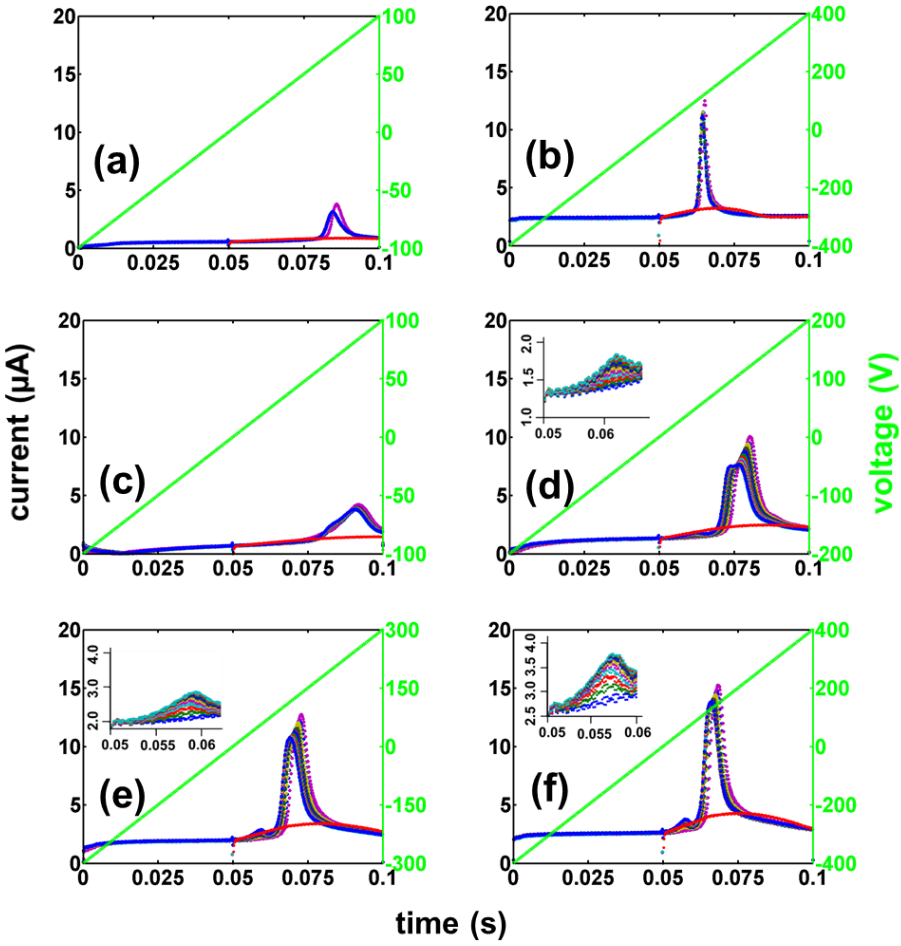

Figure 7.7: The measured current and the applied voltage in the experiment types A and B are shown. All the cycles of the current measured with the HFTC setup (S = 4.63 cm^2 and d = 40 μm) in response to a triangular voltage (0→*V(t)*, *V(t)*→-*V(t)* and -*V(t)*→*V(t)*) of 5 Hz with a total duration of 2.3 s are placed one over another. The measured current for the first quarter cycle of the voltage (0→*V(t)*), during which the charges move from a uniform distribution, is shown by a red line (0.05 to 0. 1 s). (a & b) show the currents for a solution of Solsperse with $\phi_m = 0.0005$ in lytol (without toner particles) in response to V_p = 100 V and V_p = 400 V respectively. (c)- (f) Measured currents for a dispersion with $\phi_m = 0.2$ of toner particles and $\phi_m = 0.001$ of Solsperse in lytol for V_p =(c) 100 V (d) 200 V (e) 300 V and (f) 400 V. For increasing V_p, a second peak in the interval t = [0.05 to 0.067 s] is observed in the current (inset figure in d, e & f). This peak is related to effects of the interfaces on the liquid toner particles and the peak increases each period until it reaches saturation.

When the voltage increases linearly up to a large enough voltage, all the CIMs and the particles move to the opposite polarity electrodes and end up in diffuse double layers [72,99]. Subsequently, the field in the bulk becomes ≈ *V(t)/d* [58,72,77]. Here it is important to note that EHD flow also plays an important role at large voltages (*V(t)*→-*V(t)* or vice versa). It is assumed that the EHD flow lasts until the arrival of CIMs and particles at the electrode with opposite polarity. However, in the measurements the current after the EHD peak reduces to the capacitive current, see Fig. 7.7 (d, e & f). Furthermore, when the voltage is reversed, the initial part of the measured current peak (~100 ms) matches well with the simulations, see Fig. 7.4 (d, e & f).This means that during the first 100 ms no EHD flow is observed.

When the voltage is reversed, up to a certain duration most of the CIMs stay at the electrodes because the direction of the field in the vicinity of the electrodes does not change instantly [77]. However, due to the large size of the particles, they do feel the field in the bulk, i.e. *V(t)/d* and start to move to the opposite electrodes. The velocity of the particles in the linearly increasing field in the bulk (at least up to t = 0.06 s) is given by: $v = \mu V(t)/d$. From this, the distance travelled by the particles in time t ($t \leq 1/4f$) can be calculated as: $\int_0^t v dt = \int_0^t (\mu V(t)/d) dt$. If the particles travel over the entire distance between the electrodes during a quarter period of the voltage, then the time taken by a particle to reach the opposite polarity electrodes is given by $t_{tr} = \sqrt{d^2/(2\mu V_p f)}$.The average value of the mobility of the particles can then be estimated by:

$$\mu = \frac{d^2}{2t_{tr}^2 V_p f} \tag{7.11}$$

Here, t_{tr} corresponds to the duration of the peak. For the case V_p = 400 V, the value of t_{tr} is = 0.01 s, see Fig. 7.7 (f), and the average value of the mobility of the particles is 4000 μm^2/Vs. This mobility is 5 times larger than that of the CIMs, confirming that this peak is not due to CIMs. The absence of the peak for small voltages and the reason that the peak grows in successive cycles will be explained in the next section.

The effect of the voltage and the number of cycles on the integral of the current peak is shown in Fig. 7.8. In Fig. 7.8 (a), the integral of the current

peaks are compared for the solution of Solsperse (experiment type A) and that of the dispersion with particles (experiment type B). For both cases the integral of the peak is approximately constant and does not change much with time. The constant level of the integral indicates that the overall charge in the solution does not change with time. The difference in the integral of the peak without (Type A) and with particles (Type B) is due to the presence of charged particles that apparently increases the total charge in the system. In section 7.4.3, it will be shown that the particles have an average charge of 18*e*.

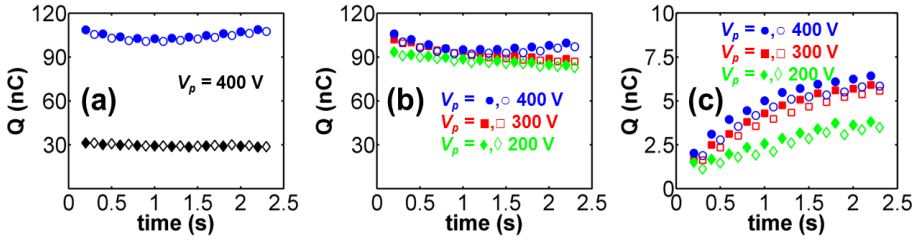

Figure 7.8: The integral of the current (shown in Fig. 7.7) after the capacitive part is subtracted is plotted as a function of time. The filled data points show the integral of the current for *-V(t)→V(t)* while the empty data points show the same for *V(t)→ -V(t)*. In (a) the integral of the current peaks for a solution of $\phi_m = 0.0005$ Solsperse in lytol (black color symbols) is compared with the integral of the current peaks for a mixture of Solsperse ($\phi_m =$ 0.001) and toner particles ($\phi_m = 0.2$) in lytol (blue color) for V_p = 400 V. In (b), the integral of the current peaks for a mixture of Solsperse ($\phi_m = 0.001$) and toner particles ($\phi_m = 0.2$) in lytol. In (c), the integral of the current peak due to the particles is plotted from Fig. 7.7 (d, e & f).

Similar measurements (type B) were also performed on the same solution with increasing voltages (V_p) and it is found that the integral of the current, and thus the total charge in the device, does not change, Fig. 7.8 (b). The integrals of the growing peak between 0.05 s to 0.067 s in Fig. 7.6 (d, e &f) are plotted in Fig. 7.8 (c), showing that the integral of the peak increases with the number of cycles and finally saturates. The saturation level of the peak increases with increasing voltage (V_p). This, together with the observation that the peak is solely the result of moving particles, raises the question why the peak is absent for *0→V(t)* (t = 0 to 0.05 s) and why it grows with the number of cycles. In order to find the answer to this question, it is essential to know the value of the mobility of the charged particles under homogeneous conditions. In the next section the size and the mobility of the charged particles are estimated.

7.4.3 Single Particle Tracking: Mobility and Size Measurements of Toner Particles

In this section a method is described to determine the mobility and radius of individual toner particles from observations of the particle motion under influence of an electric field.

The measured x position of a liquid toner particle as a function of time is shown in Fig. 7.9 (a). From t = 2 s to t = 7 s a sinusoidal voltage of V_p = 50 V and frequency 10 Hz is applied. In the absence of an electric field, the change in the position of the particle is due to Brownian motion while in the presence of an electric field, the particle oscillates in the direction of the electric field, i.e. the x direction. From the position data of the particle in the absence of an electric field, the diffusion constant and the hydrodynamic radius of the particle is estimated using Eq.7.7. In Fig.7.9 (b), a histogram for the size of 100 particles is shown; the mean size of the particles is 0.9 μm. The mobility distribution of 90 particles, calculated from their motion in a sinusoidal electric field, is shown in Fig. 7.9 (c). In the mobility histogram Fig. 7.9 (c), the particles with zero mobility (< 1 %) are not included. In Fig. 7.9 (c), it can be observed that most of the particles have a positive mobility which means that they are positively charged. The mean value of the mobility is around 30 $\mu m^2/Vs$. Using Eq.7.10, the estimated average charge on a particle is 18 e. Here, it is important to note that the mobility of the particle is measured by diluting the original liquid toner 100 times, so the charge of a particle in the undiluted liquid toner could be different from the value obtained here.

A toner particle with mobility 30 $\mu m^2/Vs$ needs $t > 0.10$ s (V_p = 400 V and f = 5 Hz) to reach the opposite electrode. The particles which contribute to the growing peak in Fig. 7.7 (f) take only 0.01 s, corresponding to a mobility of 4000 $\mu m^2/Vs$. For smaller voltages V_p < 200 V, there is no emerging peak just after 0.05 s (the time at which the voltage changes sign). In Fig. 7.7 (f), it is important to note that for the first few cycles of the voltage, there is only a peak in the current between t = 0.06 to 0.075 s, which matches well with the peak due to CIMs in Fig. 7.7 (b). The growing peak between t = 0.05 and 0.06 s in Fig. 7.7 (d, e & f) appears after a few oscillations of the voltage (for large V_p > ~200 V) and eventually saturates.

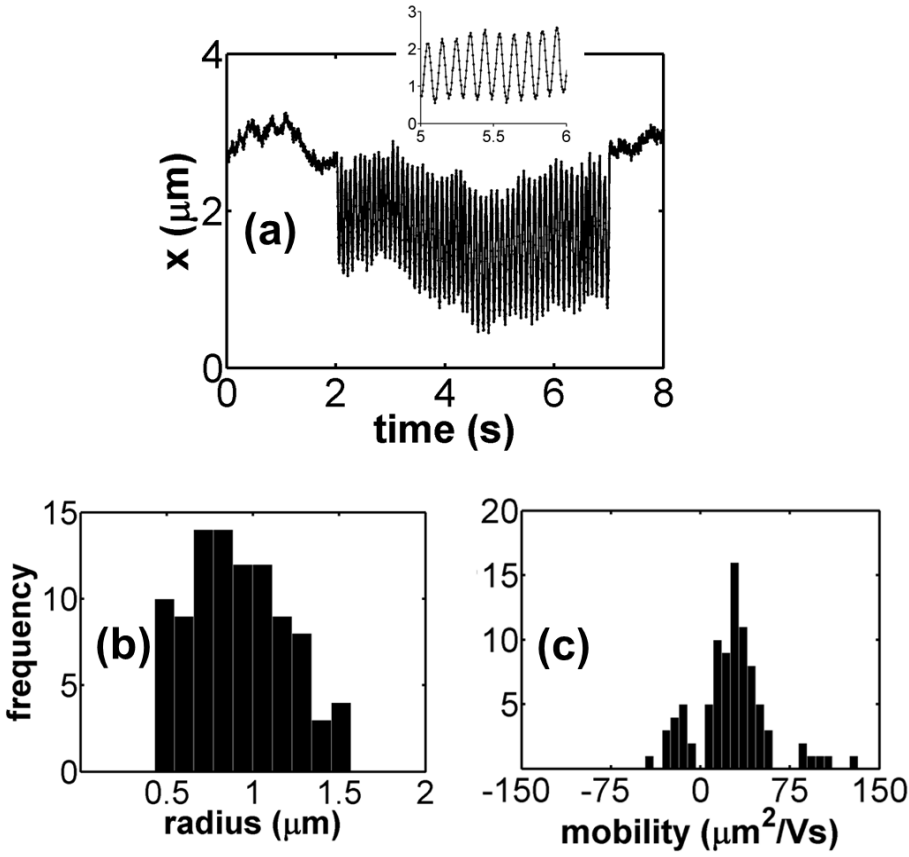

Figure 7.9: Results of experiment type E (a) the trajectory of a single liquid toner particle in the '*x*' direction without and with a sinusoidal voltage of V_p = 50 V with a frequency of 10Hz. (b) Histogram of the hydrodynamic radius of 100 liquid toner particles estimated from the Brownian motion of particles for a duration of 2 s. (c) The mobility histogram of 90 liquid toner particles. The particles with zero mobility are not included in the mobility histogram.

From the average value of the mobility of the particles (~30 μm^2/Vs), the average distance travel by particles in a linearly increasing field can be estimated using Eq. 7.6 as 7.5 μm (for V_p = 200 V, 5 Hz), 11.3μm (for V_p = 300 V, 5 Hz) or 15μm (for V_p = 400 V, 5 Hz). In Fig. 7.7, the peak between *t* = [0.05 to 0.06 s] is only observed for voltages (V_p > ~200 V) during which a large fraction of about ≈ 0.10 to 0.50 of the particle can reach the electrode before the voltage changes sign. While for the voltage with a value of V_p < 200 V, the fraction of particle reaching at the electrode will be very low about ≈ 0.01 to 0.05 This indicates that the occurrence of the peak and the increase in the mobility of toner particles is related to an effect occurring

near the electrodes. In order to further verify this, experiment type C is performed.

7.4.4 Current Measurements for Diluted Liquid Toner

For the experiment type C, the original liquid toner is diluted to 50% in lytol and no additional dispersing agent is added in the dispersion. The liquid toner is diluted in order to study the effect of the interfaces on the particles when the concentration of CIMs is very low in the dispersion. The result of experiment type C is shown in Fig. 7.10. In Fig. 7.10 (a), the absolute values of the measured currents in response to the triangular voltage with V_p = 400 V and f = 5 Hz of a duration of 2.3 s are placed one over another. From Fig. 7.10 (a), it can be seen that for the first quarter cycle of the voltage ($0 \rightarrow V(t)$), the measured current is very low (shown by red dots, $0 < t < 0.05$ s) and during the consecutive half cycles, the current increases substantially. In Fig. 7.10 (a), two peaks are observed in the current with increasing number of voltage cycles. The first peak between t = [0.05 to 0.062 s] is observed just after the change in the sign of the voltage. After a few cycles, the current in this peak increases to a very large value. The onset of this peak is the same as that of the peak observed in Fig. 7.7 (d, e, f) between t = [0.05 to 0.067 s], which indicates that both are related to the same phenomenon.

The onset time of the second peak 0.065 s < t < 0.075 s in Fig. 7.10 (a) and that due to Solsperse (Shown by black dotted line in Fig. 7.10 (a)) CIMs in Fig. 7.7 (b) matches quite well. This indicates that the second peak could be related to CIMs and possibly may have the mobility 210 $\mu m^2/Vs$. From the duration of the first peak in Fig. 7.10 (a), the mobility of the charges that contribute to the first peak is estimated by using Eq. 7.11 and is 2700 $\mu m^2/Vs$, which is very close to the value of the mobility of charges which contribute to the first peak in Fig. 7.7 (d, e, f).

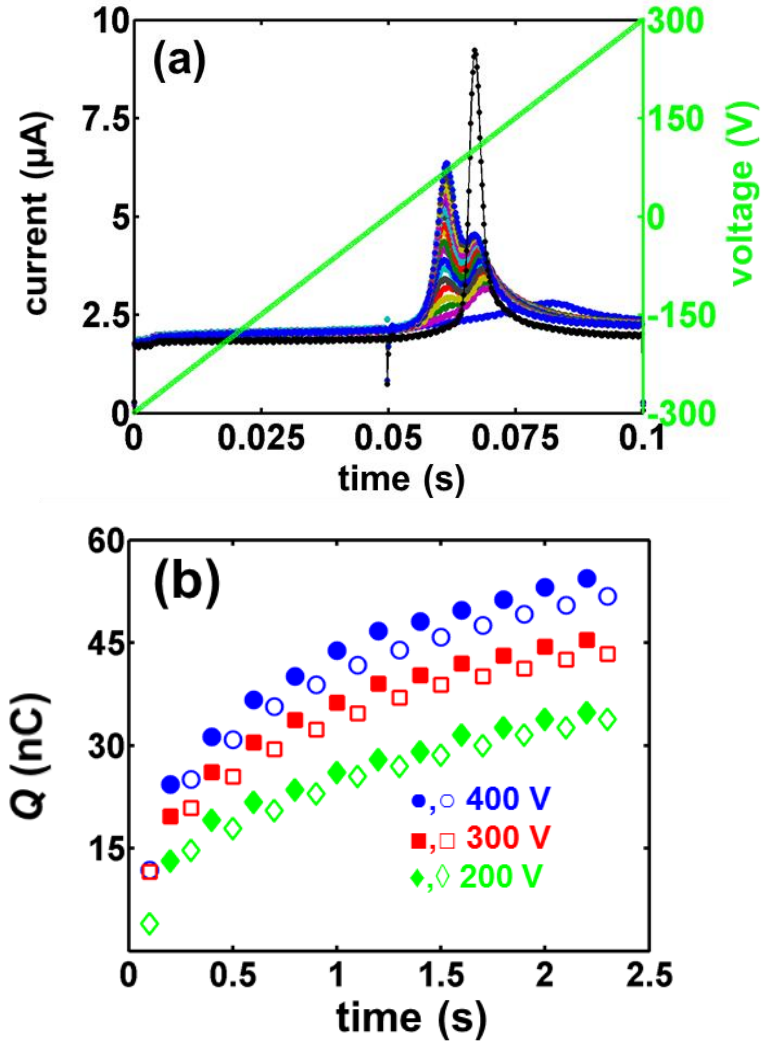

Figure 7.10: The result of the experiment type C for which the original liquid toner is diluted to 50% in lytol. In (a) all cycles of the current measured with the HFTC setup (S = 4.63 cm^2 and d = 40 μm) in response to a triangular voltage with V_p = 400 V (0→*V(t)*, *V(t)*→ -*V(t)* and -*V(t)*→*V(t)*) of 5 Hz with a total duration of 2.3 s are placed one over another. The measured current for the first quarter cycle of the voltage (0→*V(t)*), during which the charges move from a uniform distribution, is shown by red dots (0.05 to 0. 1 s). Also, the current measured using the same device for a solution of Solsperse $\phi_m = 0.0005$ in lytol during the 23 voltage cycle is shown by a black color line with black dots In (b), the corresponding integral of the current by subtracting the capacitive jump are plotted as a function of peak voltage. The filled data points show the integral of the current for -*V(t)*→*V(t)* while the empty data points show the same for *V(t)*→ -*V(t)*. Clearly, with increasing number of the voltage cycles, the integral of the current increases for a few cycles and then saturates.

The integrals of the currents from Fig. 7.10 (a) (with the capacitive part subtracted) are plotted as a function of the applied voltage duration in Fig.10 (b). It can be seen that the integral of the current increases for a few voltage cycles and then saturates. The saturation level of the integral is much larger than the initial level. It has already been verified that the voltage (V_p > 200 V) is large enough to transport a large fraction of the particles to the opposite electrodes. For the first few cycles the integral of the current is low which indicates that the charge on the particle is low. With increasing number of cycles the integral of the current increases. The same trend for the current peak between t = [0.05 to 0.0.067 s] in Fig. 7.7 (d, e, f) is observed. This indicates that both peaks are due to the same effect.

One explanation for the origin of the two peaks and of the increasing integral in Figs. 7.7 (d, e, f) & 7.10 is the following: During the equilibrium situation the particles have adsorbed positive and negative CIMs on their surface. The resulting charge is the sum of the (high) intrinsic charge and a number of adsorbed counter CIMs, yielding a small total value of the charge. When a particle with low mobility reaches the electrode with the opposite polarity, most of the counter CIMs may desorb from the surface. As the desorbed CIMs have the same polarity of the electrode where the particle has arrived, they may be repelled from that interface (because of the electrostatic repulsion) and travel to the opposite electrode. This results in two populations: particles without adsorbed counter CIMs (with a much larger charge than initially) and free counter CIMs. In Fig. 7.10 (a), the match in onset timing of the second peak with that of the peak due to Solsperse CIMs indicates that the second peak is indeed due to the CIMs. In Fig. 7.10 the various steps of charge transport, desorption at the interface and transport of charge inverse micelles are explained for the voltage of amplitude V_p = 300 V and frequency f =5 Hz.

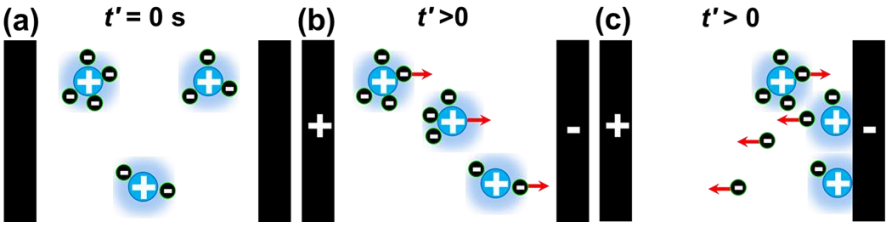

Figure 7.11: Schematic depiction of the various steps of the proposed desorption mechanism at an interface for a triangular voltage of V_p = 400 V with f = 5 Hz. In (a), at t = 0 s, the charged particles are uniformly distributed in the device t < 0 s). In (b) in response to the voltage the charged particles start to move to the opposite polarity electrodes. In (c), when the charged particle contacts the opposite polarity electrode, then the counter CIMs are desorbed (shown by black circles) form the particles leading to an increase of the particles charge.

The increasing and saturating integral of the current can be explained as follows: each time when particles contact the opposite polarity electrodes a fraction of counter CIMs may desorb from the particles leading to an increase of the effective charge of particles. This process may go on for a few cycles until no counter CIMs are left on the particle surface. Then the particle achieves the maximum charge and the integral of the peak saturates.

7.4.4.1 Simulation: A Peak Due to Highly Charged Particles

Let us now verify that the peak between t = 0.05 to 0.06 s in Fig. 7.7 (f) for the large voltages e.g., V_p = 400 V can be due to particles, which have a large value of the mobility, for example 4000 $\mu m^2/Vs$. This is done by a simulation for the situation of a mixture with CIMs and particles (Type B). Two simulations are performed. For the first simulation, it is considered that there are CIMs with $n_+ = n_- = \bar{n} = 10\ \mu m^{-3}, \mu_+ = -\mu_- = \mu = 210\ \mu m^2/Vs$ and charged particles with $\bar{n}_p = 0.1\ \mu m^{-3}$, $\mu_{p+} = -\mu_{p-} = \mu = 200\ \mu m^2/Vs$ and r = 0.9 µm. This situation is close to the initial homogeneous situation for which no peak is observed between t = 0.05-0.06 s in Fig. 7.7 (f). For the second simulation, the same dispersion is used, but additional particles are added with $n_{fp+} = \bar{n}_{fp} = 6 \times 10^{-4}\ \mu m^{-3}, n_{fp-} = 0, \mu = 4000\ \mu m^2/Vs$ and r = 0.9 µm. This situation corresponds to the case for which the growing peak with increasing voltage cycles is observed between t = 0.05-0.06 s in Fig. 7.7 (f). At equilibrium situation 70 % of the charged particle are positively charged while 30% are negatively charged will be verified in section 7.4.7, so we use the same assumption in the

simulation. Since the system is not electroneutral, there is an initial electric field between the electrodes. Each simulation starts from a homogeneous situation at t = 0 s and each has a duration of 0.2 s. A comparison of both simulations with the measurements is shown in Fig. 7.12.The measurement shown in Fig. 7.12 (taken from Fig. 7.7(f)), is a combination of the measurements for t = 0 - 0.1 s (red dots in Fig. 7.7 (f)) and that for 2.2 to 2.3 s (the last voltage cycle $-V(t) \rightarrow 0$)).

The sole purpose of this simulation is to verify the fact that the observed peak just after the change of the sign of the voltage ($0.1 < t < 0.16$ s) in Fig. 7.12(b) or in Fig. 7.7 (d, e & f) ($0.05 < t < 0.06$ s) is due to a fraction of particles that have a large mobility in contrast to the expected low mobility of most other particles. As a result of the large mobility these particles switch quickly to the opposite electrodes resulting in the peak. In the previous section the possible mechanism has already been discussed.

The match between the measurement and simulation up to 0.1 s indicates that the measured current is due to the drift, diffusion of the initially present CIMs and charged particles see Fig. 7.12. The match between the measurement and the second type of simulation for peak t = [0.1, 0.16 s] indicates that the peak is a result of the particles which have a large value of the charge compared to the other particles, see Fig. 7.12 (b). To match the simulated current peak with the measured peak (t = [0.1, 0.16 s]) the same value of the mobility is used that has been deduced from the transit time of the particles, i.e.,$4000\ \mu m^2/Vs$, section 7.4.2. Indeed, this confirms that the peak is a result of the fast particle which has a large value of the mobility and the charge. From the simulation parameters, the fraction of the particles which is charged up to the large value of 2331 e (μ = $4000\ \mu m^2/Vs$), with r = 0.9 μm, instead of the rest with 116 e (μ = $200\ \mu m^2/Vs$) is estimated as ~ 0.003. The reason for the mismatch between the measurements and simulation after 0.16 s has been already explained in the previous section and is attributed to EHD flow.

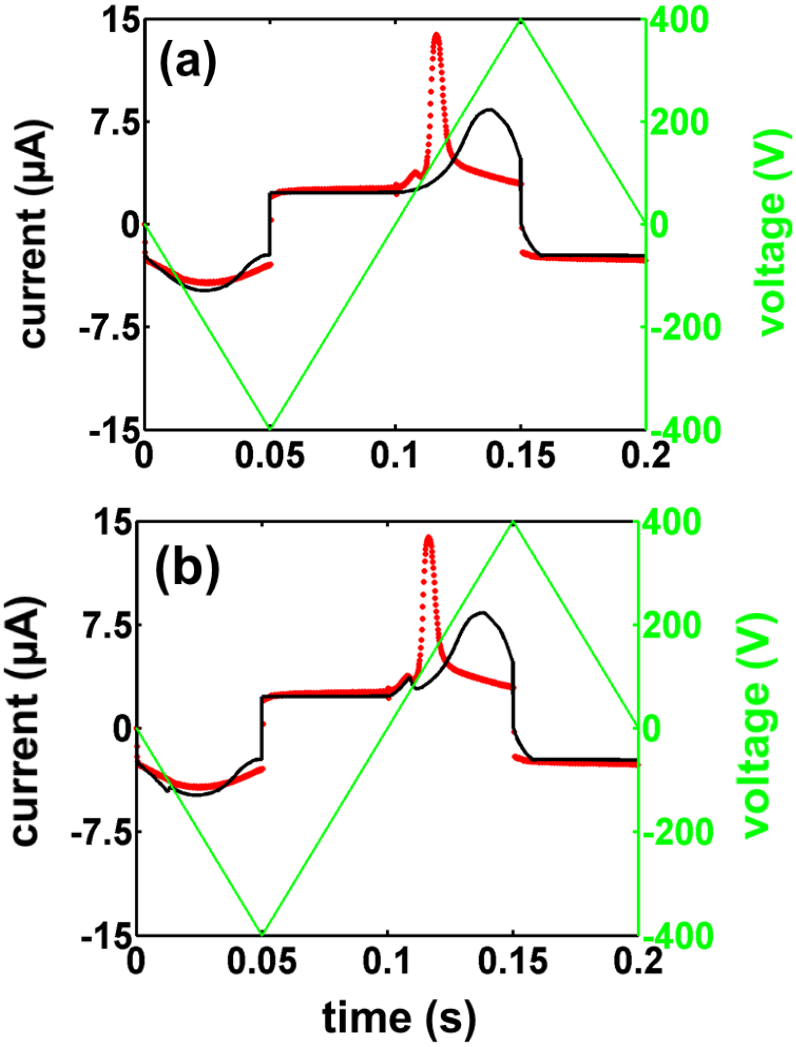

Figure 7.12: A comparison between the measurement (red dots) and simulations (black line) for the dispersion with CIMs and particles (Type B). The measured currents are from Fig. 7.7 (f) for t = [0, 0.1 s] and t = [2.2, 2.3s] (the duration for which the small peak between t = 2.25 to 2.26 s is saturated) are combined and plotted in the same figure for a complete period of the voltage (V_p = 400 V and f = 5 Hz). In (a), the measured currents are compared with the first type of simulation. In (b), the same measured currents are compared with the second type simulation. The simulation in (b) matches quite well with the measurement from t = 0 to 0.16 s. The match between the measurement and the simulation for the peak observed between t = 0.1 to 0.16 s, indicates that the peak is due to fast particles which have mobility 4000 $\mu m^2/Vs$.

In this simulation, the mobility of the initially present charged particle $\mu = 200\ \mu m^2/Vs$ is about seven times larger than the average value that is obtained from the measurements i.e., $\mu = 30\ \mu m^2/Vs$ in section 7.4.3. This can be explained as follows: for the experiment type E, the original liquid toner is diluted 100 times while for the experiment type B, the original liquid tones is diluted only 5 times and charging agent is added in the diluted dispersion ($\phi_m = 0.001$). Due to presence of the excess charging agent in the less diluted dispersion (compared to the type E), it is possible that the particles have a large value of the charge. Also, the first part of the simulations (t < 0. 1 s) shown in Fig. 7.12 looks similar in both the figures. The reason is that the concentration of the fast particle is very low in the bulk to affect the current substantially.

The transport of non-spherical or irregularly shaped particles can be modeled by the drift and diffusion and taking into account tensor nature of the mobility and diffusion constant. But an important consequence of the shape of particles can be in the interfacial charging of the particles that may depend on the surface-electrode contact area.

7.4.5 Current Measurements for Non-Polar Dispersions With High Concentrations of Particles

The results of experiment type D with undiluted liquid toner are shown in Fig. 7.13. The experiment is performed with V_p = 400 V and a frequency of 5Hz. In Fig. 7.13 (a), the absolute value of the measured currents during each half cycle are placed one over other. For an increasing number of cycles the peak in the current becomes higher and broader. The corresponding integrals of the current (after subtracting the capacitive part) are plotted as a function of time in Fig. 7.13 (b). The integral of the peak increases with increasing number of cycles and finally attains a saturation level. This trend matches with the result of experiment type B, shown in Fig. 7.8 (c). It can be concluded that the same phenomena as discussed in the previous sections occur in undiluted liquid toner. A broader peak could be the result of a wider range of mobilities of particles. However, due to the very high concentration of particles, the situation is much more complex and screening of the electric field or other effects should also be considered to interpret these currents. The reason for the increase and saturation of the peak has been already discussed in the previous section and could be related

to the presence of CIMs with opposite polarity on the surface of the particles.

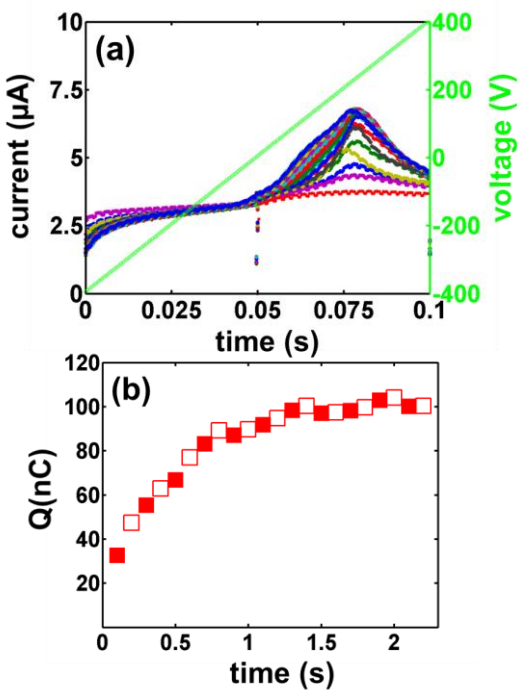

Figure 7.13: Result of experiment type D on undiluted liquid toner for a triangular wave voltage of -400 V to 400 V with frequency 5 Hz. In (a) the absolute value of the current measured for $0 \rightarrow V(t), -V(t) \rightarrow V(t)$ and $V(t) \rightarrow -V(t)$ are placed one over another. With increasing number of cycles an increasing peak is observed in the current. In (b) the integral of each peak is plotted as a function of time. The filled color symbols show the calculated integral of the current for $-V(t) \rightarrow V(t)$ while the unfilled symbols show the same for $V(t) \rightarrow -V(t)$.

7.4.6 Charging of Toner Particles at the Electrode Surfaces in a DC Field

In this section, the interfacial behavior of charged particles in response to a dc voltage is studied. For this study a roughly uniform layer of liquid toner is deposited on a substrate with interdigitated electrodes, a dc voltage is applied across the electrodes during 19 s and images are acquired simultaneously. The results of the experiment are shown in Fig. 7.14.

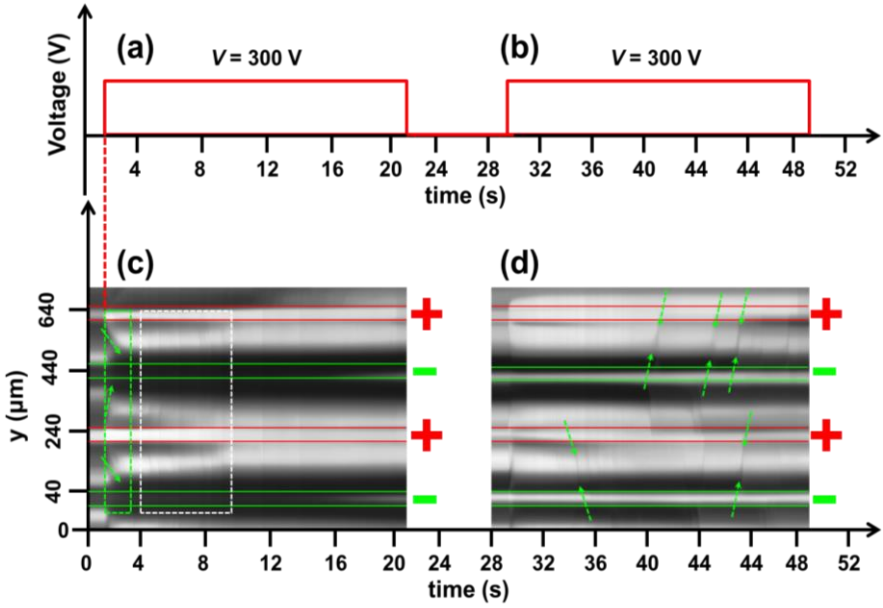

Figure 7.14: Results of experiment type F showing the effect of a DC voltage of 300 V on a layer of liquid toner on ITO interdigitated electrodes with spacing d = 200 µm. The electrodes are indicated by the space between red or green lines and the polarity of the applied voltage on the corresponding electrode is indicated by a plus or minus sign next to them. In (a, c) the time and voltage sequence is shown while in (b, d) the microscope transmission images which are acquired during 0 to 21 s (c) and 28 to 49 s (d) are combined by integrating the intensity of each image along the x direction. The dark areas in the image indicate the presence of particles. In (c) from t = 0 to 2 s, when no voltage is applied across the electrodes, the particles are relatively uniformly distributed between the electrodes and at t = 2 s the voltage is applied and the particles move to the electrodes with opposite sign (dashed green box). The region in the white dashed box shows that there is a change in the concentration of particles near the electrodes. This change corresponds to particle charging due to charge injection from the electrodes. After a duration of 21 s, the electrodes are short circuited for a few seconds, then in (d) again the same voltage is applied at t = 30 s. The gray areas next to the negative electrodes indicate that most of the particles are near the negative electrodes at this time. With increasing duration of the voltage, a few lines can be seen between the electrodes, these lines correspond to particles of which the charge is inverted due to charge injection from the electrodes.

In Fig. 7.14 (a, b), the applied voltage sequence is shown while the results of the experiments are shown in Fig. 7.14 (c, d). Fig. 7.14 (c, d) shows the average intensity of each acquired image along the x axis during 23 s with a frame rate of 15 Hz. In Fig. 7.14 (c), the dc voltage is applied at t = 2 s, as a result of which the particles move to the electrodes with opposite polarity

(green box). From the gray areas next to electrodes up to 10 s, it can be seen that most of the particles (~70 %) are next to the negative electrodes, indicating that most of them are positively charged. In Fig. 7.14 (a) for $t > 18$ s, it can be seen that the gray areas over the negative electrodes are getting brighter with increasing duration of the voltage .This means that the particles which are covering the electrode are moving away (during $t < 18$ s). In addition to this, it can also be observed that the gray areas near the positive electrodes are disappearing and the gray areas near the negative electrodes are becoming larger with increasing duration (around $t = 18$ s) of the voltage. This can be explained by the sign of the particle charge changing at the electrodes. The decreasing gray areas next to the electrodes in Fig. 7.14 (c) for $t > 10$ s demonstrate that the particles get charged when they touch the electrodes.

In Fig. 7.14 (d), after the previous sequence of 21 s and a few seconds of short circuiting the electrodes, the same voltage sequence is applied, as shown in Fig. 7.14 (b). In Fig. 7.14 (d), initially the gray areas near the negative electrodes are much wider than that of the gray areas near the positive electrodes, which indicates that most of the particles are positively charged. The voltage is applied at $t = 30$ s and from time to time some gray lines can be seen between the electrodes (as indicated by green dotted arrows between the electrodes in Fig. 7.14 (d)). These gray lines correspond to the particles which are switching between electrodes in the dc field. This is related to charge injection/inversion of the particles. From these lines, the average mobility of a particle is estimated and is found to vary from 400 to 1000 $\mu m^2/Vs$. The reason for this variation is that the gray lines in the figure are not due to individual particles but due to a chunk (containing 10 to 20 particles (estimated from the size of the chunk)) of particles. In addition to this, it can be also seen in Fig. 7.14 (d) for $t > 40$ s, that the gray areas near the positive electrodes are increasing (in contrast to $t < 40$ s) with increasing duration of the voltage. This means some of the particles that were initially concentrated next to the negative electrodes have switched to the positive electrodes as a result of charge inversion of the particles. From this, it can be concluded that when a particle touches the electrode in a dc field, there is a chance of charge injection onto the particle surface, resulting in an inversion of the particle charge.

7.4.7 Conclusions

The combination of electrical current measurements and optical measurements has revealed that the charge of pigment particles is not fixed. At large voltages particles can take up charge or give off charge at the electrodes depending on the situation. In a DC situation the charge of a particle at an electrode is reduced or even reversed in sign by taking up opposite charges. This is verified by observing particles switch between electrodes in a DC situation. In an AC situation particles can charge up as has been verified by current measurements and simulations. Such behavior can be explained if charge of the opposite sign is gradually desorbed from the surface.

Chapter 8

Conclusions and Future Scope

8.1 Summary of the Main Findings

In this dissertation the electrodynamics and interfacial properties such as adsorption/desorption of charge carriers in non-polar liquids with an added surfactant are explored, and a better and deeper understanding of the electrokinetic phenomena in non-polar liquids is provided. In general, two types of studies were performed. In one study, the interfacial behavior and the electrodynamics of charged inverse micelles (CIMs) are studied in systems without particles. In the other study the same was studied in nonpolar dispersions with particles.

The electrodynamics and the interfacial properties of CIMs in systems without particles are studied by reversing the voltage just after a long polarizing voltage step with magnitude larger than 1 V. The release and the interfacial behavior of CIMs present in equilibrium can be understood well on the basis of the Poisson-Nernst-Planck (PNP) equations in association with electrohydrodynamic (EHD) flow in the system. The experimentally found threshold voltage for EHD flow matches with the theoretical prediction of 11 V.

In an electric field, three types of new CIMs are generated in different proportions due to a bulk disproportionation mechanism. The generated

CIMs do not end up in the diffuse double layers like the initially present CIMs, but instead form interface layers. When the voltage is reversed or switched off, only a small fraction of these generated CIMs is released from the interfacial layers. These special CIMs (SCIMs) are found to be negatively charged. The release of the SCIMs from the interface layer is found to be space charge limited.

Although these SCIMs have the same size and mobility as the initially present CIMs, they behave differently at the interface. This difference can be explained by the position of the charge within the generated CIMs. The CIMs present in equilibrium form a diffuse double layer at the electrodes because their charge is in the core of the micelle. The resulting separation between the charge and its image charge on the electrode reduces the force between the CIM and the electrode. For most of the generated CIMs, the charge is located at the outside of the IM. These CIMs are therefore attracted more strongly by their image charge on the electrodes, and most of them end up in interface layers. Only 5 % of the generated CIMs is released when the field at the electrode becomes zero or changes sign.

The electrodynamics and the interfacial behavior of surfactant systems with a low concentration of particles for low voltages can be understood on the basis of the PNP equations in association with EHD flow. However, in the case of larger voltages, the particles can exchange charge when they come in contact with the electrodes, resulting in an increase in their mobility. This finding is important for applications in which charged colloidal particles switch between electrodes.

8.2 Applicability

The findings of this dissertation are relevant for applications such as electrophoretic displays and liquid toner printing which are based on the movement of charged pigment particles between interfaces in response to an applied voltage. In these applications, a surfactant is added to charge and stabilize pigment particles but the excess surfactant remains free in the bulk liquid in the form of neutral and charged inverse micelles (CIMs). Thus, the overall electrical behaviour of these systems is governed by the charged pigment particles and the free CIMs. Therefore, a better insight about the electrodynamical properties of CIMs and charged pigment particles are essential.

In this work two types of investigations have been carried out to understand the electrical behaviour of non-polar surfactant systems. In the first type of investigations, the electrokinetic features of a surfactant added non-polar liquid without the presence of colloidal particles are studied. In the second type of investigations the combined electrodynamics of the colloidal particles in the presence of CIMs are studied. In the following, how the findings of these investigations would help to evolve a new generation of EPDs with full color video rate capabilities and liquid toner printing with high speed, high contrast and environmental friendly printing are discussed.

In EPDs and liquid toner printing, the charged pigment particles move between two electrodes that are separated at a distance of 5-100 μm and the applied voltage is in the order of 15-400 V. It has been shown that when there are excess free CIMs and a voltage of such a high amplitude is applied, electrohdrodyanamic (EHD) flows occur in the system. It is a well-known fact that the EHD flows affect the stability of the dispersions [14,93,96]. Therefore, EHD flows are not desired in these systems. A way to avoid EHD flows is to use a surfactant with strong anchoring properties so that the concentration of free CIMs could be low in the dispersions [68].

Next the electrical and interfacial behaviour of the newly generated CIMs in the presence of an electric field is investigated and it is found that three different types of new CIMs are generated which behave differently at the interfaces. Furthermore, it is found that a small fraction of the generated CIMs (SCIMs) is released from the interfaces when the voltage changes sign at the interface and their release is space charge limited. The relevance of these findings for EPDs and liquid toner printing can be explained in two ways. Firstly, when the particles concentrate next to an interface and if there are CIMs with different physical properties, their interaction may affect the charge of particles, and this in turn may affect their transport properties. Secondly, space charge limited release of the SCIMs creates an asymmetric electric field in between the electrodes. An asymmetry of the field affects the switching characteristics of the particles and this may affect the performance of the display.

Finally, the interfacial behaviour of charged pigment particles is investigated. It is found that at a large voltage of a few hundred volts when the particles concentrate next to the opposite polarity electrodes, because of

the surface-electrode interactions the charge of the particles may increase or decrease. In the applications, an increase or decrease of the particle charge due to surface-electrode interactions can affect the switching characteristics of the particles that may reduce the quality of the displays and printing. A way to solve this issue would be to use a dielectric layer over the electrode so that electrode surface interactions can be avoided.

For a better and conclusive understanding of these technological model systems, a broad range of material systems need to be investigated and various experimental techniques must be integrated so that the physical, chemical and structural details of the charge carriers can be acquired simultaneously. By combining experimental techniques, for example transient electrical current and small angle neutron/X-ray scattering techniques, information about the core of the CIMs, the location of charge and the electrokinetics properties of the CIMs can be obtained simultaneously.

8.3 Future Scope

In addition to improving our understanding about non-polar surfactant systems, this dissertation also raises some important questions and suggests further investigations. During the quasi steady state part of the current new charge is generated, but only a small fraction of that charge is released when the voltage is reversed. Both from a fundamental and an application point of view, it would be interesting to find out what is happening to the rest of the charge.

Furthermore, this dissertation clearly demonstrates that three types of CIMs are generated due to bulk disproportionation in the presence of an electric field. Each of these types behaves differently at the interfaces. However, it is not clear how the same generation mechanism results in these three different types of CIMs. It is also found that the integral of the second peak saturates after a certain duration of the polarizing voltage, but the reason behind this is unknown. A further investigation of this could provide the reason for the generation of different types of CIMs.

Another question which needs further consideration is how the generated charge (SCIMs) decays with time and how the presence of neutral and

initially present CIMs accelerates this process. Understanding and modeling the decay of SCIMs could also provide hints about their generation.

In the case of a surfactant system with added particles, it has been shown that when particles touch the electrodes their charge can change. For applications such as EPDs, in which particles with CIMs are switching between the electrodes, it is important that the charge of the particle does not change. Therefore it is essential to understand how a particle exchanges charge at the vicinity of an electrode. In this dissertation, the particles that were used all had similar surface properties. It would be nice to study how the charging process varies with surface morphology, particle material and type of surfactant.

Bibliography

1. A. V. Delgado, F. González-Caballero, R. J. Hunter, L. K. Koopal, and J. Lyklema, "Measurement and Interpretation of Electrokinetic Phenomena (IUPAC Technical Report)," Pure Appl. Chem. **77**, 1753–1805 (2005).

2. J. Lyklema, "Principles of interactions in non-aqueous electrolyte solutions," Curr. Opin. Colloid Interface Sci. **18**, 116–128 (2013).

3. I. D. Morrison, "Electrical charges in nonaqueous media," Colloids Surfaces A Physicochem. Eng. Asp. **71**, 1–37 (1993).

4. S. Poovarodom and J. C. Berg, "Effect of particle and surfactant acid-base properties on charging of colloids in apolar media.," J. Colloid Interface Sci. **346**, 370–7 (2010).

5. F. Beunis, F. Strubbe, M. Marescaux, K. Neyts, and A. R. M. Verschueren, "Micellization and adsorption of surfactant in a nonpolar liquid in micrometer scale geometries," Appl. Phys. Lett. **97**, 181912 (2010).

6. F. Beunis, F. Strubbe, M. Karvar, O. Drobchak, T. Brans, and K. Neyts, "Inverse micelles as charge carriers in nonpolar liquids: Characterization with current measurements," Curr. Opin. Colloid Interface Sci. **18**, 129–136 (2013).

7. W. H. Briscoe and R. G. Horn, "Direct measurement of surface forces due to charging of solids immersed in a nonpolar liquid," Langmuir **18**, 3945–3956 (2002).

8. H. F. Eicke, M. Borkovec, and B. Das-Gupta, "Conductivity of water-in-oil microemulsions: a quantitative charge fluctuation model," J. Phys. Chem. **93**, 314–317 (1989).

9. C. E. Espinosa, Q. Guo, V. Singh, and S. H. Behrens, "Particle charging and charge screening in nonpolar dispersions with nonionic surfactants.," Langmuir **26**, 16941–16948 (2010).

10. P. Griffin Smith, M. N. Patel, J. Kim, T. E. Milner, and K. P. Johnston, "Effect of surface hydrophilicity on charging mechanism of colloids in low-permittivity solvents," J. Phys. Chem. C **111**, 840–848 (2007).

11. Q. Guo, V. Singh, and S. H. Behrens, "Electric charging in nonpolar liquids because of nonionizable surfactants," Langmuir **26**, 3203–3207 (2010).

12. M. F. Hsu, E. R. Dufresne, and D. A. Weitz, "Charge stabilization in nonpolar solvents," Langmuir **21**, 4881–4887 (2005).

13. M. Karvar, F. Strubbe, F. Beunis, R. Kemp, A. Smith, M. Goulding, and K. Neyts, "Transport of charged aerosol OT inverse micelles in nonpolar liquids," Langmuir **27**, 10386–10391 (2011).

14. P. Mürau and B. Singer, "The understanding and elimination of some suspension instabilities in an electrophoretic display," J. Appl. Phys. **49**, 4820–4829 (1978).

15. D. C. Prieve, J. D. Hoggard, R. Fu, P. J. Sides, and R. Bethea, "Two independent measurements of Debye lengths in doped nonpolar liquids.," Langmuir **24**, 1120–32 (2008).

16. R. J. Pugh and F. M. Fowkes, "The dispersibility and stability of coal particles in hydrocarbon media with a polyisobutene succinamide

dispersing agent," Colloids and Surfaces **11**, 423–427 (1984).

17. G. S. Roberts, R. Sanchez, R. Kemp, T. Wood, and P. Bartlett, "Electrostatic charging of nonpolar colloids by reverse micelles," Langmuir **24**, 6530–6541 (2008).

18. S. K. Sainis, V. Germain, and E. R. Dufresne, "Statistics of particle trajectories at short time intervals reveal fN-scale colloidal forces," Phys. Rev. Lett. **99**, 1–4 (2007).

19. S. K. Sainis, V. Germain, C. O. Mejean, and E. R. Dufresne, "Electrostatic interactions of colloidal particles in nonpolar solvents: role of surface chemistry and charge control agents.," Langmuir **24**, 1160–1164 (2008).

20. G. N. Smith and J. Eastoe, "Controlling colloid charge in nonpolar liquids with surfactants," Phys. Chem. Chem. Phys. **15**, 424–439 (2013).

21. G. N. Smith, J. E. Hallett, and J. Eastoe, "Celebrating Soft Matter's 10th Anniversary: Influencing the charge of poly(methyl methacrylate) latexes in nonpolar solvents," Soft Matter **11**, 8029–8041 (2015).

22. F. Strubbe, F. Beunis, T. Brans, M. Karvar, W. Woestenborghs, and K. Neyts, "Electrophoretic retardation of colloidal particles in nonpolar liquids," Phys. Rev. X **3**, (2013).

23. F. Strubbe, A. R. M. Verschueren, L. J. M. Schlangen, F. Beunis, and K. Neyts, "Generation current of charged micelles in nonaqueous liquids: Measurements and simulations," J. Colloid Interface Sci. **300**, 396–403 (2006).

24. A. S. Dukhin and P. J. Goetz, "How non-ionic "electrically neutral" surfactants enhance electrical conductivity and ion stability in non-polar liquids," J. Electroanal. Chem. **588**, 44–50 (2006).

25. A. Dukhin and S. Parlia, "Ions, ion pairs and inverse micelles in non-polar media," Curr. Opin. Colloid Interface Sci. **18**, 93–115 (2013).

26. M. M. Gacek and J. C. Berg, "The role of acid-base effects on particle charging in apolar media," Adv. Colloid Interface Sci. **220**, 108–123 (2015).

27. T. Hao, "Exploring the charging mechanisms in non-aqueous multiphase surfactant solutions, emulsions and colloidal systems via conductivity behaviors predicted with eyring's rate process theory," Phys. Chem. Chem. Phys. **18**, 476–491 (2016).

28. I. F. Blagovidov, V. P. Lapin, G. L. Trofimpva, and G. I. Shor, "Mechanism of the stabilizing effect of motor-oil additives," Chem. Technol. Fuels Oils **7**, 439–443 (1971).

29. S. A. Jones, G. P. Martin, and M. B. Brown, "Manipulation of beclomethasone-hydrofluoroalkane interactions using biocompatible macromolecules.," J. Pharm. Sci. **95**, 1060–74 (2006).

30. H. J. Spinelli, "Polymeric Dispersants in Ink Jet Technology," Adv. Mater. **10**, 1215–1218 (1998).

31. D. L. Klass, "Electroviscous Fluids. I. Rheological Properties," J. Appl. Phys. **38**, 67 (1967).

32. T. Hao, "Electrorheological fluids," Adv. Mater. **13**, 1847–1857 (2001).

33. P. Bartlett and A. I. Campbell, "Three-dimensional binary superlattices of oppositely charged colloids," Phys. Rev. Lett. **95**, 128302 (2005).

34. Q. Chen, S. C. Bae, and S. Granick, "Directed self-assembly of a colloidal kagome lattice," Nature **469**, 381–384 (2011).

35. K.-Q. Zhang and X. Y. Liu, "In situ observation of colloidal monolayer nucleation driven by an alternating electric field.," Nature

429, 739–743 (2004).

36. A. Yethiraj and A. Van Blaaderen, "A colloidal model system with an interaction tunable from hard sphere to soft and dipolar," Nature **421**, 513–517 (2003).

37. K. E. Tettey, M. Q. Yee, and D. Lee, "Layer-by-layer assembly of charged particles in nonpolar media," Langmuir **26**, 9974–9980 (2010).

38. Y. Chen, J. Au, P. Kazlas, A. Ritenour, H. Gates, and M. McCreary, "Electronic paper: Flexible active-matrix electronic ink display.," Nature **423**, 136 (2003).

39. B. Comiskey, J. D. Albert, H. Yoshizawa, and J. Jacobson, "An electrophoretic ink for all-printed reflective electronic displays," Nature **394**, 253–255 (1998).

40. M. Grätzel, "Ultrafast colour displays.," Nature **409**, 575–576 (2001).

41. A. R. M. Verschueren, L. W. G. Stofmeel, P. J. Baesjou, M. H. W. M. van Delden, K.-M. H. Lenssen, M. Mueller, G. Oversluizen, J. J. van Glabbeek, J. T. M. Osenga, and R. M. Schuurbiers, "Optical performance of in-plane electrophoretic color e-paper," J. Soc. Inf. Disp. **18**, 1 (2010).

42. E. Kishi, Y. Matsuda, Y. Uno, A. Ogawa, T. Goden, N. Ukigaya, M. Nakanishi, T. Ikeda, H. Matsuda, and K. Eguchi, "5.1: Development of In-Plane EPD," SID Dig. **0**, 24–27 (2000).

43. J. Heikenfeld, P. Drzaic, J.-S. Yeo, and T. Koch, "Review Paper: A critical review of the present and future prospects for electronic paper," J. Soc. Inf. Disp. **19**, 129 (2011).

44. G. H. Gelinck, H. E. A. Huitema, P. J. G. Van Lieshout, S. Sohn, T. Whitesides, and M. D. McCreary, "A rollable , organic electrophoretic QVGA display with field-shielded pixel," J. Soc. Inf. Disp. 113–118 (2006).

45. T. Bert, H. De Smet, F. Beunis, and K. Neyts, "Complete electrical and optical simulation of electronic paper," Displays **27**, 50–55 (2006).

46. J. Chen, W. Cranton, and M. Fihn, *Handbook of Visual Display Technology* (Springer-Verlag Berlin Heidelberg, 2012).

47. T. Whitesides, M. Walls, R. Paolini, S. Sohn, H. Gates, and J. Jacobson, "Towards Video-rate Microencapsulatred Dual-Particle Electrophoretic Displays," SID Dig. **4**, 133–135 (2005).

48. S. J. Telfer and M. D. McCreary, "42-4: *Invited Paper* : A Full-Color Electrophoretic Display," SID Symp. Dig. Tech. Pap. **47**, 574–577 (2016).

49. I. Chen, J. Mort, and M. A. Machonkin, "Particle Charge, Mobility, and ζ Potential in Nonpolar Colloids," Langmuir **13**, 5036–5040 (1997).

50. S. Matsusaka, H. Maruyama, T. Matsuyama, and M. Ghadiri, "Triboelectric charging of powders: A review," Chem. Eng. Sci. **65**, 5781–5807 (2010).

51. Http://www8.hp.com/us/en/commercial-printers/indigo-presses/10000.html, "HP Indigo 10000 Digital Press | HP® Official Site," .

52. A. Alj, A. Denat, J. P. Gosse, B. Gosse, and I. Nakamura, "Creation of Charge Carriers in Nonpolar Liquids," IEEE Trans. Electr. Insul. **EI-20**, 221–231 (1985).

53. F. M. Fowkes and R. J. Pugh, "Steric and Electrostatic Contributions to the Colloidal Properties of Nonaqueous Dispersions," in *ACS Symposium Series, Vol. 240* (1984), pp. 331–354.

54. *Micelles*, Topics in Current Chemistry (Springer-Verlag, 1980), Vol. 87.

55. P. C. Hiemenz and R. Rajagopalan, *Principles of Colloid and Surface Chemistry*. (Marcel Dekker, 1997).

56. R. Galneder, V. Kahl, A Arbuzova, M. Rebecchi, J. O. Rädler, and S. McLaughlin, "Microelectrophoresis of a bilayer-coated silica bead in an optical trap: application to enzymology.," Biophys. J. **80**, 2298–2309 (2001).

57. Q. Guo, J. Lee, V. Singh, and S. H. Behrens, "Surfactant mediated charging of polymer particles in a nonpolar liquid," J. Colloid Interface Sci. **392**, 83–89 (2013).

58. F. Strubbe, M. Prasad, and F. Beunis, "Characterizing generated charged inverse micelles with transient current measurements.," J. Phys. Chem. B **119**, 1957–65 (2015).

59. A. Parsegian, "Energy of an ion crossing a low dielectric membrane: solutions to four relevant electrostatic problems.," Nature **221**, 844–846 (1969).

60. E. L. Michor and J. C. Berg, "Extension to the charge fluctuation model for the prediction of the conductivity of apolar, reverse micellar systems," Langmuir **28**, 15751–15755 (2012).

61. S. Poovarodom, S. Poovarodom, and J. C. Berg, "Effect of alkyl functionalization on charging of colloidal silica in apolar media," J. Colloid Interface Sci. **351**, 415–420 (2010).

62. M. E. Parent, J. Yang, Y. Jeon, M. F. Toney, Z.-L. Zhou, and D. Henze, "Influence of surfactant structure on reverse micelle size and charge for nonpolar electrophoretic inks.," Langmuir **27**, 11845–51 (2011).

63. J. K. Lee, S. S. Kim, Y. I. Park, C. D. Kim, and Y. K. Hwang, "In-cell adaptive touch technology for a flexible e-paper display," Solid. State. Electron. **56**, 159–162 (2011).

64. J. Lee, Z.-L. Zhou, G. Alas, and S. H. Behrens, "Mechanisms of Particle Charging by Surfactants in Nonpolar Dispersions.," Langmuir **31**, 11989–99 (2015).

65. C. E. McNamee, Y. Tsujii, and M. Matsumoto, "Interaction forces between two silica surfaces in an apolar solvent containing an anionic surfactant," Langmuir **20**, 1791–1798 (2004).

66. F. Strubbe, F. Beunis, M. Marescaux, and K. Neyts, "Charging mechanism in colloidal particles leading to a linear relation between charge and size," Phys. Rev. E, **75**, (2007).

67. J. Lyklema, "Colloid stability as a dynamic phenomenon," Pure Appl. Chem. **52**, (1980).

68. I. D. Morrison and S. Ross, *Colloidal Dispersions : Suspensions, Emulsions, and Foams* (Wiley-Interscience, 2002).

69. J. H. Masliyah and S. Bhattacharjee, *Electrokinetic and Colloid Transport Phenomena* (Wiley-Interscience, 2006).

70. T. Tadros, "General Principles of Colloid Stability and the Role of Surface Forces," Colloid Stab. Role Surf. Forces - Part I **1**, 1–22 (2011).

71. R. J. Hunter, *Foundations of Colloid Science* (Oxford University Press, 2001).

72. F. Beunis, F. Strubbe, M. Marescaux, J. Beeckman, K. Neyts, and A. R. M. Verschueren, "Dynamics of charge transport in planar devices.," Phys. Rev. E **78**, 11502 (2008).

73. A. R. M. Verschueren, P. H. L. Notten, L. J. M. Schlangen, F. Strubbe, F. Beunis, and K. Neyts, "Screening and separation of charges in microscale devices: Complete planar solution of the Poisson - Boltzmann equation," J. Phys. Chem. B **112**, 13038–13050 (2008).

74. M. Karvar, F. Strubbe, F. Beunis, R. Kemp, N. Smith, M. Goulding, and K. Neyts, "Investigation of various types of inverse micelles in nonpolar liquids using transient current measurements.," Langmuir **30**, 12138–43 (2014).

75. M. Prasad, F. Strubbe, F. Beunis, and K. Neyts, "Different Types of Charged Inverse Micelles in Non-Polar Media," Langmuir **32**, 5769–5801 (2016).

76. M. Karvar, F. Strubbe, F. Beunis, R. Kemp, N. Smith, M. Goulding, and K. Neyts, "Charging Dynamics of Aerosol OT Inverse Micelles," Langmuir 10939–10945 (2015).

77. M. Prasad, F. Beunis, K. Neyts, and F. Strubbe, "Switching of charged inverse micelles in non-polar liquids," J. Colloid Interface Sci. **458**, 39–44 (2015).

78. J. Lee, Z.-L. Zhou, and S. H. Behrens, "Charging Mechanism for Polymer Particles in Nonpolar Surfactant Solutions: Influence of Polymer Type and Surface Functionality," Langmuir **32**, 4827–4836 (2016).

79. P. Kornilovitch and Y. Jeon, "Transient electrophoretic current in a nonpolar solvent," J. Appl. Phys. **109**, 64509 (2011).

80. B. A. Yezer, A. S. Khair, P. J. Sides, and D. C. Prieve, "Use of electrochemical impedance spectroscopy to determine double-layer capacitance in doped nonpolar liquids," J. Colloid Interface Sci. **449**, 2–12 (2015).

81. F. Beunis, F. Strubbe, K. Neyts, and D. Petrov, "Beyond Millikan: The dynamics of charging events on individual colloidal particles," Phys. Rev. Lett. **108**, 16101 (2012).

82. G. Seth Roberts, T. A. Wood, W. J. Frith, and P. Bartlett, "Direct measurement of the effective charge in nonpolar suspensions by

optical tracking of single particles.," J. Chem. Phys. **126**, 194503 (2007).

83. R. J. Pugh and F. M. Fowkes, "and Stability of Carbon Black in Media," Colloids and Surfaces **9**, 33–46 (1984).

84. D. P. J. Barz, M. J. Vogel, and P. H. Steen, "Determination of the zeta potential of porous substrates by droplet deflection: II. Generation of electrokinetic flow in a nonpolar liquid," Langmuir **26**, 3126–3133 (2010).

85. M. M. Gacek and J. C. Berg, "Effect of synergists on organic pigment particle charging in apolar media," Electrophoresis **35**, (2014).

86. S. Ramo, "Currents Induced by Electron Motion," Proc. IRE **27**, 584–585 (1939).

87. Z. He, "Review of the Shockley–Ramo theorem and its application in semiconductor gamma-ray detectors," Nucl. Instruments Methods Phys. Res. Sect. A Accel. Spectrometers, Detect. Assoc. Equip. **463**, 250–267 (2001).

88. F. Strubbe, F. Beunis, and K. Neyts, "Determination of the effective charge of individual colloidal particles," J. Colloid Interface Sci. **301**, 302–309 (2006).

89. F. Beunis, F. Strubbe, M. Karvar, O. Drobchak, T. Brans, K. Neyts, and A. R. M. Verschueren, "Electric charging of inverse micelles in a nonpolar liquid with surfactant," Colloids Surfaces A Physicochem. Eng. Asp. **440**, 10–19 (2014).

90. K. Neyts, M. Karvar, O. Drobchak, T. Brans, F. Strubbe, and F. Beunis, "Simulation of charge transport and steady state in non-polar media between planar electrodes with insulating layers," Colloids Surfaces A Physicochem. Eng. Asp. **440**, 101–109 (2014).

91. M. Z. Bazant, K. Thornton, and A. Ajdari, "Diffuse-charge dynamics in electrochemical systems," Phys. Rev. E **70**, 21506 (2004).

92. F. Strubbe, F. Beunis, M. Marescaux, B. Verboven, and K. Neyts, "Electrokinetics of colloidal particles in nonpolar media containing charged inverse micelles," Appl. Phys. Lett. **93**, 1–4 (2008).
93. M. Trau, S. Sankaran, D. A. Saville, and I. A. Aksay, "Pattern Formation in Nonaqueous Colloidal Dispersions via Electrohydrodynamic Flow," Langmuir **11**, 4665–4672 (1995).

94. I. Chen, J. Mort, M. A. Machonkin, J. R. Larson, and F. Bonsignore, "Space-charge-perturbed electrophoresis in nonpolar colloidal dispersions," J. Appl. Phys. **80**, 6796–6803 (1996).

95. M. Trau, D. A. Saville, and I. A. Aksay, "Field-Induced Layering of Colloidal Crystals," Science. **272**, 706–709 (1996).

96. T. Lin, S. M. Rubinstein, A. Korchev, and D. A. Weitz, "Pattern formation of charged particles in an electric field.," Langmuir **30**, 12119–23 (2014).

97. F. Beunis, F. Strubbe, K. Neyts, and A. R. M. Verschueren, "Power-law transient charge transport in a nonpolar liquid," Appl. Phys. Lett. **90**, 182103 (2007).

98. J. Crocker and D. Grier, "Methods of Digital Video Microscopy for Colloidal Studies," J. Colloid Interface Sci. **179**, 298–310 (1996).

99. M. Prasad, F. Strubbe, F. Beunis, and K. Neyts, "Space charge limited release of charged inverse micelles in non-polar liquids," Phys. Chem. Chem. Phys. **18**, 19289–19298 (2016).

100. F. Beunis, F. Strubbe, M. Marescaux, K. Neyts, and A. R. M. Verschueren, "Diffuse double layer charging in nonpolar liquids," Appl. Phys. Lett. **91**, 182911 (2007).

101. P. K. Watson, "Electrohydrodynamic Stability of Space-Charge-Limited Currents in Dielectric Liquids. II. Experimental Study," Phys. Fluids **13**, 1955 (1970).

102. J. M. Schneider and P. K. Watson, "Electrohydrodyamic stability of Space-Charge-Limited Currents in Dielectric Liquids I. Theoretical study," Phys. Fluids **13**, 1948–1954 (1970).

103. G. T. Wright, "Mechanisms of space-charge-limited current in solids," Solid. State. Electron. **2**, 165–189 (1961).

104. A. Rose, "Space-Charge-Limited Currents in Solids," Phys. Rev. **97**, 1538–1544 (1955).

105. A. A. Grinberg, S. Luryi, M. R. Pinto, and N. L. Schryer, "Space-charge-limited current in a film," IEEE Trans. Electron Devices **36**, 1162–1170 (1989).

106. P. N. Murgatroyd, "Theory of space-charge-limited current enhanced by Frenkel effect," J. Phys. D. Appl. Phys. **3**, 151 (1970).

107. D. Orden and F. Santos, "Geometry 2003," Most **528**, 509–528 (2003).

108. M. Trau, D. A. Saville, and I. A. Aksay, "Assembly of Colloidal Crystals at Electrode Interfaces," Langmuir **13**, 6375–6381 (1997).

109. P. Nakroshis, M. Amoroso, J. Legere, and C. Smith, "Measuring Boltzmann's constant using video microscopy of Brownian motion," Am. J. Phys. **71**, 568 (2003).